Temporal and Spatial Multi-omics Characterization of Smith-Lemli-Opitz Syndrome

Amy Li

A dissertation

submitted in partial fulfillment of the

requirements for the degree of

Doctor of Philosophy

University of Washington

2023

Reading Committee:

Libin Xu, Chair

Miklos Guttman

Rheem A. Totah

Program Authorized to Offer Degree:

Medicinal Chemistry

University of Washington

Abstract

Temporal and Spatial Multi-Omics Characterization of Smith-Lemli-Opitz Syndrome

Amy Li

Chair of the Supervisory Committee:

Libin Xu

Medicinal Chemistry

Smith-Lemli-Opitz syndrome (SLOS) is a metabolic disorder caused by genetic mutations in the *DHCR7* gene, leading to defective 3β-hydroxysterol-Δ^7-reductase (DHCR7), the enzyme that catalyzes the last step of cholesterol synthesis. The resulting deficiency in cholesterol and accumulation of its precursor, 7-dehydrocholesterol (7-DHC), have a profound impact on brain development, manifesting as developmental delay, cognitive impairment, moderate-to-severe intellectual disability, and behavioral deficits. Additionally, disorder severity and phenotype vary widely between individuals. Anomalies of the CNS are frequently observed in patients, with microcephaly, ventricular dilatation, and malformations of the corpus callosum and cerebellum being some of the most common. However, therapeutic interventions for the neurological aspects of SLOS are lacking. Further neurophysiological studies on SLOS mouse models are needed to understand how the loss of *Dhcr7* and disruption of cholesterol biosynthesis affect the course of neurodevelopment. The objective of this dissertation is to

establish the spatial and temporal lipidomic and transcriptomic changes that occur during development in a *Dhcr7*-KO mouse model of SLOS. **Chapter 1** provides background on the history, genetic cause, and clinical phenotype of the disorder. **Chapter 2** presents the results from an untargeted lipidomics analysis of developing mouse brains in wild-type (WT) and *Dhcr7*-KO mice. We compared relative lipid levels throughout development, from embryonic day 12.5 to postnatal day 0. The study identified differentially expressed brain lipids between WT and *Dhcr7*-KO mice at specific developmental time points, revealing lipid metabolic pathways that are affected in SLOS beyond the cholesterol biosynthesis pathway, such as glycerolipid, glycerophospholipid, and sphingolipid metabolism. In **Chapter 3**, we mapped the spatial distribution of sterols and lipids in neonatal *Dhcr7*-KO mouse brains using mass spectrometry imaging. We determined the sites of accumulation of sterols and major oxysterol metabolites of 7-DHC and identified differentially expressed lipids between WT and *Dhcr7*-KO brains. **Chapter 4** presents a complementary transcriptomics analysis to **Chapter 2**, where we carried out RNA sequencing analysis of whole brains from WT and *Dhcr7*-KO mice at the same four time points spanning development. We discuss the impact of these gene expression changes and affected signaling pathways as they relate to the neurological phenotype of SLOS. In **Chapter 5**, we summarize the overall project findings and directions for future research.

Acknowledgments

My journey through graduate school would not have been possible without the help and support of many people who came alongside me during the past seven and a half years. There are too many to list by name, but you know who you are. Thank you for being a part of this journey.

Firstly, I would like to thank my thesis advisor, Dr. Libin Xu, for his steadfast and unwavering mentorship over the years. I may have severely tested your patience at times, especially towards the end, but you have proven to be an extremely patient mentor, who cares deeply about your students, as much as you care about the science and research. Thank you for always responding quickly to emails and Slack messages (even ones after midnight), for your enthusiasm and passion towards scientific progress, and inspiring your students and leading by example with your incredible work ethic. But most of all, thank you for believing in me, even when I didn't believe in myself. It has been a privilege of a lifetime to learn from you.

The same gratitude extends to both past and present members of the Xu lab, who have made the journey that much more fun. You are some of the most hard-working, yet kind and compassionate people that I know, and it has been a privilege to work and learn alongside you. To my classmates and friends in the department of Medicinal Chemistry, you filled the hallways with lively conversation and laughter and made the basement not such a bad place to be. I would also like to express my sincere appreciation to the hard-working administrative staff who keep the department running smoothly so that students can focus on their work.

Thank you to my thesis committee members: Dr. Melissa Barker-Haliski, Dr. Miklos Guttman, Dr. Allan Rettie, and Dr. Rheem Totah, who have helped guide me through the different stages of graduate school, providing invaluable feedback at every step. I am also very thankful for the collaborative and supportive environment within the University of Washington

and the many invaluable resources available here, including the Mass Spectrometry Center, EDGE Center, and ARC Facility, that helped make my research possible. Thanks especially to Dale Whittington, for being a wizard of mass spectrometers and a trusted confidant for many students in the department, including myself.

Finally, to my mom, dad, and sister… thank you for your endless love and support throughout the years, and for providing meals, hugs, and encouragement whenever I came home for a break. It kept me going, especially through the hard times. To all my friends and family, including my church family at Faith Bible Church, you have filled the last few years with so much joy and life, outside of the lab. Thank you for making the worst parts of graduate school a little brighter, and the good parts even better, by sharing in every step along the way.

soli Deo gloria.

TABLE OF CONTENTS

LIST OF FIGURES

LIST OF TABLES

Chapter 1 Introduction

1.1 Smith-Lemli-Opitz Syndrome

1.1.1. Inherited disorders of cholesterol biosynthesis

Smith-Lemli-Opitz syndrome belongs to a larger family of seven inherited disorders of cholesterol synthesis. All seven disorders arise from genetic mutations at various points in cholesterol biosynthesis. **Tables**

Table 1.1 summarizes the genetic basis, associated enzymatic defect, and inheritance pattern of each of these disorders (Herman, 2003; Forbes D. Porter, 2002; F. D. Porter & Herman, 2011). The process of cholesterol biosynthesis occurs over a series of nearly 30 enzymatic reactions to produce cholesterol from the starting product, acetyl-CoA. The post-squalene portion of cholesterol biosynthesis is shown in **Figure 1.1**. Lanosterol is the first sterol intermediate after the cyclization of squalene epoxide and represents the first committed step toward the final cholesterol product. At this point, the cholesterol synthesis pathway branches into two parallel routes, known as the Kandutsch-Russell and Bloch pathways.

Defects at any one of these enzymatic steps in cholesterol biosynthesis results in a disorder and decreased production of cholesterol; however, the unique characteristics of each disorder are thought to result from the accumulation of a specific cholesterol precursor and/or its metabolites. Antley-Bixler and HEM dysplasia are caused by genetic mutations in two multifunctional enzymes, cytochrome P450 oxidoreductase (POR) and lamin B receptor (LBR), respectively, that function in more than just sterol synthesis. Congenital hemidysplasia with ichthyosiform erythroderma and limb defects (CHILD) syndrome and X-linked chondrodysplasia punctata 2 (CDPX2) are two of the X-linked dominant disorders. Smith-Lemli-Opitz syndrome (SLOS), lathosterolosis, and desmosterolosis are closely related due to their

enzymatic defects in the latter part of cholesterol synthesis. All three disorders are characterized by multiple malformations in the organ systems that depend on Hedgehog signaling for embryonic patterning (Cooper et al., 2003).

1.1.2. Genetic, biochemical, and phenotypical characterization of SLOS

The first cholesterol biosynthesis disorder discovered was Smith-Lemli-Opitz syndrome (SLOS/RSH, OMIM #270400). It is recognized as the prototypical cholesterol biosynthesis disorder and the third most frequent autosomal recessive disorder after cystic fibrosis and phenylketonuria (Yu & Patel, 2005). The clinical incidence of SLOS varies by geographical location and ethnicity. In the United States, it is estimated to be approximately 1/20,000 to 1/60,000 (Lazarin et al., 2017; Nowaczyk et al., 2001; Waterham et al., 1998). The carrier frequency is estimated to be 1/30, suggesting a higher clinical incidence (around 1/1,590 to 1/13,500) than what is observed (Battaile et al., 2001). However, this discrepancy could be due to prenatal lethality in the most severe cases and under-diagnosis of mild cases.

Three male patients with a similar set of shared characteristics and multiple anomalies were first described in 1964 by Smith, Lemli, and Opitz (Smith et al., 1964). It was not until 1993 that the disorder was biochemically characterized when Irons et al. first reported severely abnormal cholesterol synthesis in two female SLOS patients (Irons et al., 1993). Reduced plasma cholesterol levels and accumulation of 7-dehydrocholesterol (7-DHC), the precursor to cholesterol in the Kandutsch-Russell pathway, pointed to 7-DHC reductase (DHCR7) deficiency as the culprit (Irons et al., 1993; Tint et al., 1994). This biochemical defect was further confirmed in other cases (Tint et al., 1994). *DHCR7* as the underlying genetic cause was finally established in 1998 by several independent groups through molecular genetic analyses (Fitzky et al., 1998; Moebius et al., 1998; Wassif et al., 1998). The *DHCR7* gene (chromosome 11q12-13) encodes

3β-hydroxysterol-Δ^7-reductase (DHCR7), a 54 kDa microsomal protein that catalyzes the reduction of the C7-8 bond in 7-DHC to produce cholesterol. Thus, the primary biochemical hallmark of SLOS is decreased levels of cholesterol and accumulation of 7-DHC, in the brain and liver amongst other tissues (Fitzky et al., 2001).

Since its discovery, over 200 genetic variants of *DHCR7* have been identified, ranging from splice site to missense and nonsense mutations that result in either reduced or completely absent DHCR7 activity (Lazarin et al., 2017; Schoner et al., 2020; Waterham & Hennekam, 2012; Witsch-Baumgartner et al., 2000; Yu et al., 2000). The most common mutant allele is a splice site mutation, IVS8-1G>C (c.964-G>C) in intron VIII, which leads to a frameshift and truncated gene product. This functional *null* allele results in the most severe phenotypes. The next most common allele is the missense mutation, T93M. The wide range of genetic variability also coincides with the wide variability of phenotype and severity among SLOS patients. The most common clinical features of SLOS include craniofacial dysmorphologies, developmental delay, behavioral deficits, heart defects, and, in the most severe cases, intrauterine lethality. To evaluate the clinical severity of SLOS, the modified Bialer scoring system for phenotypic severity was developed by Kelley and Hennekam (Kelley & Hennekam, 2000) and combines the scores for congenital malformations found in each of the affected organ systems: brain, oral, acral (limbs), eye, heart, kidney, liver, lung, bowel, and genitalia.

1.1.3. Neurological phenotype of SLOS

From the earliest reports of SLOS, developmental abnormalities of the CNS have been observed, noting “hypoplasia of frontal lobes, cerebellum, and brain stem” and “serious defects in the brain, including demyelination of the cerebral hemispheres, cranial nerves, and peripheral nerves, and neuronal loss” (Irons et al., 1993). Additional anomalies of the CNS include

microcephaly, enlargement of ventricles, and malformations of the corpus callosum and cerebellum. MRI studies of patients with SLOS show anomalies involving the midline and para-midline structures of the brain (Lee, Yoshida, et al., 2013). In the most severe cases (around 5% of SLOS patients), holoprosencephaly occurs from failed cleavage of the prosencephalon, and the left and right hemispheres of the brain are not separated properly (Edison & Muenke, 2003).

Clinically, these developmental anomalies manifest as neurologic problems such as hypotonia, failure to feed, delayed motor development, cognitive impairment, and behavioral problems (Tierney et al., 2001). Behavioral manifestations of SLOS include self-injurious behavior, repetitive and ritualistic/autistic behavior, irritability, and sleep cycle disturbance (Tierney et al., 2001). SLOS also has the highest correlation with autism of any single gene disorder, with approximately 75% of children with SLOS being diagnosed with some form of autism spectrum disorder (ASD) (Bukelis et al., 2007; Sikora et al., 2006).

1.1.4. Therapeutic intervention and clinical studies

Presently, there is no cure for the disorder, and while dietary cholesterol supplementation is the current standard-of-care, the long-term effects are marginal, especially for rescuing brain function or improving developmental progress. Cholesterol treatment increases cholesterol concentrations in the periphery but does not correct biochemical deficiencies in the brain or rescue developmental processes (Elias et al., 1997; Irons et al., 1997; Sikora et al., 2004). There are, however, some anecdotal evidence and results from observational studies that indicate that cholesterol supplementation improves behavioral outcomes, such as irritability, aggression, and hyperactivity (Tierney et al., 2010; Tierney et al., 2001). Some experimental treatments have been investigated through clinical trials, including statins (Chan et al., 2009; Haas et al., 2008; Petr E. Jira et al., 2000; Wassif et al., 2017), bile acids (Nwokoro & Mulvihill, 1997), and

antioxidants (Fliesler, 2013; Fliesler et al., 2018) in combination therapy with cholesterol supplementation. Simvastatin, a blood-brain barrier permeable inhibitor of HMG-CoA reductase, the rate-limiting enzyme of cholesterol biosynthesis, was found to normalize plasma 7-DHC/total sterol levels and improve irritability symptoms in SLOS patients in a randomized, placebo-controlled trial by Wassif et al. (Wassif et al., 2017). However, these results conflict with other studies that showed limited evidence of clinical improvement in behavioral problems and increased risk of adverse reactions to statin therapy (Haas et al., 2008).

1.1.5. Modeling SLOS for *in vitro* and *in vivo* study

Several models of SLOS have been developed to aid in studying the molecular mechanisms underlying the pathophysiology of SLOS. The first transgenic *Dhcr7*-KO mouse models were generated by deletion of *Dhcr7* exons III-V or exon VIII (Fitzky et al., 2001; Wassif et al., 2001) and are analogous to the most severe IVS8-1G>C mutation in humans. However, these *Dhcr7*-KO pups do not survive past the first day of birth due to failure to feed. Another mouse model was generated via site-directed mutagenesis to reproduce one of the most common missense mutations in humans, T93M. This hypomorphic mouse model has a milder phenotype, exhibits some similar phenotypes to the human disorder, and survives into adulthood. However, the biochemical defect corrects itself over time (Correa-Cerro et al., 2006). More recently, a viable conditional KO model has been developed with LoxP-Cre technology that allows for inducible deletion of *Dhcr7* in specific cell types and tissues (Kanuri et al., 2021) and resolves the issue of perinatal lethality in other KO models.

Cellular models, including SLOS patient-derived induced pluripotent stem cells (iPSCs) and neural progenitor cells (NPCs), are also available for studying SLOS in disease-relevant human cell types (Wen et al., 2016). In a study by Francis et al., researchers at the NICHD used

SLOS patient-derived iPSCs that were further differentiated into NPCs (Francis et al., 2016). When comparing SLOS NPCs to healthy control NPCs, they showed signs of premature differentiation into neurons and loss of pluripotency. Whole genome analysis of SLOS iPSCs compared to control revealed differential expression of over 44 genes, many of which were associated with Wnt/β-catenin signaling, a critical signaling process that regulates neuronal development. Additionally, this defect in Wnt signaling was dependent on the accumulation of 7-DHC and not the lack of cholesterol. Our lab has also shown that NPCs isolated from *Dhcr7*-KO mouse cortices display reduced proliferation and increased differentiation during neurogenesis relative to WT NPCs (Tomita et al., 2022). It was further demonstrated that treatment with 7-DHC-derived oxysterols, such as DHCEO, led to similar perturbations in neurogenesis in NPCs isolated from WT mouse cortices.

Finally, an alternative to genetic models is the use of known pharmacological and selective inhibitors of DHCR7, including AY9944 (Fliesler et al., 2018) and BM 15.766 (Roux et al., 2000). Other xenobiotics inhibit DHCR7 (off-target) to various extents, such as antipsychotic and antidepressant drugs, benzalkonium chlorides, and chemotherapeutics (Boland & Tatonetti, 2016).

1.2 The Role of Cholesterol in Neurodevelopment

In general, cholesterol is an essential molecule for normal cellular function in humans. From the earlier discussion on the various disorders that arise from defects in cholesterol synthesis, we can grasp the importance of this lipid for a multitude of biological roles and functions: 1. Cholesterol is a major structural component of cellular membranes, lipid rafts, and microdomains that are important for signaling transduction and membrane trafficking (Ikonen, 2008). 2. Cholesterol is a precursor for bile acids, bioactive oxysterols, and steroid hormones (T.

Li & Chiang, 2009). 3. Cholesterol is an important covalent modulator of hedgehog proteins in Sonic Hedgehog signaling, an important pathway for embryonic patterning and development (J. A. Porter et al., 1996).

Cholesterol plays a unique role in the CNS. While the CNS only accounts for roughly 2% of total body weight, it accounts for 23% of total cholesterol in the body (Dietschy & Turley, 2004). Most of the cholesterol is found in myelin sheaths, a special type of plasma membrane synthesized by oligodendrocytes that insulate axons to potentiate electrical signals across long distances. Cholesterol is also important for neurite outgrowth and synapse formation and function (Funfschilling et al., 2012). Glial cells provide the necessary cholesterol needed by neuronal cells for synapse formation (Mauch et al., 2001). Lipid rafts and microdomains, which are highly enriched in cholesterol, act as primary sites of transmembrane signaling processes that occur during neurodevelopment.

The cholesterol pool in the CNS is distinct due to the formation of the blood-brain barrier early in development, making the CNS an isolated entity that must synthesize all its own cholesterol *de novo*. Some maternal-fetal transfer of cholesterol is known to occur, but after development of the blood-brain barrier, cholesterol cannot be taken up from peripheral circulation into the brain. In humans, the blood-brain barrier is formed between 12-18 weeks of gestation, while in mice, this occurs between E10 and E11 (Tint et al., 2006). Thus, for the first 10-11 days of development, the dam supplies all necessary cholesterol to the fetus.

The accumulation of 7-DHC, one of the most reactive lipid molecules to free radical oxidation with a peroxidation rate constant of 2260 M^{-1} s^{-1} (Xu et al., 2009), is specific to *DHCR7* inhibition in SLOS and leads to the formation of various oxysterol metabolites (Xu, Korade, et al., 2011). Oxysterols are known to exert a variety of biological functions as

important signaling molecules, both in normal physiological conditions and aberrant pathological processes in disease states (Griffiths & Wang, 2018). Oxysterol metabolites produced either from free radical oxidation or enzymatic reaction have been found to accumulate in the tissues and fluids of SLOS patients (Korade et al., 2010; Xu et al., 2010).

Figure 1.2 summarizes the role of cholesterol metabolism in the brain.

1.3 Leveraging Multi-omics Techniques to Understand the Biological Consequences of *Dhcr7*-KO

1.3.1. Comprehensive multi-dimensional lipidomics

Lipidomics is a rapidly growing field that enables the characterization of the entire lipidome in cells, tissues, or an organism (Han & Gross, 2022; Wenk, 2010). Changes in lipid metabolism and homeostasis caused by different disease states or drug treatments can be probed by lipidomics experiments, which can aid our understanding of normal physiology and disease pathology at the molecular level. While current technologies using liquid chromatography coupled with high-resolution mass spectrometry have greatly increased coverage of the lipidome, there are still limitations in resolving the large number of lipid species with similar masses in a narrow mass window. Our lipidomics method combines two orthogonal separation techniques, hydrophilic interaction liquid chromatography (HILIC) and ion mobility (IM), to enhance the resolution of lipid species based on headgroup polarity and gas phase size and shape, respectively, across the various classes of glycerolipids, glycolipids, phospholipids, and sphingolipids (K. Hines et al., 2017; A. Li et al., 2020). We refer the readers to **Appendix A** for an in-depth discussion on this method.

1.3.2. Spatial lipidomics by mass spectrometry imaging (MSI)

Another significant advancement in lipidomics research is the emergence of mass spectrometry-based imaging as a powerful, label-free technique to visualize the distribution and co-localization of molecular compounds in biological systems with minimal sample preparation (Walch et al., 2008). With the known developmental CNS abnormalities commonly present in SLOS individuals (Lee, Conley, et al., 2013), MSI is useful for correlating metabolic deficiency with morphological features present in disorder progression and anatomical CNS landmarks.

1.3.3. Transcriptomic profiling by RNA-sequencing

Through technological advancements in high-throughput DNA sequencing methods, such as in RNA-sequencing, the study of transcriptomics is becoming hugely popular and more accessible in biological research (Wang et al., 2009). The transcriptome constitutes the complete set of gene transcripts in a cell, tissue, or organism. While different types of cells may have the same genome, the transcription of a subset of those genes into RNA is what gives each cell type its specific identity and function. Transcriptomics is thus a powerful tool for characterizing the changes in gene expression profiles that occur in response to a disease state or treatment (Kukurba & Montgomery, 2015).

1.4 Dissertation Overview

In this thesis, I have leveraged two ‘omics techniques, lipidomics and transcriptomics, to study how defective *Dhcr7* affects the course of cholesterol-dependent processes during neurodevelopment using a *Dhcr7*-KO mouse model. This project emphasizes the importance of understanding the global changes that occur in SLOS beyond the initial defect of cholesterol synthesis and their downstream effects on various signaling pathways that can be targeted for the development of novel therapies. Current treatments for SLOS fail to bring about significant

improvement across the vast array of neurological phenotypes present in the disorder. Thus, further neurophysiological studies of *in vivo* SLOS models are needed to understand how the disruption of cholesterol synthesis affects neurodevelopment.

In the remaining chapters of this dissertation, we will focus on the determination of the lipidomic and transcriptomic changes that occur in a *Dhcr7*-KO mouse model of SLOS. In **Chapters 2** and **3**, I have characterized the temporal and spatial distributions of brain lipids in *Dhcr7*-KO mice, using two mass spectrometry (MS)-based techniques, hydrophilic interaction liquid chromatography-ion mobility-MS (HILIC-IM-MS) and MALDI-MS imaging. **Chapter 2** focuses on the temporal aspect of lipidomics changes through three embryonic (E12.5, E14.5, and E16.5) and one postnatal time point (PND0). **Chapter 3** focuses on the spatial component of the sterolomic and lipidomic changes in PND0 *Dhcr7*-KO mice compared to WT. **Chapter 4** describes a complementary transcriptomics analysis of WT and *Dhcr7*-KO mouse brains through the same time points studied in **Chapter 2**, to identify differentially expressed genes and enriched signaling pathways. Finally, **Chapter 5** summarizes the overall project findings and future directions for related research.

Figures

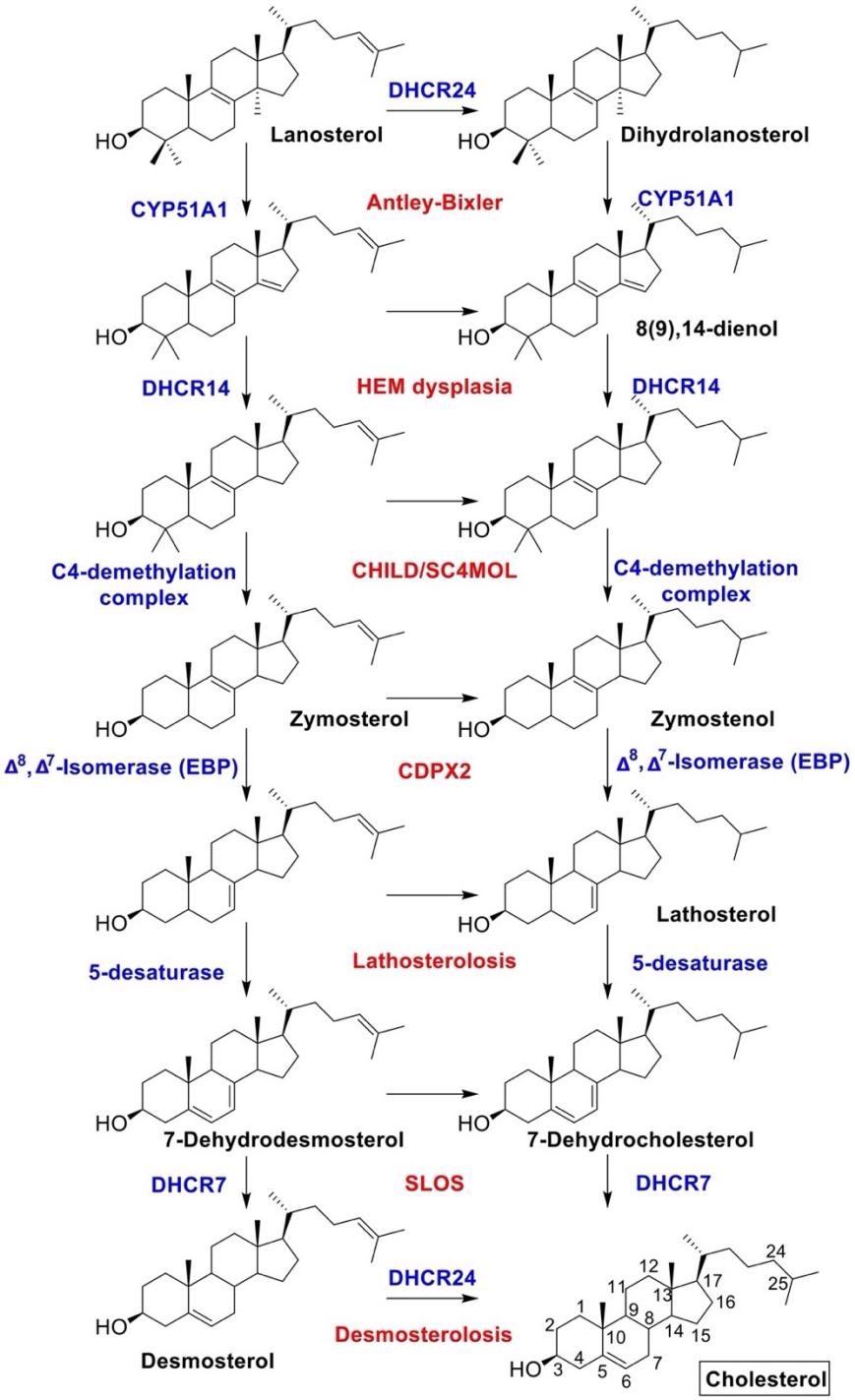

Figure 1.1 Schematic of post-squalene cholesterol biosynthesis, converting lanosterol into cholesterol, also displaying the enzymatic defects (shown in blue) that result in cholesterol biosynthesis disorders (shown in red).

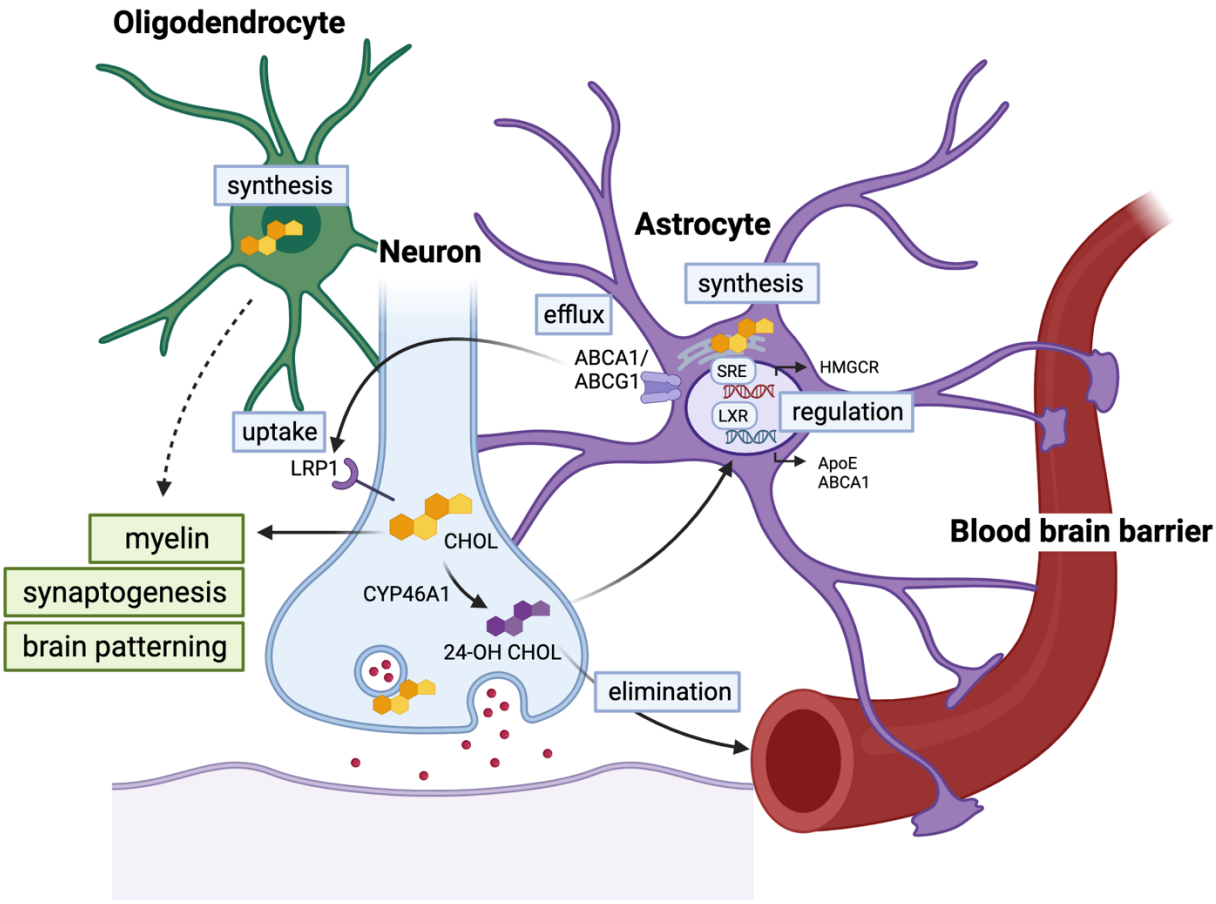

Figure 1.2 Cholesterol metabolism in the brain, including cholesterol synthesis, regulation, efflux, uptake, and elimination. Astrocytes are the main source of cholesterol for neurons, whereas oligodendrocytes synthesize cholesterol to form myelin. Created with BioRender.com.

Tables

Table 1.1 Table summarizing the family of cholesterol biosynthesis disorders.

Disorder	Gene	Protein	Inheritance
Antley-Bixler	*POR*	Cytochrome P450 oxidoreductase	Autosomal recessive
HEM Dysplasia	*LBR/ DHCR14*	Lamin B receptor/Sterol **Δ**14-reductase	Autosomal recessive
CHILD Syndrome	*NSDHL*	C4-demethylation complex	X-linked dominant
CDPX2	*EBP*	Sterol **Δ**8,**Δ**7-isomerase	X-linked dominant
SLOS	*DHCR7*	7-dehydrocholesterol reductase	Autosomal recessive
Lathosterolosis	*SC5D*	Lathosterol 5-desaturase	Autosomal recessive
Desmosterolosis	*DHCR24*	Sterol **Δ**24-reductase	Autosomal recessive

Chapter 2 Temporal Changes in the Brain Lipidome during Neurodevelopment of SLOS Mice

Portions of this chapter have been adapted and reproduced with permission from:

> Amy Li, Kelly M. Hines, Dylan H. Ross, James W. MacDonald, and Libin Xu, Temporal changes in the brain lipidome during neurodevelopment of Smith-Lemli-Opitz syndrome mice, *Analyst*, 147:1611–1621, (**2022**).

2.1 Introduction

Smith-Lemli-Opitz syndrome (SLOS, OMIM #270400) is a congenital multiple malformation disorder that has a wide range of incidence rates from 1 in 20,000 to 1 in 60,000 people in various geographic populations (Battaile et al., 2001; Ciara et al., 2006; Nowaczyk et al., 2001; F. D. Porter et al., 2011). SLOS is caused by mutations in the *DHCR7* gene (Fitzky et al., 1998; Tint et al., 1994; Wassif et al., 1998), which encodes 3β-hydroxysterol-Δ^7-reductase (DHCR7), an enzyme that catalyzes the last step of cholesterol biosynthesis in the Kandutsch-Russell pathway, *i.e.*, the reduction of 7-dehydrocholesterol (7-DHC) to cholesterol. This defect leads to decreased levels of cholesterol and accumulation of 7-DHC in individuals with SLOS (Tint et al., 1994; Tint et al., 1995). 7-DHC is highly reactive toward free radical oxidation and has been identified as a substrate for enzyme-mediated oxidation (Xu et al., 2009), leading to the formation of a large number of oxidation products, termed oxysterols, also found to accumulate in the tissues and fluids of SLOS patients (Xu et al., 2010; Xu et al., 2013). It is now widely recognized in the field that both cholesterol deficiency and elevated 7-DHC levels contribute to SLOS pathophysiology.

Brain development is a highly regulated process, including tight control over the metabolism of lipids. There is a high metabolic demand for cholesterol in both neuronal and glial cells, with the highest rate of *de novo* synthesis occurring during early brain development, as the

blood-brain barrier prevents uptake of cholesterol from systemic circulation, as well as possible but limited maternal-fetal transfer (Dietschy et al., 2004). Brain lipid content can reach over 60% of white matter, 40% of grey matter, and 81% of myelin by dry weight (O'Brien & Sampson, 1965). Cholesterol is an especially important lipid in the brain. In addition to being a major component of cellular membranes, it is essential for embryonic development *via* the Hedgehog signaling pathway (J. A. Porter et al., 1996), myelination (Saher et al., 2005), and synapse formation and function (Koudinov & Koudinova, 2001; Mauch et al., 2001). Gene regulation of cholesterol and lipid homeostasis are closely interconnected through the SREBP pathways and liver X receptors (Horton et al., 2002; Repa et al., 2000). Brain abnormalities affecting cognition and behavior are among the major clinical phenotypes of SLOS patients. Microarray analysis of gene expression in wild-type (WT) and Dhcr7-KO embryonic mouse brains found that *Dhcr7*-KO led to a large downregulation of *Srebf1*, the major regulator of fatty acid synthesis (Waage-Baudet et al., 2005). Furthermore, exposure of Neuro2a neuroblastoma cells to 7-DHC-derived oxysterols led to not only changes in the expression of genes involved in cholesterol homeostasis (*Hmgcr, Dhcr7, SREBP2, S1P, SQS*) but also downregulation of the fatty acid synthesis gene (*FASN*) (Korade et al., 2010). Thus, an imbalance in metabolism or homeostasis in lipid levels could be an important factor in the neurological defects present in the SLOS pathophysiology. Recently, a detailed lipidomics analysis of aging mouse brains was reported by Tu et al. (Tu et al., 2017). However, despite the known critical and diverse roles of lipids during neurodevelopment, the temporal changes in the brain lipidome during normal brain development have not been investigated, and related lipidomic changes beyond sterol homeostasis have not been elucidated in SLOS animal models. The goal of this study was to fill these specific knowledge gaps.

Shotgun and liquid chromatography (LC)-mass spectrometry (MS)-based methods have paved the way for the broad application of lipidomics in various biological systems (Burla et al., 2018; Han & Gross, 2005; O. Quehenberger & Dennis, 2011; Ryan & Reid, 2016). In recent years, LC coupled with ion mobility (IM)-MS has shown advantages in enhancing the confidence of lipid identification using collision cross section (CCS) values obtained from an orthogonal IM separation, in addition to retention times and *m/z* (K. Hines et al., 2017; K. M. Hines et al., 2017; Kyle et al., 2016; Tu et al., 2017). Different classes of lipids tend to occupy characteristic spaces in the CCS-*m/z* conformational plot, enabling the differentiation of isobaric or similar-mass lipids from different classes (K. Hines et al., 2017; Kyle et al., 2016). We developed a hydrophilic interaction liquid chromatography (HILIC)-IM-MS based lipidomics method, which enables resolution of individual lipid species based on their headgroup polarity (lipid class) *via* the HILIC dimension and further resolution of co-eluting lipids *via* the IM dimension (K. Hines et al., 2017; K. M. Hines et al., 2017; Hines & Xu, 2019). More recently, open-source software containing predicted retention times and CCS databases have been developed to facilitate the identification of lipids using the multi-dimensional data generated from LC-IM-MS analyses, such as LipidIMMS (Zhou et al., 2018) and MS-DIAL 4 (Tsugawa et al., 2020). We recently developed *LiPydomics*, an all-in-one Python package that contains several functional modules, including data processing and normalization, lipid identification using a comprehensive collection of HILIC retention times and lipid CCS values, statistical analysis, graphical plotting, and an intuitive, interactive user interface (Ross, Cho, Zhang, et al., 2020). With the *LiPydomics* package, lipid identification at Level 3 (lipid species level: lipid class/subclass and fatty acid sum composition) can be achieved according to the Lipidomics Standards Initiative (Liebisch et al., 2013; Ryan et al., 2016).

In this work, we comprehensively characterized the brain lipidome of developing WT and *Dhcr7*-KO (equivalent to the most common and severe SLOS mutation, IVS8-1G>C, in humans) (Fitzky et al., 2001) mice utilizing HILIC-IM-MS and *LiPydomics*. Our study spanned several developmental time points to extensively describe the temporal lipidomic landscapes of WT and *Dhcr7*-KO mouse brains and how lipid levels change throughout development and due to genetic disorder by comparing time points and genotypes, respectively. Furthermore, we identified differentially expressed lipids between WT and *Dhcr7*-KO mice at the different developmental stages, which indicated altered glycerolipid, glycerophospholipid, and sphingolipid metabolism.

2.2 Results and Discussion

2.2.1. Untargeted lipidomics analysis of brain tissue extracts

Brains were harvested from WT and *Dhcr7*-KO mice at E12.5, E14.5, E16.5, and PND0, as depicted in **Figure 2.1A**. *Dhcr7*-KO brain tissues are generally smaller than matching WT brain tissues, although such differences did not reach statistical significance (**Figure 2.2**). Untargeted lipidomics analysis was then carried out for these brain tissue extracts using our HILIC-IM-MS method in positive and negative ionization modes, resulting in 2,521 and 4,867 detected features, respectively. After initial peak picking and alignment using Progenesis (**Figure 2.1B**), the compound measurements for detected features were exported and analyzed using the *LiPydomics* package, which automatically performs identification at the level of lipid subclass and sum composition of fatty acyl chains based on different combinations and tolerances of measured or predicted *m/z*, RT, and CCS (**Figure 2.1C**) (Ross, Cho, & Xu, 2020; Ross, Cho, Zhang, et al., 2020). We narrowed down the list of IDs, only using IDs that were identified with predicted *m/z* + RT + CCS matching (*pred_mz_rt_ccs* with tolerances of 50 ppm,

0.2 min, and 3.0%, respectively), leading to 419 and 572 putatively identified compounds for positive and negative modes. The output from *LiPydomics* identifications includes all potential matches; thus, multiple putative IDs are included for some compounds and are not listed in any meaningful order. We then narrowed down the list further by employing an intensity cutoff of 500 (using "Maximum Abundance," which is calculated as the highest average of all sample groups' averaged abundances), consistent with background noise levels in the mass spectra, to exclude low-intensity features.

The list was manually inspected for overlapping and unlikely IDs. We first removed putative bacterial lipid identifications in this analysis, including acyl-PE, acyl-PG, lysyl-PG, DGDG, and MGDG (K. M. Hines et al., 2017; Hines et al., 2019) (identified features removed: 46 and 123 bacterial lipids in positive and negative modes). Subsequently, unfavorable and minor adducts, including chloride and formate adducts, were removed in the negative mode since the solvent contains ammonium acetate, and odd-chain lipids were removed for simplicity since even-chain fatty acids are predominant in mammalian systems, though we acknowledge that odd-chain lipids are possible. We then chose to carry out lower-level identification with *m/z* + RT (*pred_mz_rt*) or *m/z* + CCS (*pred_mz_ccs*) for lipid species that are missing CCS or RT values in our predicted database due to an insufficient number of entries for that specific class and adduct in the training dataset. These additional identifications were manually confirmed by searching against METLIN and LIPID MAPS databases and using Lipid Pioneer (Ulmer et al., 2017). For example, triacylglycerides (TG) and free fatty acids (FFA) were not identified in *LiPydomics* because the predicted RTs were not included in the current database version. However, their early retention times were consistent with experimental RT values; thus, TGs and FFAs were still identified by all three parameters and included in the final list. Other classes not

currently covered in *LiPydomics* include monoacylglycerides (MG) and saturated ceramides (Cer), which were manually identified after searching the other databases listed above. After manual inspection, 272 and 280 lipid adducts (401 unique lipids in total) were identified for positive and negative modes, respectively (**Figure 2.1C**). As a result of this identification process, a total of 538 CCS values (272 and 266 values in positive and negative modes, respectively) were measured in this study, including CCS values of 21 hexosylceramides (HexCer), 13 MGs, four saturated Cers, and 11 FFAs that are reported for the first time (**Figure 2.3**). Cardiolipins (CL), which were manually identified by RT and *m/z*, were excluded from these plots. Due to their doubly charged state, proper CCS calibration should be carried out using a doubly charged calibrant species to achieve accurate TWIM CCS values (Bush et al., 2012; Hines et al., 2019), which was not acquired in this experiment.

Lipid identifications are annotated with lipid class and fatty acyl sum composition nomenclature, corresponding to Level 3 identification, according to the Lipidomics Standards Initiative (Liebisch et al., 2013). We recognize the limitations of the implemented analytical workflow in its inability to distinguish isobaric or isomeric lipid species with the same sum fatty acyl composition without additional MS/MS experiments. Although HILIC separation increases the confidence of lipid class identification, post-IM fragmentation (MS^E) does not allow clear differentiation of MS/MS spectra of lipids from the same class due to their close retention times. Furthermore, we note that using a single internal standard, sphingosyl-PE (d17:1/12:0), allows only for relative comparisons and normalization to reduce variation across samples and not absolute quantitation, which requires at least one internal standard per lipid class. The complete list of identified lipids is included in **Table S2.3**, along with detailed relevant information, including alternative IDs from the same level of identification in *LiPydomics*. The breakdown of

identified lipid species is displayed in **Figure 2.4,** colored by their lipid category and class, with fatty acyls in purple, glycerolipids in red, glycerophospholipids in green, and sphingolipids in blue. A large number of phosphatidylcholine (PC) and phosphatidylethanolamine (PE) lipids were identified in both ionization modes, as well as TGs in positive mode, reflective of their abundance in the brain. TGs and MGs are detected exclusively in positive mode, while FFAs and CLs are identified exclusively in negative mode.

2.2.2. Developmental lipidomic changes in WT and *Dhcr7*-KO mice

Next, we examine the temporal changes in individual lipid levels in the WT and *Dhcr7*-KO mouse brains through four developmental stages. The time points were chosen because *de novo* cholesterol biosynthesis in mouse brains starts at around E11 (Tint et al., 2006), cortical neurogenesis peaks at around E15.5 (Dehay & Kennedy, 2007; Finlay & Darlington, 1995; Molyneaux et al., 2007), and myelination starts at PND0 (Foran & Peterson, 1992). One limitation of the *Dhcr7*-KO mouse model used here is that KO pups cannot survive past the first day of birth, which prevents examination of lipidomic changes beyond PND0. Heat maps with hierarchical clustering were generated to visualize the variation of lipid levels across the developmental time points, as seen in **Figure 2.5** and **Figure 2.6**. The relative lipid intensities after normalization were used, and heat maps were clustered by the default Euclidean distance method, row-centered, and unit variance scaled by row. Heat maps are helpful in visualizing temporal patterns across the four time points and identifying differences in the patterns between genotypes, where darker colors correspond to relatively high levels and lighter colors correspond to relatively low levels.

For FFAs in WT, shown in **Figure 2.5A**, about half of them are the highest at E16.5, including polyunsaturated fatty acids (PUFA) such as FFA 20:4 and FFA 22:6, while others are

the highest at E12.5, including two monounsaturated fatty acids (MUFA), FFA 16:1 and FFA 18:1. In the KO, however, many PUFA species, including 20-carbon containing FFAs, reach the highest levels at PND0. Interestingly, 18-carbon-containing FFAs are at their peak at E16.5 in the KO, including FFA 18:2 and FFA 18:3.

Most of the glycerolipids (**Figure 2.5B**), including diacylglyceride (DG) and TG species, are the highest at the earlier time points in the WT. However, there is a cluster of TGs, with higher degrees of unsaturation in their fatty acyl chains, that peak at E16.5, suggesting fatty acyl-dependent variation within the class. Most MGs had high levels at both E12.5 and E16.5 time points. The unsaturated 20-carbon-containing MGs were much higher at all time points in the KO compared to the WT, similar to the unsaturated, shorter chain DG(20:1). However, for other DGs and TGs, WT and KO heat maps show similar trends across all time points.

Developmental patterns of sphingolipids are shown in **Figure 2.5C**. In WT, Cer species either peak at E14.5 or PND0; furthermore, Cer(d36:2), Cer(d36:1), and Cer(d38:2) go from low to high with the developmental time points, while Cer(d34:1) and Cer(d40:1) display the opposite trend. Most HexCer species are the highest at E12.5, except for HexCer(d36:1), which increases throughout E16.5 but drops at PND0, while most SM species gradually increase from early to later time points and reach the highest levels at PND0. The sphingolipid heat maps of WT and KO are largely consistent in terms of their temporal patterns. Still, there are differences in some species' intensities at certain time points, which are discussed further in the following section.

Due to the large number of glycerophospholipids identified in this study, we chose only a few of the most common lipid classes to present in **Figure 2.6**. Many of the glycerophospholipid classes, including PE, PC(O/P), and PG, are similarly separated into two clusters, either starting

high and decreasing or starting low and increasing throughout the WT time course, but there are no apparent patterns based on fatty acid composition. WT and KO heat maps within each subclass exhibit a high degree of similarity. The CL and PG (precursor to CL) subclasses have visually distinct patterns than other classes, with most species being at the highest levels at E12.5 and decreasing through PND0.

Overall, many lipid species displayed unique temporal patterns throughout the developmental time course from E12.5 to PND0. Notably, the peak of many lipids at E16.5 in WT, including FFA 22:6 and other polyunsaturated lipids, seems to be concurrent or coinciding with the peak of neurogenesis processes. The elucidation of the developmental patterns of each lipid class provides important knowledge for understanding their roles during neurodevelopment in future studies.

2.2.3. Differentially expressed lipid species between WT and *Dhcr7*-KO mouse brains

PCA analysis of all groups of data showed good separation according to genotype and time point (**Figure 2.7**). Computation of empirical Bayes-adjusted contrasts between the two genotypes at each time point revealed differentially expressed lipids at each time point at an FDR (adjusted p-value) of < 0.05 (**Table S2.4**).

The number of significantly altered lipids increases from E12.5 to PND0 time points, with PND0 having the most in both positive (17 lipids) and negative (12 lipids) modes (**Figure 2.8**). In positive mode, 2-6 MG species were found to be significantly increased in *Dhcr7*-KO brains depending on the developmental day, including the endocannabinoid, 2-arachidonoylglycerol (2-AG), or MG(20:4). Furthermore, at PND0, SM(d36:2), HexCer(d36:2), and Cer(d34:1) were significantly decreased in *Dhcr7*-KO brains compared to WT. In negative mode, five FFAs (20:1, 20:2, 20:3, 22:4, and 22:6) display significantly higher levels in the

Dhcr7-KO brains at PND0. In addition, some PE species were found to be significantly decreased, while LPE species were found to be significantly increased in the *Dhcr7*-KO brains. Subsequently, using linear regression using a 2-df spline, we found that three of the MG species (20:3, 24:6, and 20:2) that were determined to be significantly altered at one or more time points in the ANOVA analysis display genotype-dependent changes across development as a whole (**Figure 2.9**). For all three MGs, the lipid abundances remain relatively constant or slightly decrease for WT mice. In contrast, they increase in KO mice as they approach parturition, thus showing that the trends differ between the two genotypes.

Several features with the *m/z* and early retention times of oxysterol metabolites of 7-DHC show significant elevations in *Dhcr7*-KO brains (**Figure 2.10**), as expected by the primary biochemical defect and high oxidation reactivity of 7-DHC in SLOS. *m/z* 399 could arise from the dehydration of the parent ion (*m/z* 417) of a major 7-DHC oxysterol found in *Dhcr7*-KO mouse brains, 3β,5α-dihydroxycholest-7-en-6-one (DHCEO) while *m/z* 365 could arise from loss of 2 H_2O from 7-DHC+O (such as hydroxylated 7-DHC) or loss of one H_2O from 7-dehydrodesmosterol (Xu et al., 2013; Xu, Korade, et al., 2011). However, because HILIC cannot separate the individual sterols and oxysterols, we cannot assign the exact identities of these features. Regardless, this result is consistent with previous targeted LC-MS/MS experiments that showed oxysterol accumulation in *Dhcr7*-KO mouse brains at high levels (Xu et al., 2013; Xu, Korade, et al., 2011).

2.2.4. Pathway analysis and biological implications

Pathway analyses on the differentially expressed lipids were carried out using MetaboAnalyst and LIPEA (Acevedo et al., 2018; Pang et al., 2021). Similar metabolic pathways were found to be significantly impacted by *Dhcr7*-KO using both methods: glycerophospholipid

metabolism, glycerolipid metabolism, and sphingolipid metabolism (**Figure 2.11** and **Table S2.5**). LIPEA also identified potentially affected biological processes, such as the sphingolipid signaling pathway, neurotrophin signaling pathway, and glutamatergic synapse. While LIPEA has a built-in conversion tool that converts general lipid names to KEGG IDs, for MetaboAnalyst, we directly input relevant KEGG IDs. Note that in both pathway analyses, lipids from the same class are represented by only 1-2 KEGG ID rather than a specific KEGG ID per individual lipid species; therefore, the lipid class, MG, is underrepresented in the pathway analysis since there are six MGs that were significantly altered. MGs are an important class of lipid signaling molecules in the CNS, involved in both physiological processes, such as neurotransmission, and pathological processes in neurological disease (Poursharifi et al., 2017). 2-AG, in particular, is a key mediator of the endocannabinoid signaling pathway at neuronal synapses (Castillo et al., 2012). However, whether the changes in MG levels contribute to the neurological defects in SLOS patients remains to be examined.

The alteration in sphingolipid metabolism and signaling appears to be closely relevant to SLOS pathophysiology. Sphingolipids and cholesterol are the main components of membrane microdomains, or lipid rafts, that are critical for neurodevelopment and neuronal signaling (Olsen & Faergeman, 2017). Compartmentalization of signaling proteins is required for normal neuronal physiology, polarization, synapse formation, and synaptic signaling. In a previous work, Keller et al. found that there are significantly different protein profiles associated with the lipid rafts between the brains of a SLOS rat model and those of the control rats, suggesting altered lipid raft structure and function (Keller et al., 2004). The authors also found that 7-DHC displays similar efficiency in forming lipid rafts, so it is possible that the decreased levels in sphingolipids may contribute to the observed changes in lipid raft structure and function.

Notably, in a different *Dhcr7*-KO mouse model from this study, it was found that mutant cortical neurons' response to glutamate is significantly reduced relative to control neurons, while the expression of the receptors did not change, suggesting defective synaptic signaling (Wassif et al., 2001). Whether such defects are related to the altered lipid raft function remains to be examined. Furthermore, as major components of myelin, the reduced levels of SMs and cholesterol may affect myelination in SLOS (O'Brien et al., 1965). Although myelination defects have not been observed in the limited studies of SLOS patients (Lee, Conley, et al., 2013), the MRI characteristics of SLOS patients are similar to those of other neurological disorders with myelination defects (Dang Do et al., 2018), and white matter lesions have been previously reported in SLOS patient brains (Dang Do et al., 2018).

The decreases in the levels of PEs and increases in the levels of lyso-PEs and FFAs suggest upregulation of the phospholipase A_2 (PLA_2) activity. The activities of PLA_2, releasing FFAs and lysophospholipids, are known to play important roles in neurotransmission, learning and memory, and neuroinflammation (Joensuu et al., 2020; Solomonov et al., 2016). LPE also induces neuronal differentiation by activating MAPK (Nishina et al., 2006). Interestingly, increased levels of neuroprostanes, lipid peroxidation products of DHA, have been found in *Dhcr7*-KO mouse brains relative to controls at PND0 (Korade et al., 2013), further supporting the evidence of increased inflammation and free radical oxidation in the SLOS mouse brain. Future transcriptomic analysis may shed light on the gene expression changes associated with inflammation and lipid metabolic pathways identified in this work (**Chapter 4**).

2.3 Experimental Procedure

2.3.1. Chemicals

Optima LC/MS grade solvents (acetonitrile, chloroform, methanol, methylene chloride, and water), 2-methylbutane, ammonium acetate, and sodium chloride were purchased from Thermo Fisher Scientific (Grand Island, New York). Lipid standards, as described in (A. Li et al., 2020), were purchased from Avanti Polar Lipids (Alabaster, Alabama) and NuChek Prep (Elysian, Minnesota).

2.3.2. Animals

C57BL/6J and transgenic heterozygous mice with a null mutation for *Dhcr7* (Ex8) mice were purchased from Jackson Laboratories (Bar Harbor, Maine; catalog #007453). The University of Washington Institutional Animal Care and Use Committee approved all animal protocols. Mice were housed in an animal care facility with a 12-hour light and dark cycle and fed an *ad libitum* commercial rodent chow diet. Heterozygous *Dhcr7* (Ex8) mice were mated overnight, where the day after time-mating was designated as E0.5. For embryonic time points (E12.5, E14.5, and E16.5), timed pregnant female dams were euthanized by CO_2 asphyxiation, sacrificed by decapitation, and embryos removed from the abdominal cavity into 1x PBS at the appropriate gestational age. For the postnatal day 0 (PND0) time point, neonates were removed from their cages on the day of birth, euthanized on ice, and sacrificed by decapitation under hypothermal conditions. Brains were dissected, flash frozen in 2-methylbutane on dry ice, weighed, and stored at -80°C until analysis. Other tissue samples were collected from embryos and neonates for genotyping following an established protocol (Fitzky et al., 2001). Briefly, embryonic tissue was digested in a lysis solution for 2 hours at 100°C in a thermocycler, PCR was performed with extracted DNA, primers, and master mix, and the PCR product was

analyzed by agarose gel electrophoresis to determine the genotype: *Dhcr7*$^{-/-}$ (KO), *Dhcr7*$^{+/-}$ (Het), and *Dhcr7*$^{+/+}$ (WT). Four biological replicates for each genotype were collected from multiple litters at each time point. No power analysis calculation was used to estimate sample size due to the unknown effect size in this exploratory study.

2.3.3. Tissue Sample Preparation

E16.5 and PND0 brains were cut in half along the sagittal midline due to their large size, while E12.5 and E14.5 whole brains were used. Tissue weights can be found in **Figure 2.2** and **Table S2.2**. Frozen brain tissues were homogenized in tubes containing ceramic beads using the Precellys Tissue Homogenizer. Samples were kept on dry ice at all other times. 1.5 mL of homogenization solvent (1:2 chloroform/methanol, v/v) was added, along with 100 μL of internal standard [C12 sphingosyl-PE (d17:1/12:0), 1 mM]. Samples were vigorously shaken at 6800 rpm for three cycles of 30 seconds with 60 seconds pause in between. Tissue homogenates were transferred to 10 mL glass centrifuge tubes for lipid extraction. Briefly, 4 mL of Folch solution (2:1 chloroform/methanol, v/v) and 1 mL of sodium chloride solution (0.9%, w/v) were added to each tube. Samples were vortexed for 30 seconds and then centrifuged at 2000 *g*. The bottom organic layers were transferred by glass pipette to new glass tubes and dried for two hours in a speed vacuum concentrator (Savant SpeedVac® SC210A; Thermo Fisher Scientific). Samples were reconstituted in 1.5 mL of methylene chloride and stored at -80°C until analysis.

2.3.4. HILIC-IM-MS Lipidomics Analysis

Lipidomics analysis was performed as previously described in detail (K. Hines et al., 2017; A. Li et al., 2020). Samples were diluted in autosampler vials to 10:100 in HILIC A (95:5 ACN/H_2O, 5 mM ammonium acetate) buffer for analysis. Quality control samples were made by pooling aliquots of all samples and were analyzed intermittently throughout the MS run. Each

biological replicate was analyzed once per ionization mode. Samples were analyzed on the Waters Synapt G2-Si IM-QTOF in both positive and negative ionization modes. Post-acquisition data processing was performed by Progenesis QI software for peak picking, alignment, and multivariate statistical analysis using R and EZInfo. Lipid identifications were made by similarity matching of *m/z*, retention time, and CCS using various databases, including our own in-house CCS database, CCSbase (https://CCSbase.net), and an automated lipidomics data processing Python package, *LiPydomics* (https://github.com/dylanhross/lipydomics) (Ross, Cho, Zhang, et al., 2020). Lipid signal abundances were normalized by a factor combining the intensity of the internal standard in the sample and the brain tissue weight (**Table S2.2**). The single internal standard, N-lauroyl-D-erythro-sphingosyl phosphoethanolamine [sphingosyl-PE (d17:1/12:0)], separated well from other lipid classes of interest and was added to account for sample processing and technical variation, to capture relative differences between WT and KO samples (Cifkova et al., 2012). Peak-picked and aligned raw data from Progenesis QI is shown in **Table S2.1**.

2.3.5. Statistical Analysis and Data Visualization

To account for technical variability, we first converted the lipid abundances to log2 to reduce the weight of highly abundant lipids. Then, we normalized the data by scaling each sample to have the same median. After normalization, principal component analysis (PCA) was carried out to visualize the grouping of each genotype and time point (**Figure 2.7**). To make comparisons between the groups, we used the Bioconductor *limma* package to fit a 'limma-trend' model (Phipson et al., 2016; Ritchie et al., 2015). This method allows us to fit an analysis of variance (ANOVA) model while accounting for any dependence between the mean and variance. We then computed empirical Bayes-adjusted contrasts between the two genotypes at each time

point, where the empirical Bayes adjustment helps improve the by-lipid variance estimates by borrowing information across all the lipids. We selected lipids with a false discovery rate (FDR; adjusted p-value) < 0.05 (see **Table S2.4** for a summary of the significantly different lipids) (Benjamini & Hochberg, 1995). To identify lipids that show genotype-dependent temporal changes in abundance, we fit a linear regression using a 2-df (degrees of freedom) spline, which allows the fitted line to curve in one direction.

Plots were made using R 3.5.0 (R Core Team, 2018). We generated our heat maps in R program and modeled them after the open-source web tool, ClustVis (https://biit.cs.ut.ee/clustvis/) (Metsalu & Vilo, 2015).

2.4 Conclusion

In this lipidomics study, we applied our untargeted HILIC-IM-MS method to characterize the murine lipidome during normal brain development and in a model of the human disorder SLOS. Of the 2,521 and 4,867 features detected in both positive and negative modes, 272 and 280 lipid adducts (401 unique lipids) were identified by lipid class and fatty acyl sum composition. We utilized the *LiPydomics* Python package to automate several steps of data analysis, including multi-levels of normalization and Level 3 lipid identification using *m/z*, RT, and CCS, by searching against the extensive predicted lipid database in the package. This marks the first study to investigate the developmental changes that occur during time points that span neurogenesis after *de novo* cholesterol biosynthesis starts. It is clear from this study that fatty acid composition, particularly their degrees of unsaturation, has some bearing on the temporal patterns of lipids displayed throughout development, which could indicate their different functions and roles during development. Additionally, pathway analysis of differentially expressed lipid species between WT and SLOS mouse brains suggests altered glycerolipid,

sphingolipid, and glycerophospholipid metabolism, which have implications in synaptic signaling, lipid raft formation, myelination, and inflammation in SLOS pathophysiology.

Figures

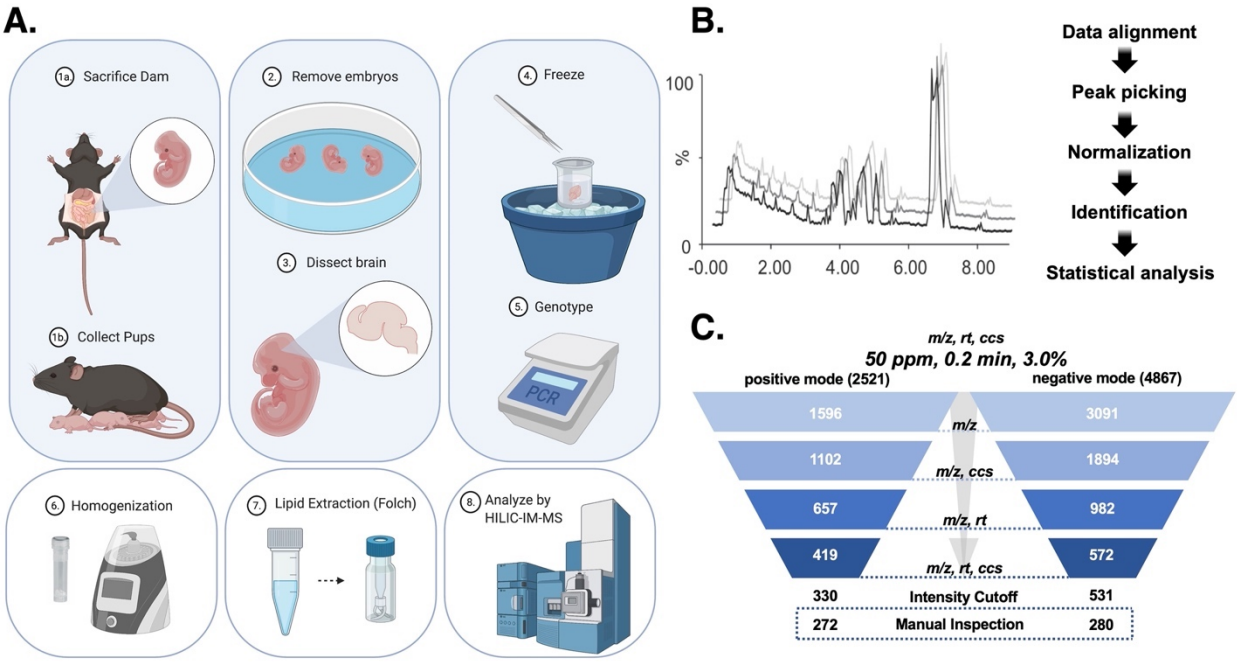

Figure 2.1 Schematic of the workflow from **A.** sample preparation (i.e., brain dissection, tissue homogenization, lipid extraction, and MS analysis) to **B.** data processing to **C.** data analysis (i.e., Progenesis and *LiPydomics*). C. shows the number of identified features with various stringency levels for identification matching through *LiPydomics* and manual identification. Panel A was created with BioRender.com.

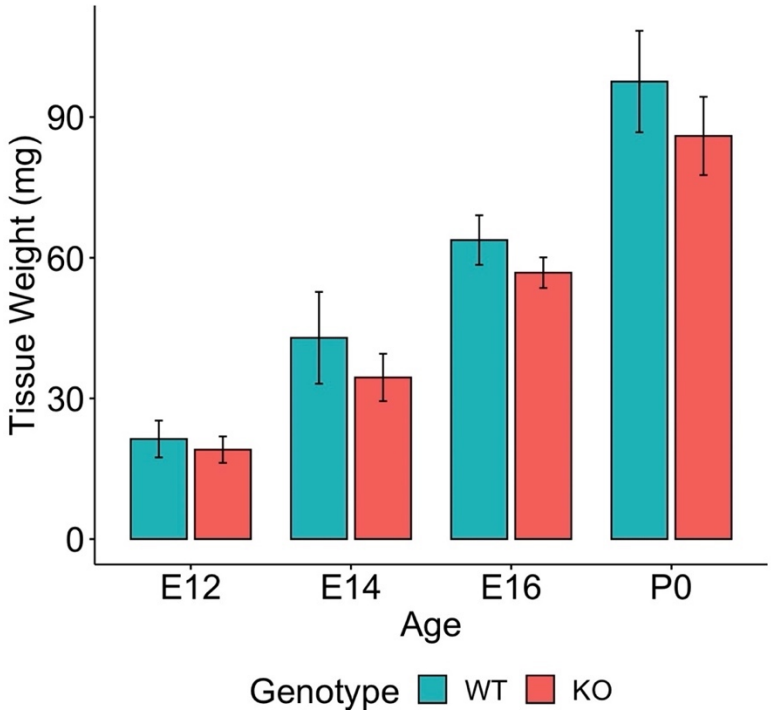

Figure 2.2 Frozen weights of brain tissue samples after dissection; four biological replicates per age group and genotype.

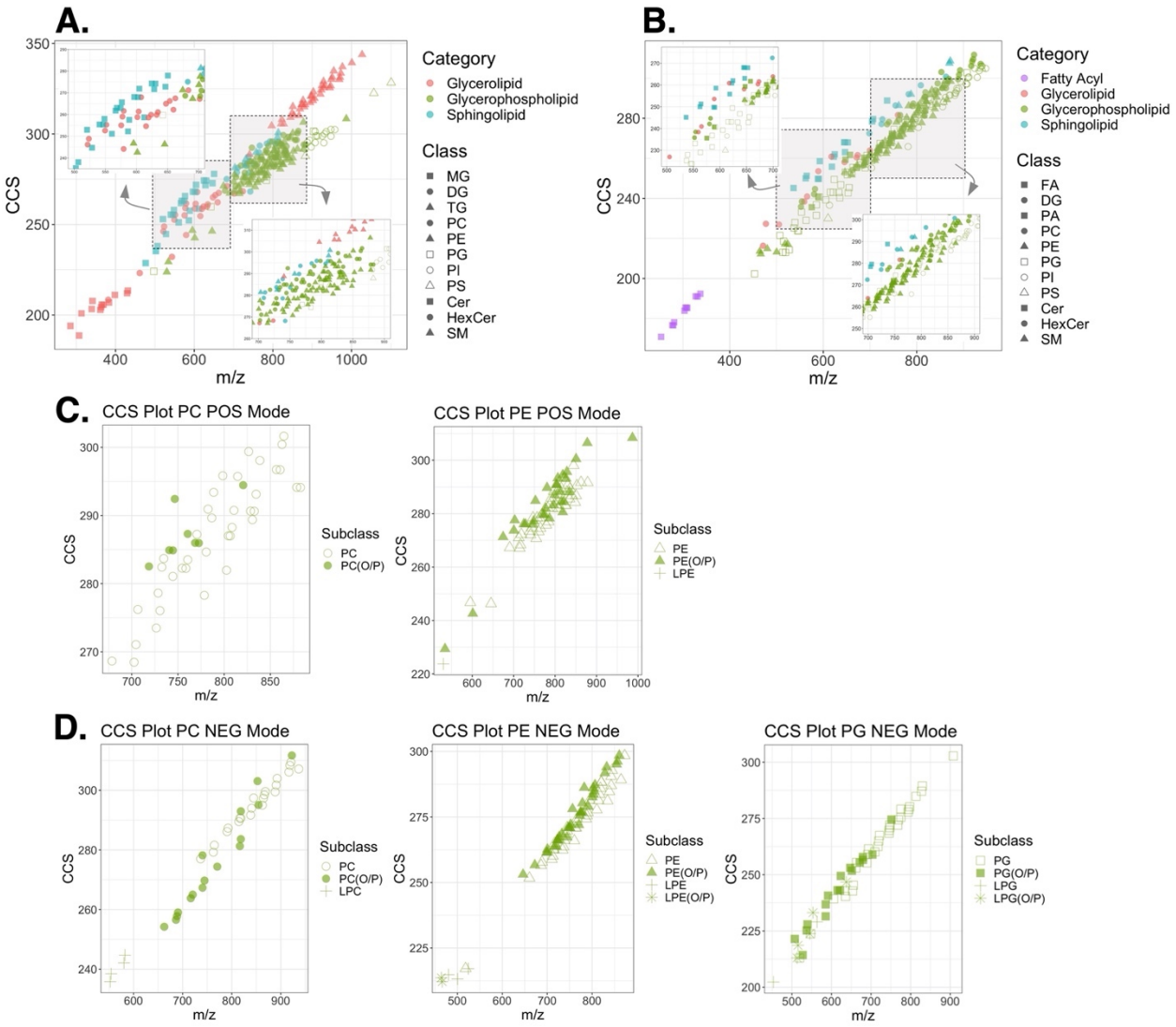

Figure 2.3 IM-MS conformational plot for CCS measurements of lipid species detected in **A.** positive and **B.** negative ionization modes. Colors differentiate the lipid categories, while point shapes differentiate the lipid classes. Individual CCS plots for PC, PE, and PG lipids to distinguish acyl-, plasmenyl/plasmanyl-, and - subclasses in **C.** positive and **D.** negative ionization modes.

For simplicity, plasmalogen (both plasmenyl and plasmanyl) and lyso-glycerophospholipid species were grouped within the same class; however, these subclasses are further broken down for PC, PE, and PG lipids.

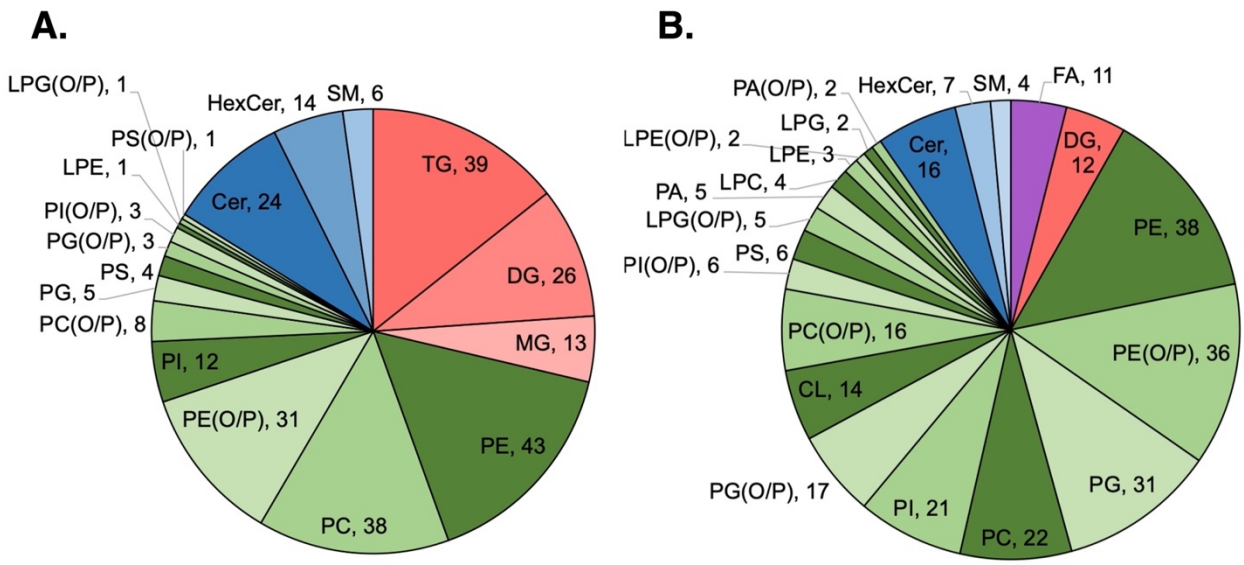

Figure 2.4 Breakdown of lipid identifications made in **A.** positive and **B.** negative ionization modes across the major categories of lipids.

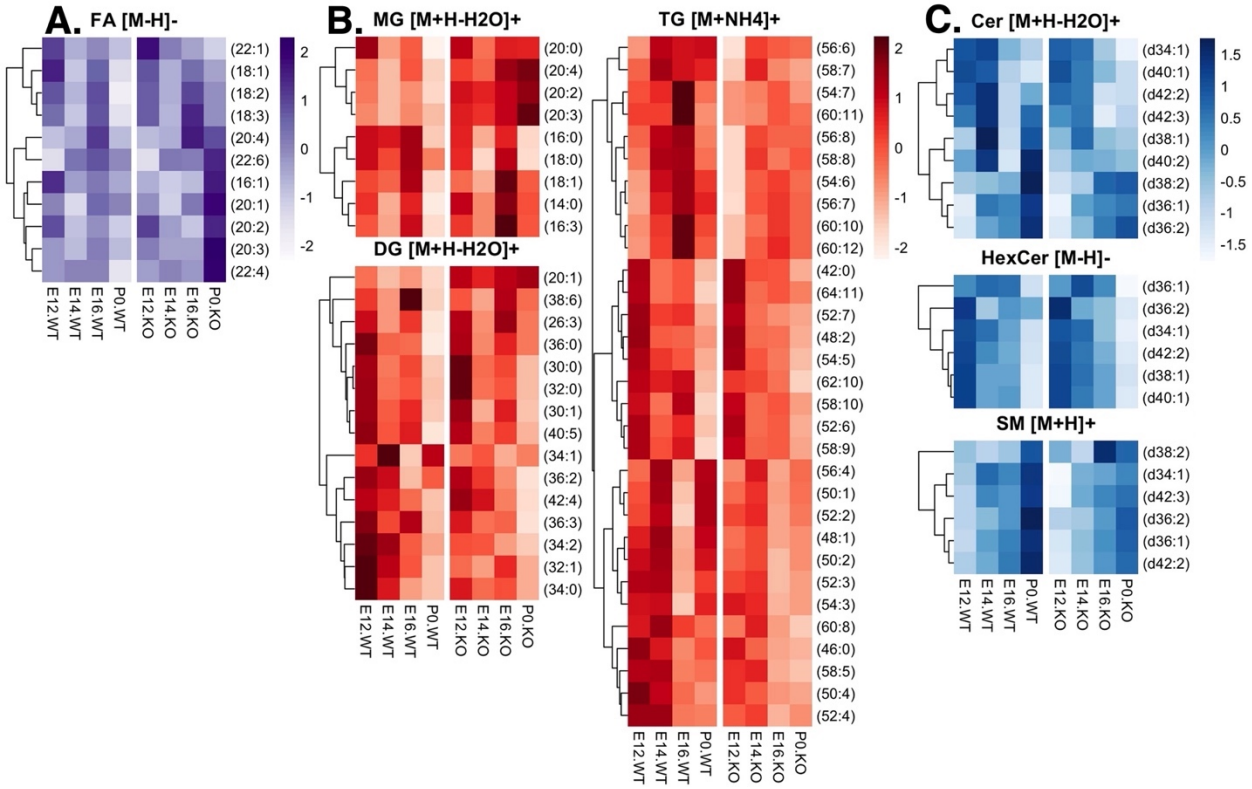

Figure 2.5 Heat maps for major lipid classes (fatty acyls, glycerolipids, and sphingolipids) showing temporal patterns of lipid composition during neurodevelopment across the four time points in WT and *Dhcr7*-KO mice (n = 4 per time point per genotype). Heat maps were generated using unit variance scaling by row.

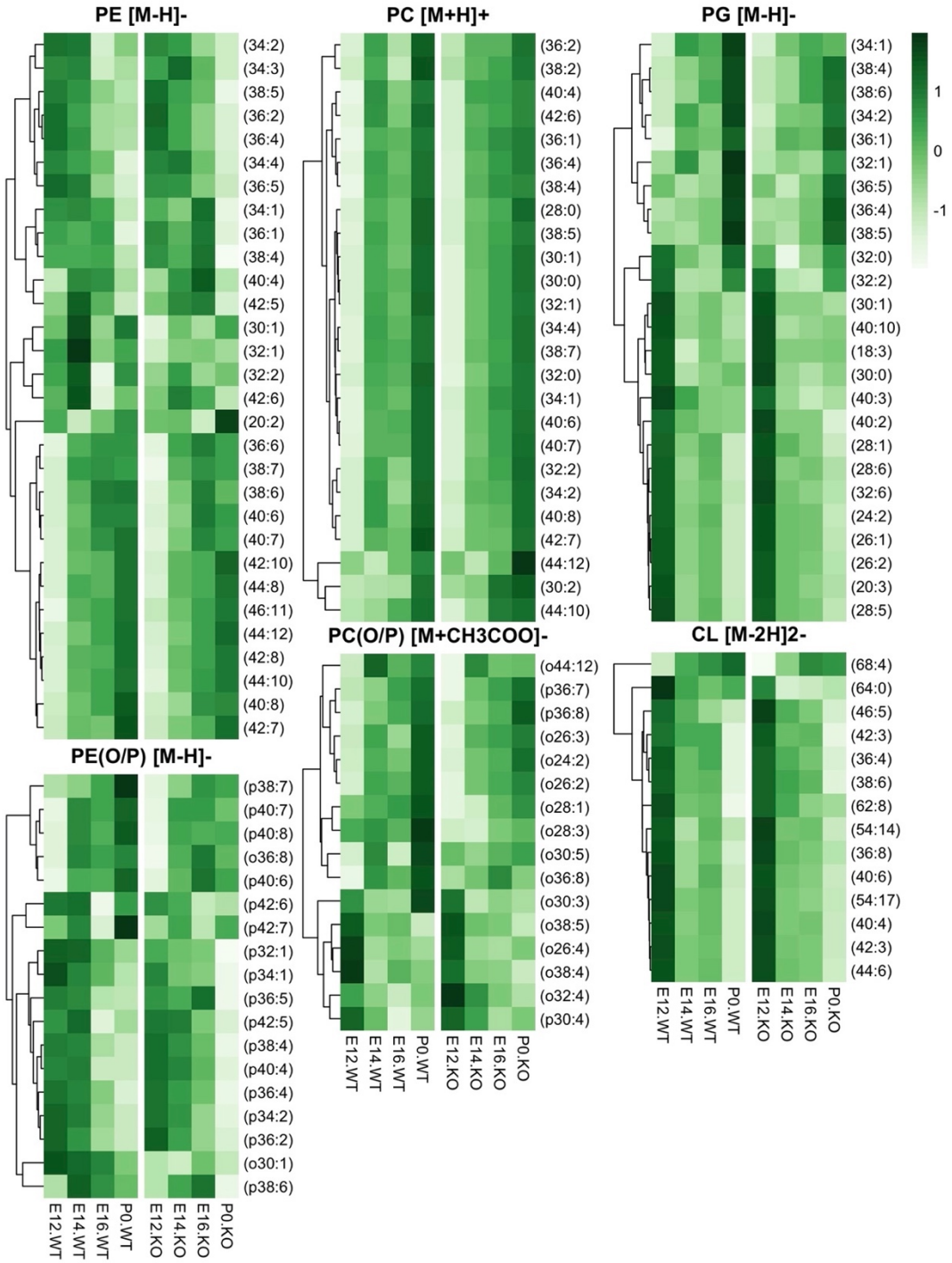

Figure 2.6 Heat maps for glycerophospholipids showing temporal patterns of lipid composition during neurodevelopment across the four time points in WT and *Dhcr7*-KO mice (n = 4 per time point per genotype).

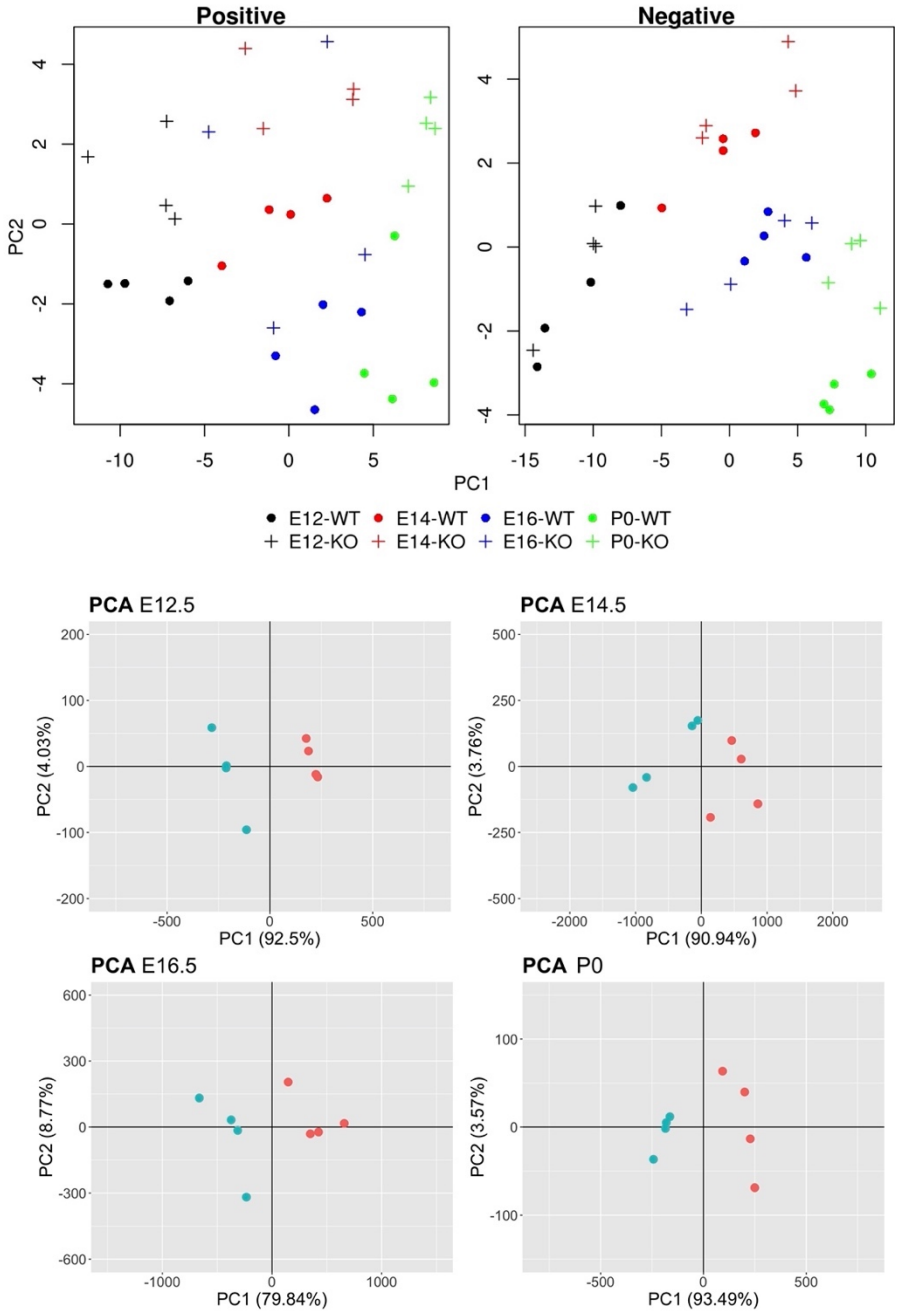

Figure 2.7 Principal component analysis (PCA) of WT and *Dhcr7*-KO samples grouped by age and genotype for both positive and negative ionization modes. Principal component analysis (PCA) of WT and *Dhcr7*-KO samples grouped by age from positive ionization mode and filtered by an ANOVA p-value of 0.05.

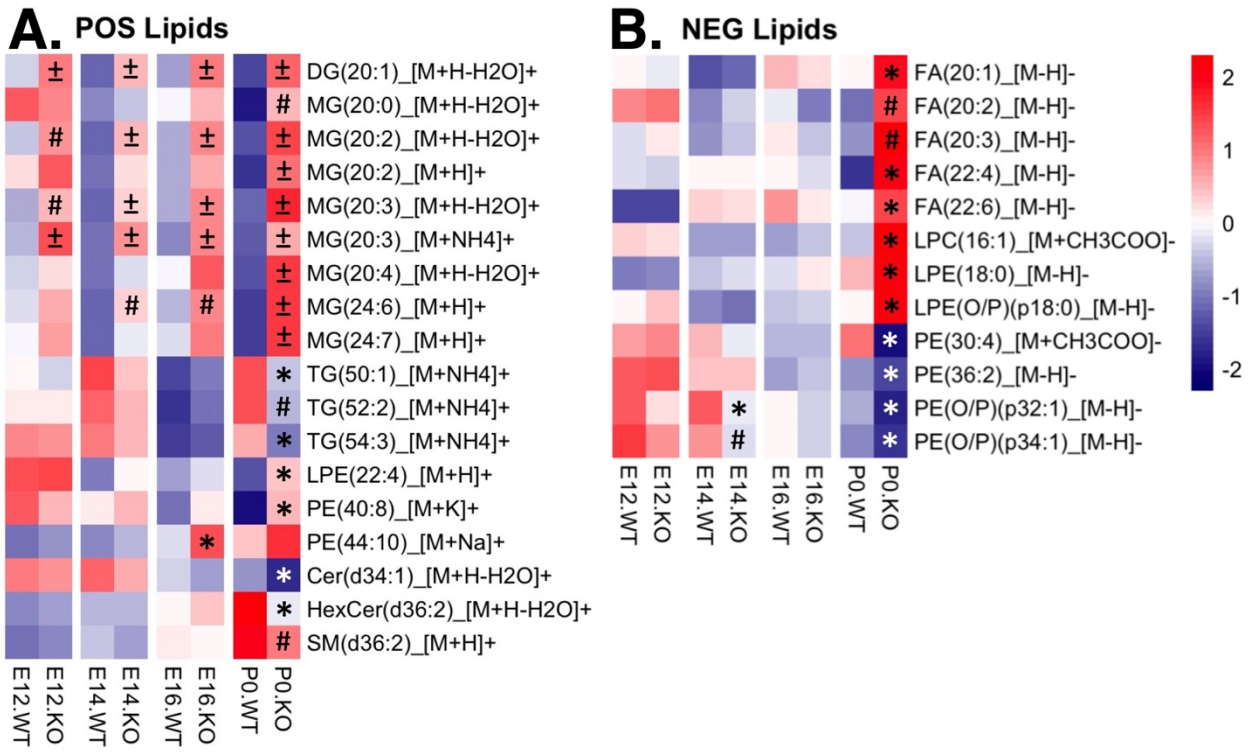

Figure 2.8 Heat maps of significantly altered lipids (FDR < 0.05) in **A.** positive and **B.** negative ionization modes comparing WT and *Dhcr7*-KO mice at each developmental time point.
* $P < 0.05$, # $P < 0.005$, ± $P < 0.0005$.

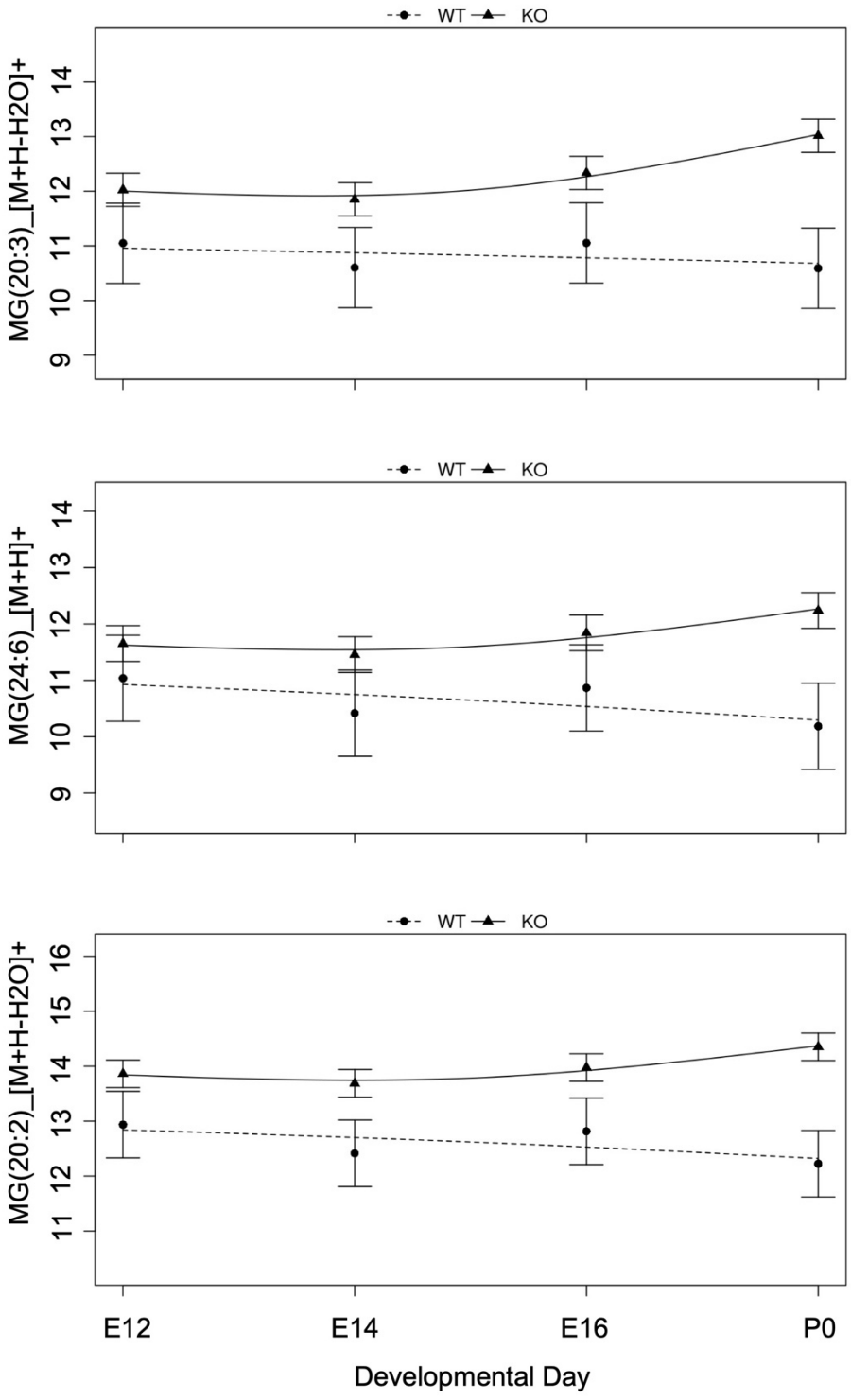

Figure 2.9 Linear regression fit using a 2-df spline for three MG compounds with a significant genotype-dependent change in abundance across developmental time points, plotting the mean and 95% confidence interval.

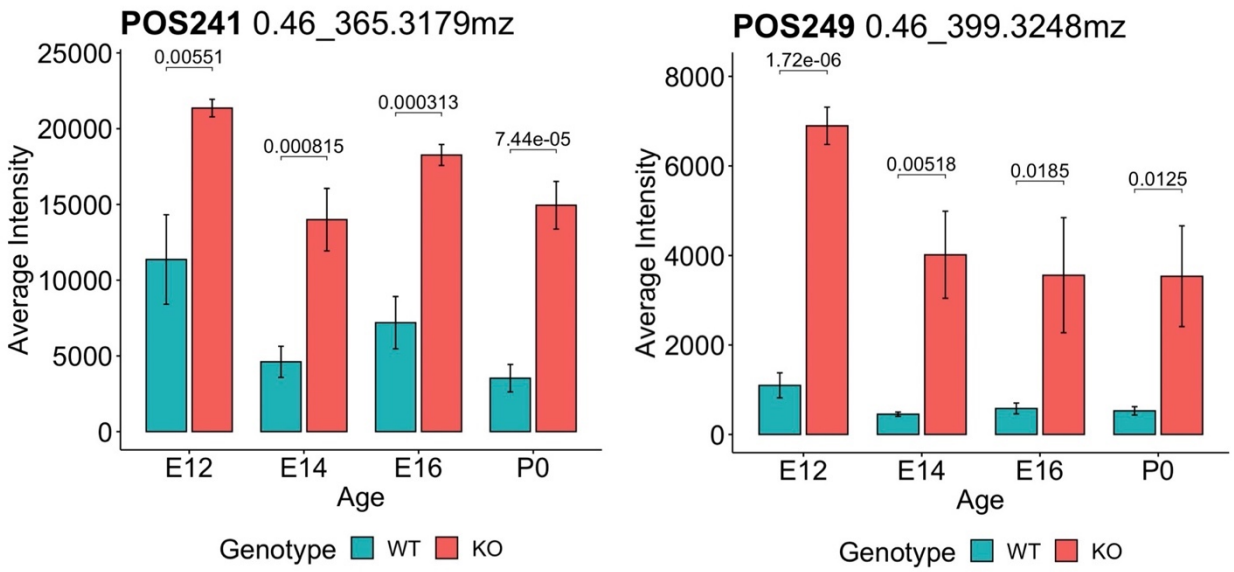

Figure 2.10 Bar plots comparing relative amounts of two oxysterol species (denoted by its compound number, retention time, and *m/z* value) in WT and *Dhcr7*-KO samples.

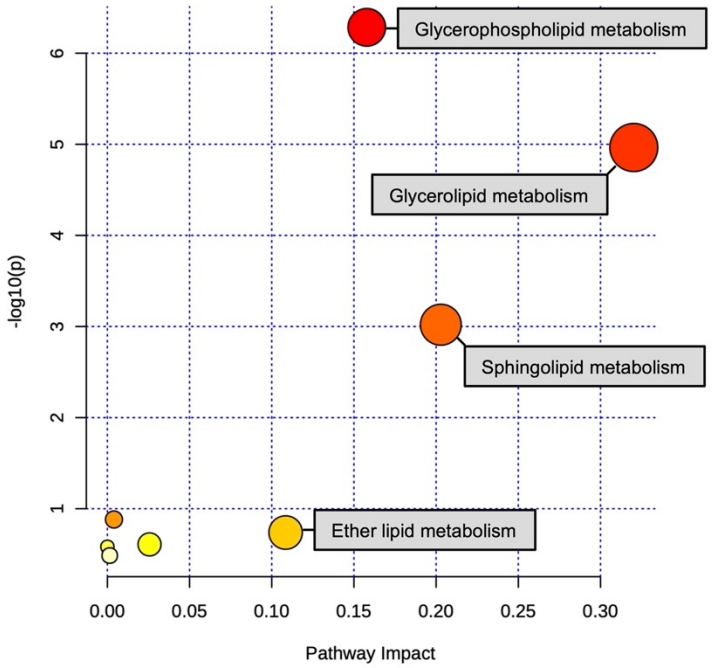

	Total	Expected	Hits	Raw p	-log10(p)	Holm adjust	FDR	Impact
Glycerophospholipid metabolism	36	0.36	6	5.20E-07	6.28E+00	4.37E-05	4.37E-05	0.16
Glycerolipid metabolism	16	0.16	4	1.08E-05	4.96E+00	9.00E-04	4.55E-04	0.32
Sphingolipid metabolism	21	0.21	3	9.56E-04	3.02E+00	7.84E-02	2.68E-02	0.20
Glycosylphosphatidylinositol (GPI)-anchor biosynthesis	14	0.14	1	1.31E-01	8.82E-01	1.00E+00	1.00E+00	0.00
Ether lipid metabolism	20	0.20	1	1.82E-01	7.39E-01	1.00E+00	1.00E+00	0.11
Phosphatidylinositol signaling system	28	0.28	1	2.46E-01	6.08E-01	1.00E+00	1.00E+00	0.03
Inositol phosphate metabolism	30	0.30	1	2.62E-01	5.82E-01	1.00E+00	1.00E+00	0.00
Fatty acid degradation	39	0.39	1	3.27E-01	4.86E-01	1.00E+00	1.00E+00	0.00

Figure 2.11 Pathway analysis of significantly altered lipids using MetaboAnalyst. Pathway enrichment was calculated by hypergeometric test and plotted on the y-axis as -log(p). Pathway topology analysis used relative betweenness centrality and plotted on the x-axis as pathway impact value.

Tables

Excel spreadsheet tables are accessible as Supporting Info in the publication:

> Amy Li, Kelly M. Hines, Dylan H. Ross, James W. MacDonald, and Libin Xu, Temporal changes in the brain lipidome during neurodevelopment of Smith-Lemli-Opitz syndrome mice, *Analyst*, 147:1611–1621, (**2022**). https://doi.org/10.1039/D2AN00137C.

Table S2.1 Raw HILIC-IM-MS datasets for positive (1st tab) and negative (2nd tab) ionization modes, with all features detected in Progenesis, and their mass-to-charge (Da), retention time (min), collision cross section values (Å^2), and intensities for each sample.

Table S2.2 Tissue weights and C12 sphingosyl-PE IS abundances used for normalization of lipid intensities.

Table S2.3 Lipid identifications from *pred_mz_rt_ccs* matching in *LiPydomics* and after manual filtering of annotations, in positive (1st tab), negative (2nd tab), and both ionization modes (3rd tab).

Table S2.4 Significantly altered lipids (FDR < 0.05) from ANOVA analysis for each time point, with logCPM (average log abundance), logFC (log fold-change), adjusted p-value, and average log abundances for WT and KO groups.

Table S2.5 Results of enriched KEGG pathways from LIPEA pathway analysis of significantly altered lipids.

Chapter 3 MALDI-IM-MS Imaging of Brain Sterols and Lipids

Portions of this chapter have been deposited as a preprint at bioRxiv:

> Amy Li and Libin Xu, MALDI-IM-MS Imaging of Brain Sterols and Lipids in a Mouse Model of Smith-Lemli-Opitz Syndrome, *bioRxiv*, (**2023**). doi:10.1101/2023.10.02.560415.

3.1 Introduction

Smith-Lemli-Opitz syndrome (SLOS) is a multiple malformation disorder caused by genetic mutations in the *DHCR7* gene, encoding the enzyme 3β-hydroxysterol-Δ^7-reductase (DHCR7) that catalyzes the final step in cholesterol synthesis (F. D. Porter et al., 2011; Thurm et al., 2016). The biochemical hallmark of SLOS is cholesterol deficiency and accumulation of the precursor to cholesterol, 7-dehydrocholesterol (7-DHC), and during brain development, 7-dehydrodesmosterol (7-DHD) (Irons et al., 1993; Tint et al., 1994; Tint et al., 1995; Tomita et al., 2022). Due to its high reactivity towards free radical oxidation (Xu et al., 2009), 7-DHC also gives rise to many other oxidized metabolites, known as oxysterols (Xu et al., 2010; Xu et al., 2013; Xu, Korade, et al., 2011; Xu, Liu, et al., 2011), among which 3β,5α-dihydroxycholest-7-en-6-one (DHCEO), 4α-hydroxy-7-DHC, and 4β-hydroxy-7-DHC are the major ones observed in embryonic and postnatal day 0 (PND0) *Dhcr7*-KO mouse brains (Tomita et al., 2022). Oxysterols, whether produced enzymatically or non-enzymatically, are known to play both a pathological and physiological role in the brain and other tissues (Bjorkhem et al., 2009; Brown & Jessup, 1999; Raleigh et al., 2018; Sacchetti et al., 2009). Thus, the effects of blocking cholesterol synthesis at the level of DHCR7 can be viewed as two-fold: depletion of a critical cellular molecule, cholesterol, and accumulation of 7-DHC and its derived oxysterols to potentially toxic levels.

With over 100 genetic mutations of DHCR7 discovered to date (Waterham et al., 2012; Witsch-Baumgartner et al., 2000; Yu et al., 2000), the genotypic variability of SLOS is expansive, ranging from point mutations to splice site mutations to null mutations that can lead to reduced enzyme activity, expression, or complete absence of the enzyme. Thus, individuals diagnosed with SLOS can exhibit a wide range of phenotypes across several organ systems due to the essential role of cholesterol during development (Cooper et al., 2003; J. A. Porter et al., 1996). The central nervous system (CNS) is one of the most severely affected organs in SLOS because the brain synthesizes cholesterol locally and independently. The CNS phenotype manifests as cognitive and behavioral deficits (ranging from autistic behaviors to severe developmental delay), as well as gross anatomical defects such as agenesis of the corpus callosum (F. D. Porter et al., 2011). This highlights the essential role of cholesterol in brain development. *De novo* cholesterol synthesis begins early in mouse embryonic development (Tint et al., 2006), and accumulation of 7-DHC-derived oxysterols has been observed as early as E12.5 in *Dhcr7*-KO mouse brain (Tomita et al., 2022). This early accumulation of 7-DHC-derived oxysterols in SLOS was shown to be toxic to neuronal cells and cause decreased proliferation and premature differentiation of neural precursor cells (Tomita et al., 2022; Xu et al., 2012).

The *Dhcr7*^{tm1Gst} (*Dhcr7*^{Ex8}) mouse model of SLOS is equivalent to the IVS8-1G>C mutation in humans and is associated with a severe phenotype, causing postnatal lethality within 24 hours of birth in homozygous mice. In **Chapter 2**, we conducted an untargeted lipidomics study of the brain over the time course of development in this mouse model of SLOS using hydrophilic interaction liquid chromatography-ion mobility-mass spectrometry (HILIC-IM-MS) (A. Li et al., 2022). While the study was informative on global changes in various lipid classes and species as embryonic development progressed, whole brain tissue homogenization

eliminated the rich spatial information present within the brain. Matrix-assisted laser desorption ionization (MALDI)-based mass spectrometry imaging (MSI) allows spatial information of endogenous metabolites to be preserved and is thus well suited for studying the changes in the distribution and abundance of various brain lipids in the SLOS mouse model. This study represents a crucial step in understanding how the brain regions are differentially affected by the loss-of-function mutation in *Dhcr7* and the role of lipid metabolism in the overall pathophysiology of SLOS.

However, relative to LC-based lipidomics, MALDI lacks the chromatographic separation of analytes, which presents a challenge for the identification of lipids because most lipids are observed in a narrow mass range of 600-900 Dalton. Coupling MALDI with IM-MS provides an additional dimension of separation of lipids without significantly decreasing the throughput. IM separates ions based on their collision cross sections (CCS) with an inert background gas, which is dependent on the size and shape of the ions and the specific gas. It has been demonstrated that different classes of lipids tend to occupy different chemical spaces in the CCS-*m/z* plot (K. Hines et al., 2017; Kyle et al., 2016; Leaptrot et al., 2019; Ross, Cho, Zhang, et al., 2020; Zhou et al., 2017), which can be used to enhance the confidence of lipid identification.

This work aims to map the regional distribution of sterols and lipids using MALDI-IM-MS. We first successfully determined the distribution of cholesterol and its precursors, as well as the *m/z* values corresponding to the oxysterol metabolites of 7-DHC. We then identified lipids using *m/z* and CCS at the Lipid Species-level (lipid class/subclass and fatty acid sum composition) according to the Lipidomics Standards Initiative (Liebisch et al., 2013) and curated a database of MALDI-IM-MS-derived lipid CCS values. Subsequent statistical analysis revealed differentially expressed lipids between *Dhcr7*-KO and WT mouse brains.

3.2 Results

3.2.1. Confirmation of biochemical hallmark in *Dhcr7*-KO mouse brains

The biochemical hallmarks of *Dhcr7*-KO in the SLOS mouse brains compared to the wild-type are decreased levels of cholesterol and increased levels of 7-DHC and 7-DHD, the precursors to cholesterol in the Kandutsch-Russell and Bloch pathways, respectively. To facilitate the identification of these sterols, we first analyzed standards of cholesterol, three precursor sterols (7-DHD, desmosterol, and 7-DHC), and three major 7-DHC-derived oxysterols (DHCEO, 4α-hydroxy-7-DHC, and 4β-hydroxy-7-DHC) previously observed in *Dhcr7*-KO mouse brains (Tomita et al., 2022) using MALDI-IM-MS with CHCA as the aqueous matrix. The *m/z* and CCS values of major peaks found from authentic standards are shown in **Figure 3.2A**, which are mostly $[M+H-H_2O]^+$ or further dehydration ions, as well as dehydrogenation ions for 7-DHC. For sterols, major peaks correspond to the loss of one or two water molecules from the molecular ion ($[M+H-H_2O]^+$ or $[M+H-2H_2O]^+$), and for 7-DHC, a dehydrogenation ion ($[M+H-H_2O-2H]^+$) at *m/z* 365.3 was also observed. We note that *m/z* 367.3 is the primary ion formed from both 7-DHC and desmosterol, which complicates the analysis. However, the *m/z* 365.3 is specific to the dehydrogenation ion of 7-DHC, $[M+H-H_2O-2H]^+$, and the dehydration ion of 7-DHD, $[M+H-H_2O]^+$. Although these two isomeric ions were not resolved by TWIM, they can still be used to inform the characteristic sterol distribution in the SLOS mouse brain.

For oxysterols, the molecular ion of DHCEO ($[M+H]^+$) was observed at *m/z* 417.3, as well as peaks for the loss of one or two water molecules (*m/z* 399.3 and 381.3). For 4α-hydroxy-7-DHC and 4β-hydroxy-7-DHC, only the loss-of-water ions were observed at *m/z* 383.3 and 365.3.

Using MALDI-IM-MSI, we were able to localize several endogenous sterols and oxysterols and investigate patterns of distribution in the brain tissue of WT and *Dhcr7*-KO mice, as shown via representative ion image heat maps (**Figure 3.2B** and **Figure 3.3**). The heat map gradient shows the signal intensity of individual pixels within the tissue according to a color scale. Anatomically, cholesterol is abundant in the corpus callosum and anterior commissure structures of the WT mouse, which would be expected for such brain structures that are highly abundant in white matter. On the other hand, the signal intensity for cholesterol is very low on the *Dhcr7*-KO mouse tissue section. The ion image for *m/z* 367, which could arise from 7-DHC in the *Dhcr7*-KO brain and desmosterol in the WT brain, is slightly more intense in the KO than the WT but not completely absent in the WT. On the other hand, the ions at *m/z* 365 and 363 are highly abundant in *Dhcr7*-KO tissue while virtually absent in the WT brain. The ion image for *m/z* 365 is most likely the combined signal from $[M+H-H_2O]^+$ of 7-DHD or the dehydrogenation ion of 7-DHC, $[M+H-H_2O-2H]^+$, while *m/z* 363 could result from the dehydrogenation ion of 7-DHD. The localization pattern of cholesterol precursors in the *Dhcr7*-KO tissue appears to be more diffused compared with that of the cholesterol in the WT tissues. Although the signals are still the most intense in the corpus callosum, they are also abundant in the outer layer of the cortex and ventricular/subventricular zone of the cortex.

Patterns for ion images of *m/z* corresponding to oxysterol compounds (**Figure 3.2C** and **Figure 3.3**), including three peaks (*m/z* 417, 399, and 381) that correspond uniquely to DHCEO ions, are similar to those of 7-DHC and 7-DHD. The molecular ion at *m/z* 417 shows the least amount of signal, while the loss-of-water ions, *m/z* 399 and 381, display good intensities. *m/z* 383 could arise from hydroxylated 7-DHC, which matches the exact mass and CCS values from

pure standards of 4α-hydroxy-7-DHC and 4β-hydroxy-7-DHC. However, their low abundances precluded further investigation via fragmentation to obtain information on specific isomers.

3.2.2. CCS atlas of lipids observed in mouse brains with MALDI

As expected, sterol and oxysterol features showed drastic changes in *Dhcr7*-KO brains compared with WT. However, we are also interested in other lipid species changes due to the lipidomic changes that can result from the loss of *Dhcr7* function. To accomplish this, we first aimed to identify brain lipids observed under MALDI using a combination of *m/z* and CCS. TWIM-derived CCS values of observed features were calibrated with a series of PC and PE standards for positive and negative modes, respectively, as described previously (Hines et al., 2016). Lipids were first identified using *LiPydomics* by setting the tolerance for *m/z* to 30 ppm and CCS to 3.0%. Unidentified features were further checked against *m/z* and CCS values in HMDB, where the CCS values originate from AllCCS (Z. Zhou et al., 2020). **Table S3.1** and **Figure 3.4** summarize all the identified lipids at the lipid species level. As seen in **Figure 3.4**, lipids can be classified based on their location in the CCS-*m/z* plot, similar to what is observed with ESI (K. Hines et al., 2017) in **Chapter 2** (**Figure 2.3**). In the positive mode CCS-*m/z* plot (**Figure 3.4A**), the CCS trend of sterol metabolites is lower than those of phospholipids and sphingolipids, suggesting that they adopt more compact gas-phase conformations due to their fused-ring structures.

From these data, some lipid species with similar *m/z* values but large differences in CCS can be found. For example, *m/z* values of $[M-H]^-$ ions of LPE(22:6) and LPS(18:0) differ by only 0.004%. However, their CCS values differ by 3.3%, which is well within the accuracy of current IM-MS instruments (2% accuracy is generally considered acceptable in the field). As another example, the *m/z* values of $[M+Cl]^-$ ion of PC(34:1) and the $[M-H]^-$ ion of PE(40:4) differ by

0.002%, but their CCS values differ by 3.3%. Other isobaric pairs of lipids with different CCS are listed in **Table S3.2**. Images of selected isobaric pairs are shown in **Figure 3.5** and **Figure 3.6**, demonstrating distinct regional distribution between these pairs. Thus, CCS enabled more confident identification and imaging of isobaric lipids.

3.2.3. Differentially expressed lipids between WT and *Dhcr7*-KO mouse brains

Using multivariate statistical analysis tools, we identified lipid species that were differentially expressed in the *Dhcr7*-KO mouse brains compared to WT. Principal component analysis (PCA) plots for regions-of-interest (ROI) from WT and *Dhcr7*-KO brain sections (four quadrants from one tissue section) show clustering of and separation between the two genotypes along PC1 (**Figure 3.7**). S-plots generated from OPLS-DA (**Figure 3.8A**) revealed differential lipid features that drive the separation between WT and *Dhcr7*-KO brains, where p[1] on the x-axis describes how much a feature influences the separation on the OPLS-DA. p(corr) on the y-axis measures the reliability of that feature as a contributing factor in the model. Features with p(corr) greater than 0.9 or less than -0.9 are denoted with an asterisk in **Supplementary Table 1.** Selective features that display a high correlation with WT (lower left) or KO (upper right) are shown in **Figure 3.8B**, along with the H&E staining of adjacent serial sections. Some features were present only in WT or *Dhcr7*-KO tissue, and others that showed more subtle changes were picked up via S-plot analysis. Additional replicates of the images from a different brain are shown in **Figure 3.9**.

In **Chapter 2**, our HILIC-IM-MS study highlighted specific changes in lipids across developmental time points (A. Li et al., 2022), and we were interested to see if similar changes would be detected via MALDI-IM-MSI but with a spatial resolution component. ESI and MALDI are two fundamentally different ionization sources, which could lead to different

observations of lipids and differences due to ion suppression of low abundant lipids when analyzing the whole brain homogenates. Indeed, we observed significantly decreased levels in several ceramides [e.g., Cer(d36:1)] and significantly increased levels in lysoPC [e.g., LPC(16:1)], and lysoPE [e.g., LPE(p16:0)], species in the KO samples relative to WT, consistent with the lipidomic changes identified using HILIC-IM-MS. The ceramides were most abundant in the corpus callosum (made up of white matter) of WT and appeared to be mostly absent in *Dhcr7*-KO. Another interesting observation was phosphoinositol species detected in the negative ionization mode, where PI(38:4) is upregulated in *Dhcr7*-KO, while the corresponding PI monophosphate, PIP(38:4) is downregulated in *Dhcr7*-KO tissue, which could point to aberrant PI signaling pathways. In general, we also observed increased levels of free fatty acids (FFA) in the *Dhcr7*-KO brains, such as FFA 18:0, 18:1, 20:3, 20:4, and 22:3. Images of other lipid species are shown in **Figure 3.10**.

Ions with similar tissue distributions could be identified using the image correlation feature in HDI. For example, the ions at *m/z* 660 and *m/z* 464 (**Figure 3.10**) have a very high spatial correlation with the cholesterol peak, *m/z* 369, while the ions at *m/z* 351 and *m/z* 495 have high correlation with 7-DHC/7-DHD. These unknown features that had a stark contrast between *Dhcr7*-KO and WT tissues were not identified by any lipid databases. The low abundance of these lipids precluded targeted fragmentation to obtain more structural information. However, it should be noted that these features could be adducts or fragments of cholesterol that are formed either endogenously or during sample processing. Thus, we cannot exclude the possibility that these features are artifacts resulting from the MALDI process. One potential approach to analyzing these unknown features in the future is with the Bruker timsTOF fleX instrument, which is equipped with a post-ionization laser, referred to as MALDI-2, that increases sensitivity

for challenging analytes, and trapped ion mobility spectrometry (TIMS) that enables high ion mobility resolution.

3.2.4. On-tissue MALDI-MS/MS to confirm abundant lipid annotations

Some of the more abundant lipid species were confirmed via on-tissue targeted MS/MS fragmentation in the negative ionization mode. Fragmentation spectra were assigned in **Figure 3.11** using the LIPID MAPS prediction tool for the fragmentation of phospholipids. Diagnostic fragments were used to confirm the lipid class and determine the specific *sn1/sn2* position of fatty acids. Thus, shown are the targeted fragmentation spectra of PE(18:0/20:4), PS(18:0/22:6), and PI(18:0/20:4), with diagnostic fragments of ethanolamine phosphate at *m/z* 140.01, loss of serine headgroup at *m/z* 747.50, and inositol phosphate dehydration ion at *m/z* 241.01 for the respective lipids.

Additionally, fragmentation revealed that some abundant lipid features were initially misidentified. Two specific *m/z* features were discovered to be in-source fragments of other abundant lipids, including the fragment of PI(18:0/20:4) at *m/z* 599.33, which had the characteristic peak of inositol phosphate, and the fragment of PC(16:0/18:1) at *m/z* 744.56, which had diagnostic fragments that included the intact choline headgroup.

Additionally, PA(18:1/16:0) could also be an in-source fragment, and this has been reported in the literature as a potential source of error in MALDI experiments (Vandergrift et al., 2023). Any headgroup loss due to in-source fragmentation would lead to the same corresponding spectra for PA and, thus, could be mistakenly identified because there are no unique diagnostic fragments for PA.

3.3 Discussion

In this work, we successfully established the spatial distribution of cholesterol and its precursors, 7-DHC and 7-DHD, in the WT and *Dhcr7*-KO mouse model of SLOS. It has been previously shown that 7-DHC-derived oxysterols, particularly DHCEO, cause the neurogenic defects observed in SLOS models (Tomita et al., 2022; Xu et al., 2012). While increased oxysterols have been reported previously in whole-brain homogenates, this work represents the *first* molecular imaging of oxysterols in developing mouse brains. We found that the oxysterols mostly co-localized with the images of *m/z* values that correspond to 7-DHC and 7-DHD, with the highest intensity observed in the corpus callosum, followed by the outer layer of the cortex and the ventricular/subventricular zone of the cerebral cortex. Because neurogenesis initiates in the ventricular regions, the images support the pathophysiological roles of the cholesterol precursors and the oxysterols in SLOS. The high level of sterols in the corpus callosum is also consistent with the commonly observed defects of the corpus callosum in the brains of SLOS patients (Lee, Conley, et al., 2013; F. D. Porter et al., 2011).

This work also assembled a collection of lipid CCS values (97 and 163 in the positive and negative modes, respectively) derived from MALDI and TWIM. Thus, this lipid CCS collection fills a gap in MALDI-derived CCS values since previous CCS values are primarily measured for ions formed from ESI. Significantly, although MALDI and ESI are fundamentally different ionization mechanisms, the lipid CCS values are consistent between the same ions formed from MALDI and ESI. This demonstrates that the widely available ESI-derived CCS library (Picache et al., 2019; Ross, Cho, & Xu, 2020; Z. Zhou et al., 2020; Zhou et al., 2017) can be used for metabolite identification when using MALDI.

Differentially expressed lipids in different brain regions between *Dhcr7*-KO and WT mouse brains could shed light on their contribution to SLOS pathophysiology in addition to sterols and oxysterols. For example, the decreased levels of ceramides in the corpus callosum could affect the myelination process because ceramides are the lipid precursor to sphingomyelin, a major lipid involved in myelination. White matter lesions have been observed in the brains of SLOS patients (Dang Do et al., 2018; Lee, Conley, et al., 2013), which could be attributed to myelination defects. Second, the increased level of PI(38:4) and decreased level of PIP(38:4) could have a profound impact on the neurogenesis process. Conversion of PI to PIP is mediated by phosphatidylinositol 3-kinase (PI3K), and the PI3K/AKT pathway is important for neurogenesis (Le Belle et al., 2011). Third, lysophospholipids were found to be increased in *Dhcr7*-KO brains. Lysophospholipids are important signaling molecules that mediate numerous physiological processes, such as brain growth, neuron arborization, and myelination, through their specific G-protein coupled receptors (Tan et al., 2020). Lastly, free fatty acids were generally higher in the *Dhcr7*-KO brains than in the WT. This is consistent with the higher level of lysophospholipids since both are presumably formed from phospholipase activities. Free fatty acids have been found to play important roles in neuroinflammation, learning, and memory (Joensuu et al., 2020). To summarize, the spatial lipidomic changes resulting from *Dhcr7*-KO could lead to new avenues of research to further understand the neurodevelopmental phenotype in SLOS.

3.4 Experimental Procedure

3.4.1. Chemicals

α-cyano-hydroxycinnamic acid (CHCA), 9-aminoacridine (9-AA), red phosphorus, and cholesterol were purchased from Sigma-Aldrich Inc. 2-methylbutane was purchased from

Thermo Fisher Scientific (Grand Island, New York). 7-dehydrocholesterol, 7-dehydrodesmosterol, and desmosterol were purchased from Avanti Polar Lipids. DHCEO, 4α-hydroxy-7-DHC, and 4β-hydroxy-7-DHC were prepared as described previously (Xu, Korade, et al., 2011; Xu, Liu, et al., 2011).

3.4.2. Animals

C57BL/6J and transgenic heterozygous mice with a null mutation for *Dhcr7* (Ex8) mice were purchased from Jackson Laboratories (Bar Harbor, Maine; catalog #007453). The University of Washington Institutional Animal Care and Use Committee approved all animal protocols. Mice were housed in an animal care facility with a 12-hour light and dark cycle and fed an *ad libitum* commercial rodent chow diet. Heterozygous *Dhcr7* (Ex8) mice were mated overnight, where the day after time-mating was designated as embryonic day 0.5 (E0.5). At birth, neonate litters were separated from their dams and euthanized on ice via decapitation. Neonatal brains were harvested under a dissection scope and flash frozen in pre-cooled 2-methylbutane, transferred to dry ice, and stored at -80ºC until further steps of matrix application and analysis.

3.4.3. Sample preparation for MALDI-MSI

The sample preparation workflow is outlined in **Figure 3.1**. Brain tissues were attached to the cryostat chuck with minimal OCT. Coronal tissue sections were cut at 16 μm thickness and thaw-mounted onto standard glass slides. WT and KO mouse brain sections were collected at various intervals along the anterior-posterior axis and paired on the same slide. Slides were stored at -80 ºC and placed in a vacuum desiccator to thaw and avoid condensation.

Slides were coated *via* sublimation with CHCA and 9-AA for positive and negative mode ionization, respectively (Caughlin et al., 2017). Briefly, 300 mg of the matrix was evenly

deposited on the bottom of the outer flask of the sublimation glassware (Chemglass Life Sciences), and a slide was affixed with tape to the bottom of the inner flask filled with an ice water slurry. The assembled glassware apparatus was heated in a sand bath and connected to a vacuum pump manifold. Sublimation was performed under the following conditions: 180ºC, 0.2 Torr pressure, and 60 minutes for CHCA, and 120ºC, 2 Torr pressure, and 10 minutes for 9-AA.

Slides were washed post-analysis with 100% methanol for 30 seconds. H&E staining was performed following a standard H&E procedure (Vector Laboratories) to correlate ion images with specific histological brain regions. High-resolution optical images were obtained with a scanner (Epson Perfection V850 Pro).

3.4.4. MALDI-IM-MS

MALDI-IM-MS was performed on a Waters SYNAPT XS traveling wave IM (TWIM)-QTOF mass spectrometer equipped with a 1k Hz Nd:YAG laser in both positive and negative ionization modes. Data was acquired over a mass range of 50 to 1200 *m/z*. TWIM separation was performed with a gas flow rate of 90 mL/min, a wave velocity of 500 m/s, and a wave height of 40 V. Images were acquired at 30 or 50 µm spatial resolution (step size). High-Definition Imaging (HDI) software and EZ-Info (Waters) were used for data processing, visualization, and statistical analysis. TWIM-derived CCS values were calibrated manually with a series of phosphatidylcholine (PC) and phosphatidylethanolamine (PE) lipid standards using an in-house Python script, as described previously (Hines et al., 2016; Ross et al., 2019). Red phosphorus reference spots were used for lock-mass correction. Features were normalized to total ion current (TIC) at each pixel. Lipid identifications were made by *m/z* and CCS matching using various databases, including LIPID MAPS, HMDB, our own in-house CCS database, CCSbase (https://CCSbase.net) (Ross, Cho, & Xu, 2020), and an automated lipidomics data processing

Python package, *LiPydomics* (https://github.com/dylanhross/lipydomics) (Ross, Cho, Zhang, et al., 2020). Lipid identifications are reported at the level of fatty acyl sum composition in **Table S3.1**. On-tissue targeted MS/MS fragmentation of high-abundance lipids was carried out by ramping the collision energy in the transfer region from 25-40 eV.

Data shown in this work are from two biological replicates per ionization mode (replicate data shown in **Figure 3.3**, **Figure 3.9**, and **Figure 3.10**). Other serial sections served as technical replicates and are consistent with the results (data not shown).

3.4.5. Data availability

Raw MALDI-IM-MS data is available at MassIVE under MSV000092638 (doi:10.25345/C5125QM05).

3.5 Conclusion

In this work, we used MALDI-IM-MSI to map out the brain sterolomic and lipidomic changes caused by *Dhcr7*-KO in a SLOS mouse model compared to wild-type controls. Although cholesterol is a notoriously difficult molecule to ionize, we were able to achieve mapping of the distribution of cholesterol, sterol precursors, and oxysterol metabolites within WT and *Dhcr7*-KO brains in positive ionization mode, which confirmed the biochemical hallmark of SLOS. In addition, we determined several classes of lipids on brain tissue in positive and negative ionization modes that were altered between WT and *Dhcr7*-KO via multivariate statistical analysis and confirmed their identities via *m/z* and CCS. On-tissue fragmentation further confirmed the identities and fatty acid composition of some abundant lipids. The biological implications of some of these lipidomic changes in certain lipid classes, such as lysophospholipids and ceramides, were discussed in the context of SLOS neurobiology. Finally,

we compiled a library of MALDI-derived, TWIM-measured CCS values of mouse brain lipids detected in this study.

Figures

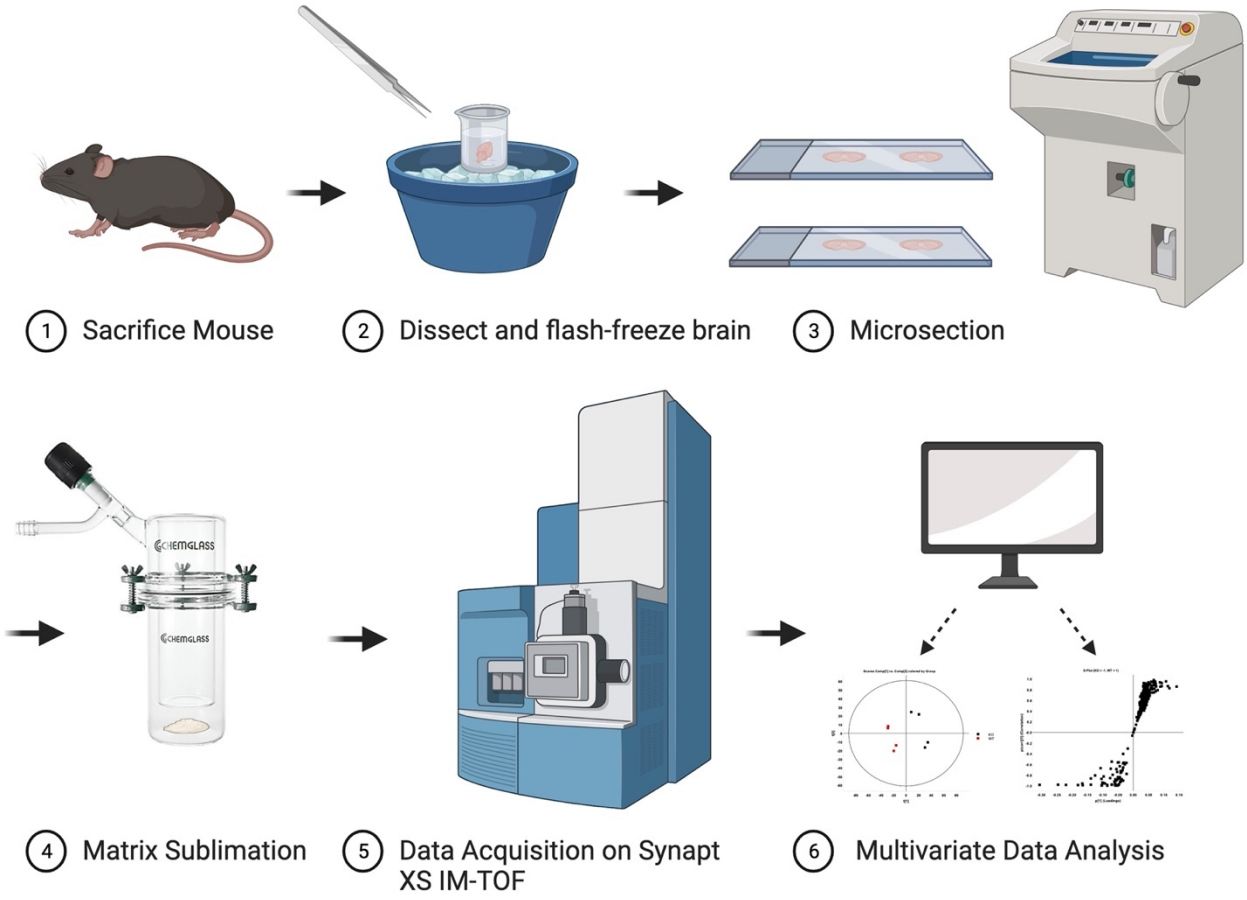

Figure 3.1 Diagram of the MALDI-IM-MS imaging workflow, including steps for sample preparation (brain harvested from mouse, tissue sectioning), matrix application (coating via sublimation), and data acquisition and analysis. Created with BioRender.com.

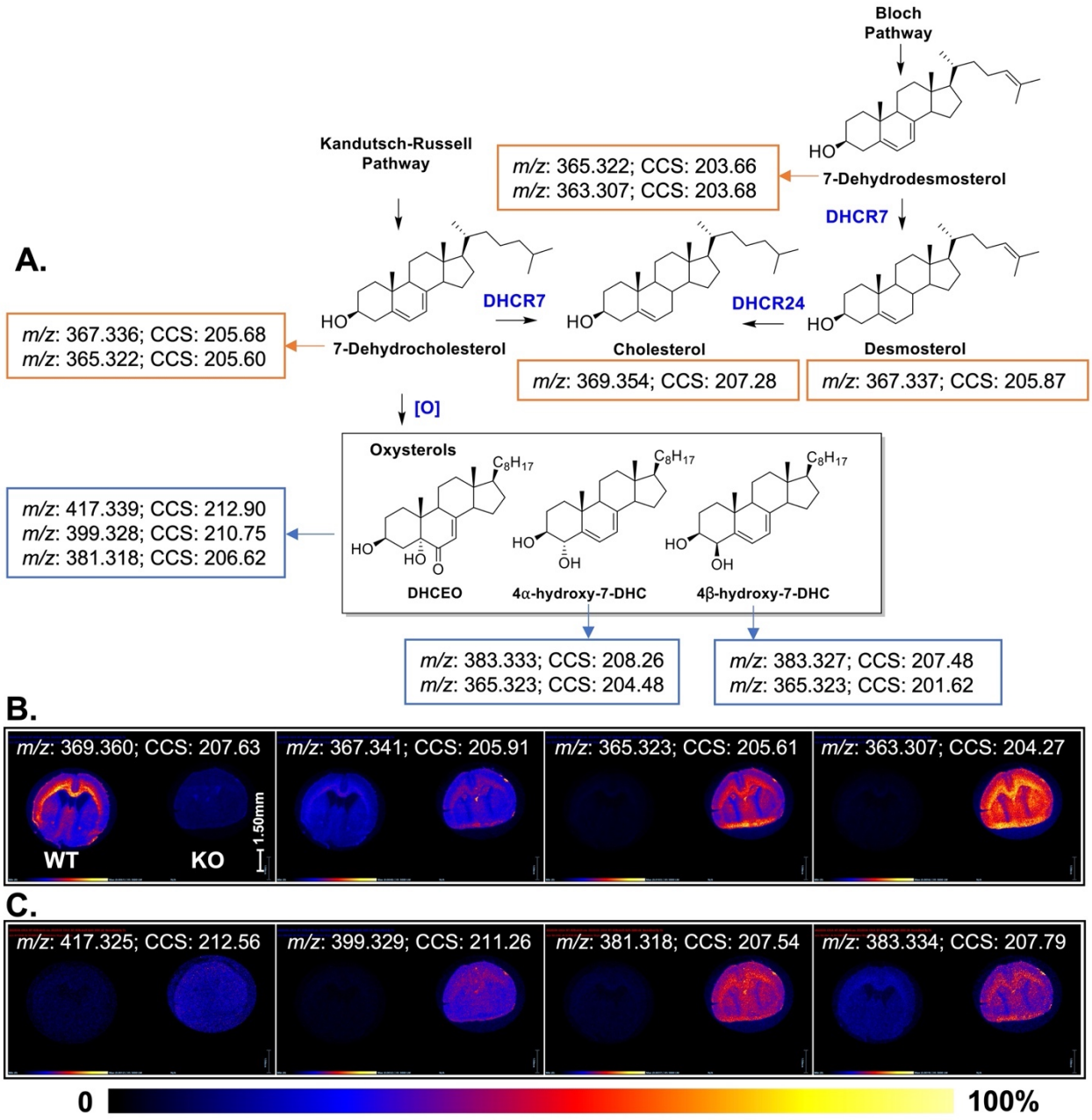

Figure 3.2 A. Last steps of cholesterol biosynthesis pathway with associated enzymes. Boxes contain exact mass and TWIM-derived CCS measurements from MALDI of sterol and oxysterol standards. **B.** Ion images of cholesterol and sterol precursors in WT (left) and *Dhcr7*-KO (right) mouse brain tissue. **C.** Ion images of oxysterol metabolites in WT (left) and *Dhcr7*-KO (right) mouse brain tissues. Intensities are normalized to TIC and represented according to the heat map color gradient.

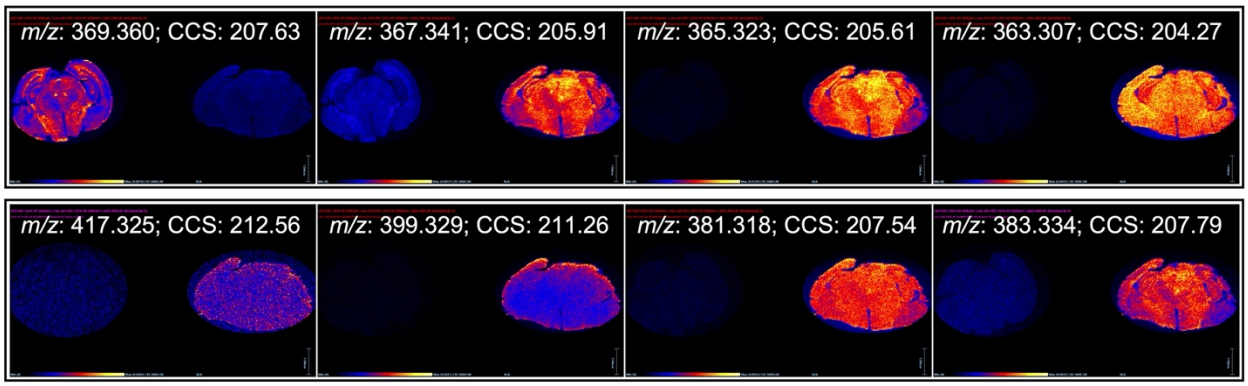

Figure 3.3 Biological replicate data for sterol and oxysterol features from **Figure 3.2** (n = 2 animals per genotype and ionization mode).

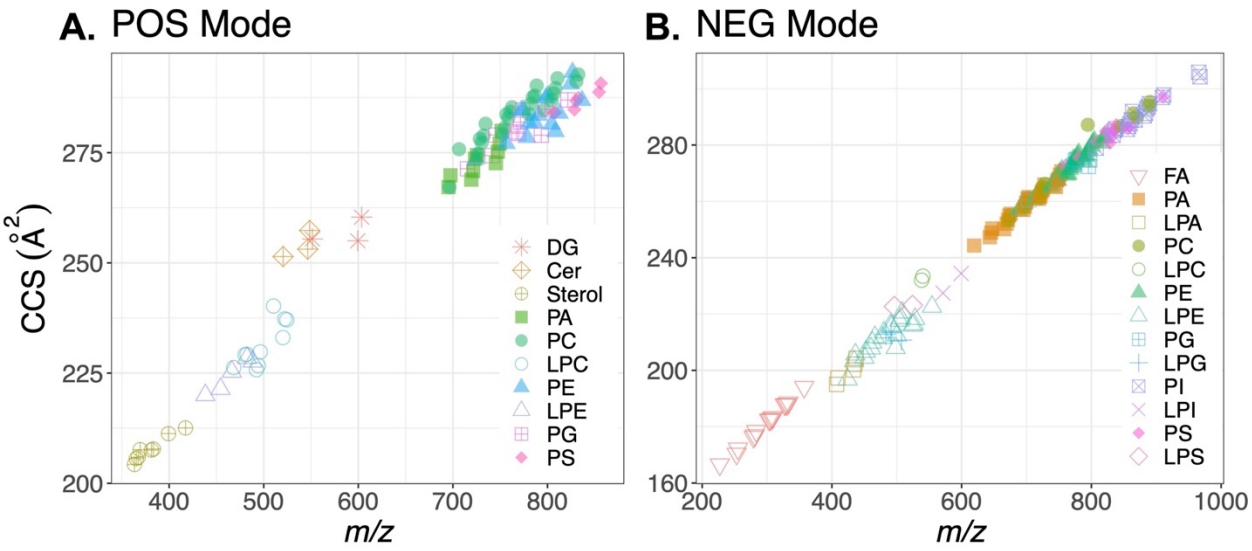

Figure 3.4 Collision cross section (CCS)-*m/z* plot of lipids identified in **A.** positive and **B.** negative ionization modes in MALDI-IM-MS analysis of mouse brains at postnatal day 0.

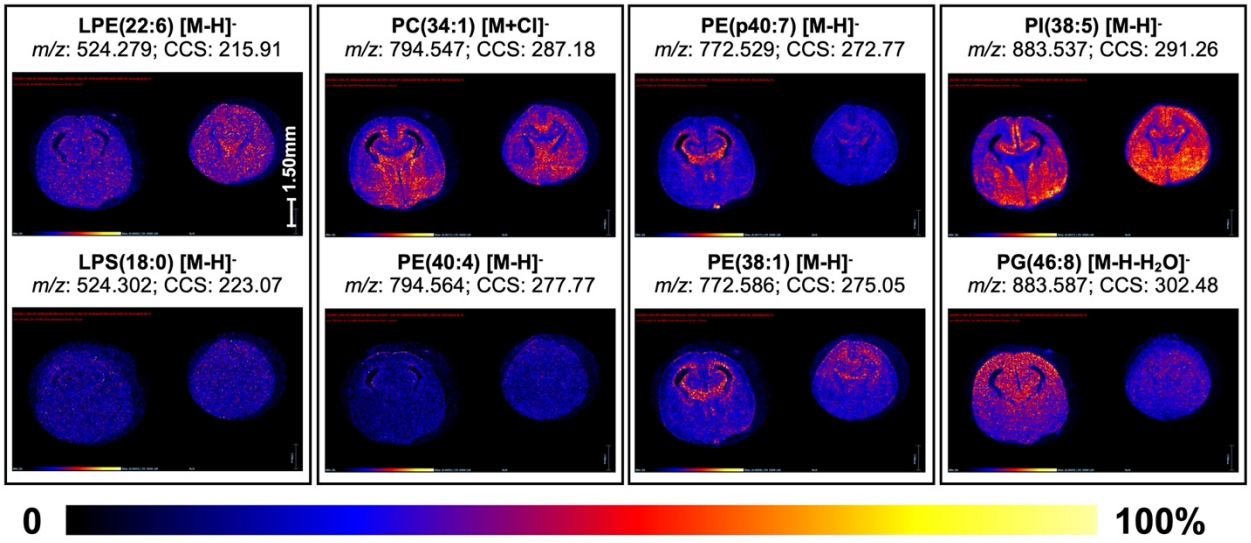

Figure 3.5 Ion images of selected isobaric lipid pairs with different CCS values. Intensities are normalized to TIC and represented according to the heat map color gradient.

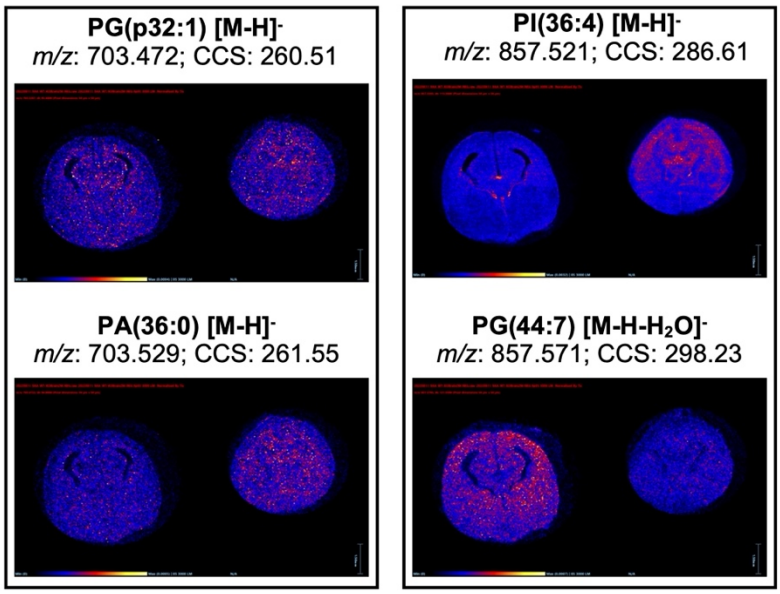

Figure 3.6 Other isobaric lipid pairs with different CCS values.

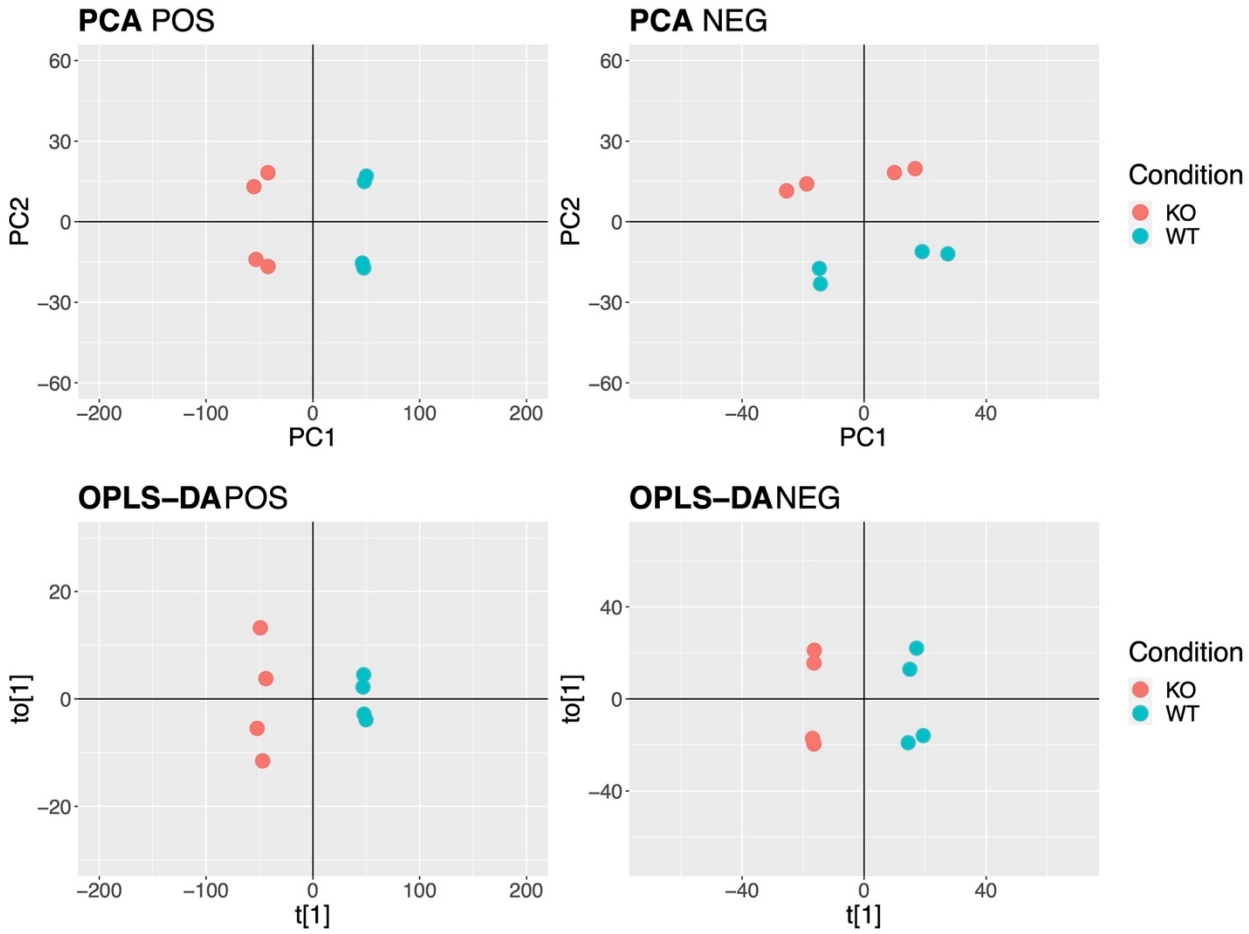

Figure 3.7 Multivariate statistical analysis of WT and *Dhcr7*-KO mouse brain tissues. Unsupervised PCA plots and supervised OPLS-DA plots for one biological replicate in negative and positive ionization modes.

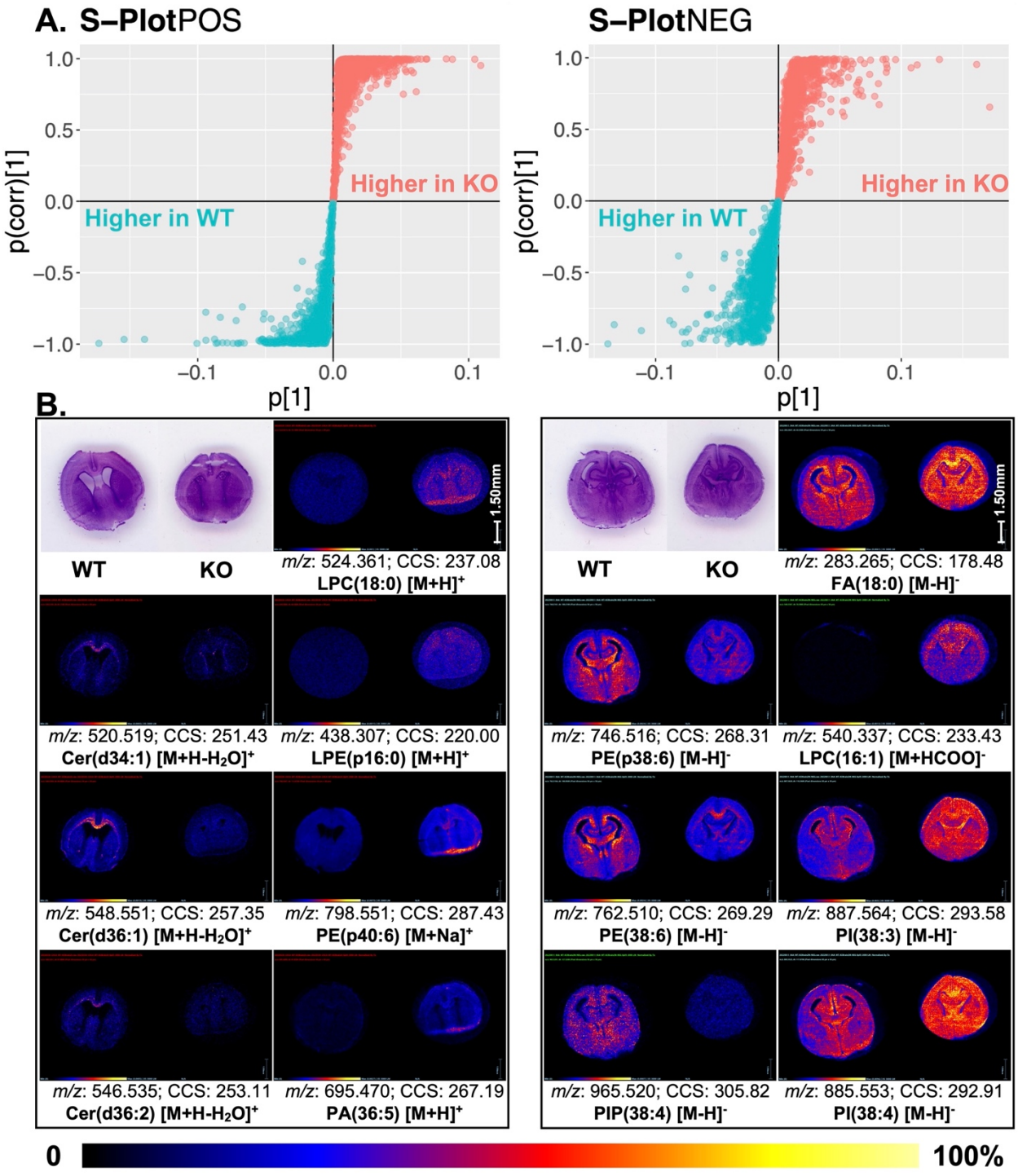

Figure 3.8 A. S-plots from multivariate statistical analysis of a pair of WT and *Dhcr7*-KO mouse brain tissues in positive and negative ionization modes. **B.** Ion images of lipid features that are higher in WT or higher in *Dhcr7*-KO are shown below each respective S-plot. Intensities are normalized to TIC and represented according to the heat map color gradient.

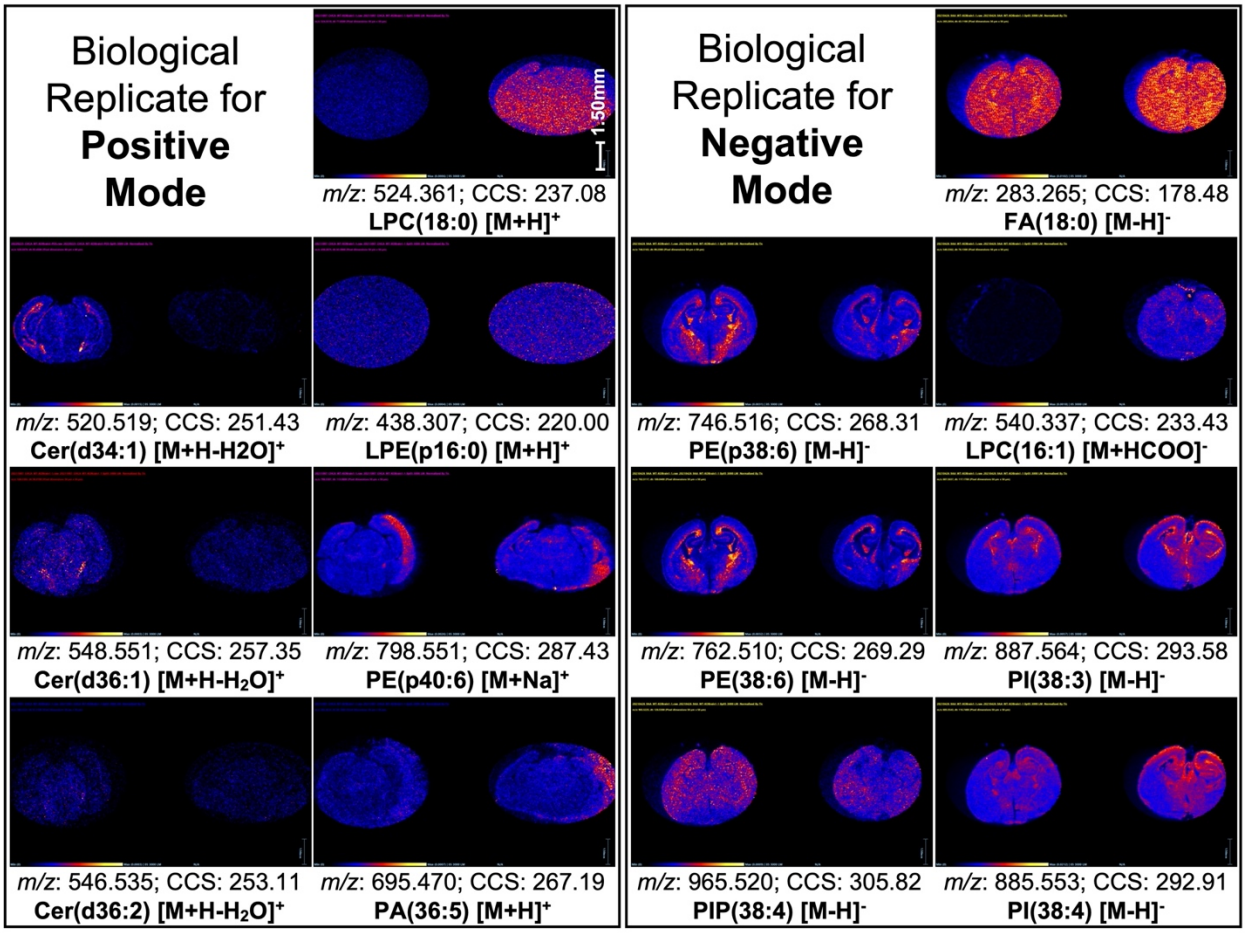

Figure 3.9 Biological replicate data for significantly altered lipid features from **Figure 3.8** (n = 2 animals per genotype and ionization mode).

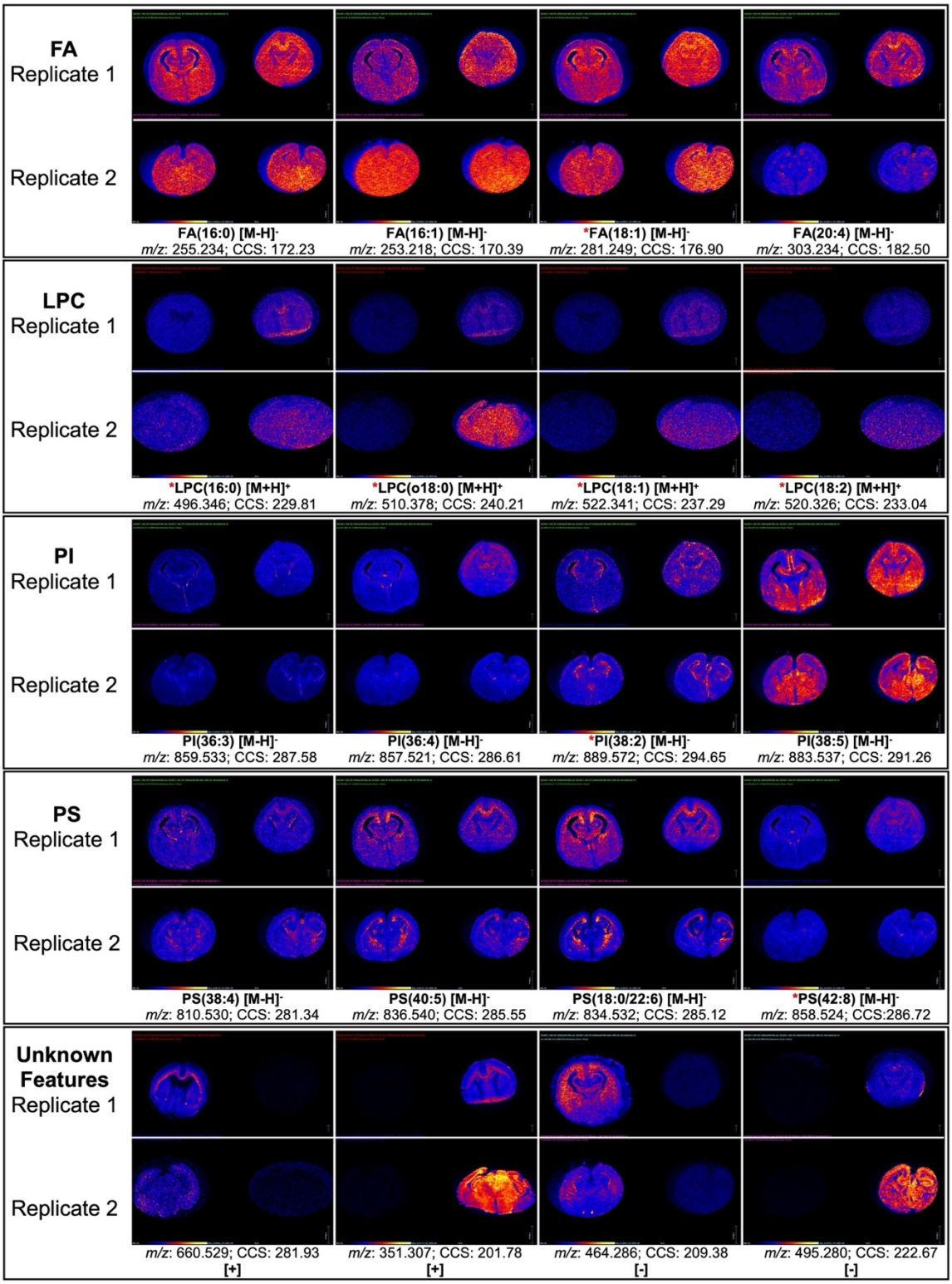

Figure 3.10 Ion images of other lipid species in two biological replicates. Asterisk (*) denotes features with a significant p(corr) value (absolute value ≥ 0.9).

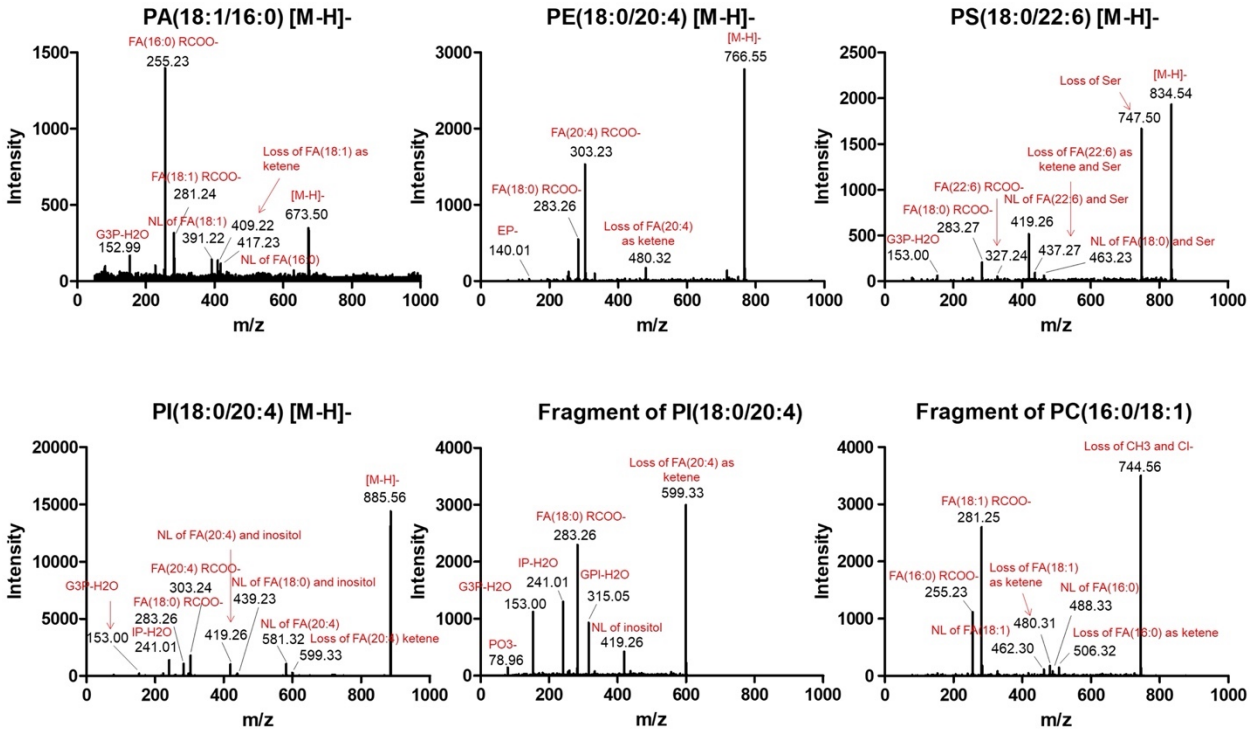

Figure 3.11 Targeted fragmentation spectra of lipid features found on-tissue via MALDI-MS/MS. Diagnostic fragments were used to confirm lipid class assignment and determine sn1/sn2 fatty acyl chain compositions.

Tables

Excel spreadsheet tables are accessible as Supporting Info in the preprint:

> Amy Li and Libin Xu, MALDI-IM-MS Imaging of Brain Sterols and Lipids in a Mouse Model of Smith-Lemli-Opitz Syndrome, *bioRxiv*, (**2023**). doi:10.1101/2023.10.02.560415.

Table S3.1 Table of lipid identifications and measured CCS values compared to reference values (% error).

Table S3.2 Table of isobaric lipid pairs with different CCS values.

Chapter 4 Temporal Transcriptomic Changes in SLOS Neurodevelopment

Portions of this chapter have been deposited as a preprint at bioRxiv:

> Amy Li, Hideaki Tomita, and Libin Xu, Temporal gene expression changes and affected pathways in neurodevelopment of a mouse model of Smith-Lemli-Opitz syndrome, *bioRxiv*, (**2023**). doi:10.1101/2023.11.21.568116.

4.1 Introduction

Smith-Lemli-Opitz syndrome (SLOS, OMIM #270400) is caused by genetic mutations in the *DHCR7* gene (Fitzky et al., 1998; P. E. Jira et al., 2003; Tint et al., 1994; Wassif et al., 1998; Yu et al., 2000), which encodes the terminal enzyme of cholesterol biosynthesis, 7-dehydrocholesterol reductase (DHCR7, EC 1.3.1.21), leading to decreased levels of cholesterol and increased levels of the cholesterol precursor, 7-dehydrocholesterol (7-DHC), other sterol intermediates, and oxysterol metabolites (F. D. Porter et al., 2011; Thurm et al., 2016; Tint et al., 1995). Clinically, the disorder manifests a wide variety of phenotypes, including multiple congenital malformations (structural abnormalities and functional defects across several organ systems), developmental delay, and cognitive impairment (Kelley et al., 2000). Specifically in the CNS, anatomical abnormalities have been observed in SLOS patients, ranging from microcephaly to enlarged ventricles and hypoplasia of the corpus callosum, and in the most severe cases, holoprosencephaly (Dang Do et al., 2018; Lee, Conley, et al., 2013; Marion et al., 1987; F. D. Porter et al., 2011).

Development of the CNS is a carefully orchestrated and regulated process involving the interplay of many different signaling pathways. In the CNS, cholesterol plays an essential role as a precursor to neurosteroids and steroid hormones, a major component of plasma membranes, myelin, and lipid rafts, and an important modulator of developmental signaling pathways, such as the Sonic hedgehog pathway (Koudinov et al., 2001; Mauch et al., 2001; J. A. Porter et al.,

1996; Saher et al., 2005). Thus, disruption of cholesterol synthesis profoundly impacts many cellular processes in brain development, given the numerous biological functions of cholesterol. In addition, the cholesterol pool in the brain is especially unique due to the blood-brain barrier preventing cholesterol uptake from the circulation (Dietschy et al., 2004). This means that cholesterol metabolism must be tightly regulated in a spatiotemporal manner during neurodevelopment to supply the high metabolic needs of cells during neurogenesis, as cells proliferate, migrate, differentiate, and undergo programmed cell death (Dietschy et al., 2004; Funfschilling et al., 2012). While there is limited maternal-fetal transfer during early development in mice, *de novo* cholesterol synthesis becomes critical in the CNS after the formation of the blood-brain barrier around E10-11, while cortical neurogenesis begins around E12.5 and peaks around E15.5.

The development of genetically engineered mouse models of SLOS has made it possible to study the molecular mechanisms underlying the disorder at embryonic stages. In this study, we utilize a commercially available SLOS mouse model, *Dhcr7*-KO (Ex8), in which the exon VIII coding region of *Dhcr7* has been deleted, leading to a truncated gene product (Fitzky et al., 2001). The mouse model replicates the known biochemical defect of cholesterol synthesis (Tomita et al., 2022) and exhibits developmental abnormalities in the lung, cleft palate, and bladder (Fitzky et al., 2001). Homozygous pups die on the first day of birth due to an uncoordinated suck and failure to feed.

Transcriptomic studies of SLOS models have been previously reported in the literature (Francis et al., 2016; Tomita et al., 2022; Waage-Baudet et al., 2005). One of the first transcriptomic studies of SLOS mice using Affymetrix microarray analysis reports gene expression profiling on the hindbrains of gestational day 14 (E14) SLOS mice (Waage-Baudet et

al., 2005). Hierarchical clustering of the differentially expressed genes identified alterations in genes involved in cholesterol homeostasis, cell cycle control and apoptosis, neurodifferentiation, embryogenesis, and, of particular interest, axon guidance. Dysregulated axon guidance was believed to be partly responsible for the abnormal hippocampal development previously reported in these mice (Waage-Baudet et al., 2003). In another study using a human-derived induced pluripotent stem cell (iPSC) model of SLOS that exhibited aberrant neural differentiation, Francis et al. determined that several transcriptional networks related to neural differentiation, cadherin-associated signaling, and kinase signaling were affected when comparing control iPSCs to SLOS iPSCs. In addition, they found overall downregulation of Wnt/β-catenin signaling (*CAV1, CDH1, SNAI2*), suggesting a role of defective Wnt signaling in the aberrant iPSC differentiation phenotype in SLOS (Francis et al., 2016).

In a recent study from our lab, we found that *Dhcr7*-KO leads to a premature neurogenesis phenotype (with decreased proliferation and increased differentiation) of neural precursors in both a SLOS mouse model and in SLOS patient-derived neural progenitor cells (NPCs) and eventual thinning of cortical layers in embryonic mouse brains (Tomita et al., 2022). This mechanism was found to be mediated by glucocorticoid receptors and the neurotrophin kinase, TrkB. RNA sequencing analysis of human SLOS NPCs revealed gene expression changes related to neural precursor proliferation and differentiation, including those involved in MAPK and Ras signaling. While many transcriptomics experiments have been performed to investigate the pathophysiological mechanism of SLOS, no study has examined the temporal changes in gene expression and biological pathways throughout the embryonic developmental stages.

In this chapter, we discuss the results of an RNA sequencing analysis of whole brains (Wang et al., 2009) in a well-established SLOS mouse model, *Dhcr7*-KO mice, at E12.5, E14.5, E16.5, and PND0 compared to matching wild-type (WT) mice. Differentially expressed genes and significantly affected signaling pathways and biological processes were identified at each time point. Meta-analysis of all four time points highlighted shared and unique biological pathways at distinct developmental stages.

4.2 Results

4.2.1. Differential Expression Analysis

RNA sequencing (RNAseq) of whole mouse brains was performed, and gene expression profiles were compared between WT and *Dhcr7*-KO mice at three embryonic time points (E12.5, E14.5, E16.5) and one postnatal time point (PND0). RNAseq steps are outlined in **Figure 4.1**, including brain dissections, RNA extraction and sequencing, and data analysis.

When considering all the WT and KO samples together in one principal component analysis (PCA) bi-plot (**Figure 4.2A)**, there is separation and clustering of the four groups according to time points, indicating that there are differences in the transcriptome at each time point that make each cluster distinct from the others. The PCA bi-plots constructed for each individual time point (**Figure 4.2B**) more clearly demonstrate the separation between WT and KO samples.

To examine gene expression differences between the WT and KO conditions at the various time points, we performed differential expression analysis using DESeq2 in R. The number of differentially expressed genes (DEGs) for each time point, using an adjusted p-value (or false discovery rate, FDR) threshold of 0.05, are summarized in **Table 4.4**, including the number of total measured genes used as a reference background for pathway analysis. In

summary, E12.5 had 647 differentially expressed genes (213 up-regulated in *Dhcr7*-KO compared to control, 434 down-regulated), E14.5 had 279 genes (129 up-regulated, 150 down-regulated), E16.5 had 645 genes (391 up-regulated, 254 down-regulated), and PND0 had 919 genes (391 up-regulated, 528 down-regulated). In **Figure 4.3**, significant DEGs (using thresholds: adjusted p-value (FDR) ≤ 0.05 and absolute fold-change ≥ 1.2) are visually represented on volcano plots displaying the magnitude of change on the y-axis and statistical significance on the x-axis. The complete list of DEGs is available in **Table S4.1**. The low number of measured genes for E14.5 resulted from the independent filtering step in DESeq2, which removes features with very low read counts that have low power to be detected as significant due to high dispersion.

Interestingly, most DEGs were not overlapping between time points, as seen in **Figure 4.4**, suggesting that there are differences in the genes and pathways being affected at specific times throughout development. Only nine DEGs were found to be shared between all four groups. Three that were down-regulated (*Abca1, Dhcr7, Srebf1*) and six up-regulated (*Aacs, Fdft1, Hmgcs1, Nsdhl, Sqle, Stmn4*). Besides *Stmn4*, the rest of the genes are all directly involved in different aspects of sterol metabolism, such as efflux transport (*Abca1*), transcriptional regulation (*Srebf1*), and various enzymes along the synthetic pathway. As expected in this *Dhcr7*-KO mouse model, the gene encoding for *Dhcr7* was the most down-regulated gene transcript, with the largest fold-changes across all four time points and lowest p-values. However, the other observed changes, such as up-regulation of key enzymes involved in cholesterol biosynthesis, are likely compensatory mechanisms that are transcriptionally regulated by the low cellular cholesterol levels in *Dhcr7*-KO mice.

4.2.2. Pathway Analysis and Gene Ontology (GO) Term Enrichment

For genes included in pathway analysis, we used a significance threshold of an adjusted p-value (FDR) ≤ 0.05. Pathway analysis is used to identify which pathways are over-represented in a given set of genes beyond pure random chance. iPathwayGuide uses their proprietary "Impact Analysis" that factors in two probabilities, pORA (over-representation) and pAcc (perturbation), to compute statistical significance and is modeled after the Kyoto Encyclopedia of Genes and Genomes (KEGG) pathways (Donato et al., 2013; Draghici et al., 2007; Kanehisa & Goto, 2000). It should be noted that we did not apply p-value adjustment for the pathway analysis results. Many pathways were significantly affected at individual time points. The top 10 KEGG pathways significantly affected at each time point are shown in **Figure 4.5**, and additional significantly altered pathways are available in **Table S4.2**. Pathway results are visualized with bubble plots, which are ranked by p-value. The horizontal position on the plot designates the ratio of differentially expressed genes to the total number of genes associated with the specific pathway, while the size of the bubble designates the number of differentially expressed genes, and the color designates the p-value. Interestingly, some of the top results in the earliest time point (E12.5) include important signaling pathways for embryonic development (Hippo, Wnt, and TGF-β). In contrast, later time points include pathways related to neurotransmission (synaptic vesicle cycle and different types of synapses, including cholinergic, glutamatergic, and GABAergic synapses).

We also performed a GO enrichment analysis to identify which GO terms for biological processes are significantly over-represented in the given set of genes (Ashburner et al., 2000; Gene Ontology et al., 2023). The top 10 GO biological process terms enriched at each time point are shown in **Figure 4.6**. Like pathway analysis, we found many top terms related to sterol

synthesis, development, and synaptic signaling. To verify these pathway analysis results, we used another online tool, the Database for Annotation, Visualization, and Integrated Discovery (DAVID), for comparison (Dennis et al., 2003; Sherman et al., 2022). The DAVID pathway analysis and GO enrichment analysis results are shown in **Figure 4.7** and **Figure 4.8** and were consistent with iPathwayGuide. Though GO terms tend to have much larger gene sets than KEGG pathways, the significantly affected biological processes are in line with the significantly affected pathways revealed by iPathwayGuide. The complete list of significantly enriched GO terms for biological processes is available in **Table S4.3**.

4.2.3. Pathway Meta-Analysis of All Time Points

The meta-analysis feature in iPathwayGuide enables cross-comparison of the four time points, as shown via the UpSet plot in **Figure 4.9**. *Steroid biosynthesis* (mmu:00100) is the only pathway significantly affected at all time points, with a p-value significance threshold set at 0.05. This is a similarly expected result as the shared DEGs. **Figure 4.10** shows the genes associated with the *steroid biosynthesis pathway* and their log fold-changes for each time point. This list of genes includes transcripts different from the nine shared DEGs (from **Figure 4.4**), including *Lss, Msmo1, Cyp51, Sc5d, Dhcr24, and Tm7sf2.* In this case, *Dhcr7* is the only down-regulated gene, while all the other steroid synthesis-related genes are up-regulated.

In **Figure 4.9**, we have highlighted pathways that are commonly affected at two or more time points. For example, the *cell adhesion molecules pathway* (mmu:04515) is the only other pathway shared between all embryonic time points, E12.5-E16.5 (**Figure 4.11**). *L1cam* is the only gene consistently up-regulated at those three time points. The *ribosome pathway* (mmu:03010) was significantly affected in E14.5, E16.5, and PND0 groups, and the associated genes are broken down for each time point in **Figure 4.12**. Many of the genes in this pathway

encode ribosomal proteins either in the small or large subunit. However, there is little overlap between the ribosomal DEGs at these three time points. It is also interesting to note that while all the DEGs in this pathway are down-regulated for E14.5 and E16.5 time points, all the DEGs except for one are up-regulated at PND0. This result could indicate a defect in translation at the ribosome level and in protein synthesis, while the switch in the direction of fold-changes highlights the temporal aspect of regulation.

Both *cholinergic* (mmu:04725) and *GABAergic synapse pathways* (mmu:04727) were significantly affected at the later E16.5 and PND0 time points (**Figure 4.13**). For both, most genes are up-regulated at E16.5 and down-regulated at PND0, although the DEGs specific to the pathway differ between the time points. Gene expression changes in neurotransmitter signaling pathways could suggest defects in neurotransmission in SLOS, which will be discussed in the next section. Another related pathway, the *glutamatergic synapse* (mmu:04724), was shared between E12.5 and E16.5 time points (**Figure 4.14**), along with the *axon guidance* (mmu:04360) and *neuroactive ligand-receptor interaction pathways* (mmu:04080). Similar to the *cholinergic* and *GABAergic synapse pathways*, DEGs were found to be mainly up-regulated at the E16.5 time point. GABA is the primary inhibitory neurotransmitter, and glutamate is the main excitatory neurotransmitter in the mammalian CNS, suggesting that both inhibitory and excitatory neurotransmission were affected.

4.2.4. Unique Pathways for Individual Time Points

In addition to the pathways commonly enriched at multiple time points, some are uniquely enriched at individual time points. We expect to observe significant genes and pathways specific to the different stages of development. Thus, it makes sense that amongst earlier time points, there were pathways more closely related to neurogenesis and early

embryonic development of the CNS. In contrast, later time points had a greater emphasis on neuronal maturation and synaptic signaling.

E12.5

Amongst the pathways significantly affected at E12.5 (**Figure 4.5**), three are related to embryogenesis, including *Hippo*, *Wnt*, and *TGF-β* pathways. All three are well-known, evolutionarily conserved signaling pathways crucial for mammalian embryonic development. DEGs for these three pathways are shown in an interaction network in **Figure 4.15**, where lines denote different types of interactions between genes and colors represent the direction of fold-change. There is some overlap between the genes within these three related pathways. Most of the DEGs are down-regulated, which could indicate that inhibited signaling within these pathways is underlying some of the structural and functional CNS abnormalities present in the SLOS phenotype.

E14.5

For E14.5 (mid-neurogenesis), two related pathways, *cell cycle* (mmu:04110) and *cellular senescence* (mmu:04218), were found to be among those significantly affected. Both pathways are related to cell cycle control, an important element of embryonic development and neuronal differentiation. Cyclin-dependent kinases (CDKs) are key regulatory enzymes in both pathways (Brantley & Di Talia, 2021), and *CDK1* (the major CDK enzyme that controls cell cycle) and *CDK4* gene transcripts were both found to be down-regulated, as seen by the interaction network in **Figure 4.15**. This finding is interesting, considering the critical role of apoptosis in neurogenesis.

E16.5

E16.5 had the largest number of unique pathways significantly affected among all the time points, with 31 pathways with a p-value ≤ 0.05. Among these, the *synaptic vesicle cycle* (mmu:04721) and two pathways related to *cAMP/AMPK signaling* (mmu:04024 and mmu:04152) were particularly interesting (**Figure 4.15**). Synaptic vesicles mediate the release of neurotransmitters into the synaptic cleft between synapses, and this affected pathway is related to the other synapse-associated pathways shared between several time points. Similar to those pathways, the DEGs for synaptic vesicle cycle were mostly up-regulated at E16.5. For cAMP/AMPK signaling pathways, there appears to be a link between these two pathways and their role in cellular homeostasis (Aslam & Ladilov, 2022). While most DEGs involved were up-regulated, dysregulation of cAMP/AMPK signaling could likely affect downstream physiological processes, including metabolism (various biosynthetic pathways), cell fate, and gene transcription.

PND0

For PND0, we found many of the DEGs in significantly affected pathways to be down-regulated. In general, at this time point, there were more down-regulated genes than up-regulated ones, as seen in the asymmetrical volcano plot of DEGs (**Figure 4.3**). Among the significantly affected pathways, *growth hormone, secretion, and action* (mmu:04935) and *phospholipase D signaling pathways* (mmu:04072) were of particular interest, as seen in **Figure 4.15**.

4.3 Discussion

Individuals with SLOS show a wide range of severity in phenotype across the many affected organ systems (Kelley et al., 2000), and this applies to the neurological phenotype seen

in the CNS. Neurological defects manifest as structural abnormalities (Dang Do et al., 2018; Lee, Conley, et al., 2013; Marion et al., 1987; F. D. Porter et al., 2011), developmental delay, intellectual disability, and behavioral problems, as well as frequent co-occurrence of autism spectrum disorder (ASD) (Sikora et al., 2006; Tierney et al., 2001).

Cortical neurogenesis occurs over the span of several days, from approximately E11 to E17 (Chen et al., 2017). *De novo* cholesterol synthesis turns on around E10-E11 to supply the large cholesterol needs of neurogenesis (Sisecioglu et al., 2015). The time points within our study span these neurogenesis stages. We and others have reported that loss of *DHCR7* leads to decreased proliferation and premature neurogenesis in both human and mouse NPCs (Francis et al., 2016; Tomita et al., 2022). Francis et al. found that defective Wnt signaling may be responsible for such a phenotype, while our work suggested that activation of glucocorticoid receptor (GR) by an oxysterol metabolite may be the critical signaling pathway. However, these two findings are not mutually exclusive because activation of GR has been found to inhibit Wnt/β-catenin signaling (Olkku & Mahonen, 2009; H. Zhou et al., 2020). Wnt signaling is critical for basic developmental processes such as cell-fate specification, progenitor proliferation, and cell division (Teo & Kahn, 2010). At E12.5, *Wnt9b* (large fold-change), *Wnt4*, and *Wnt5b* are all down-regulated, as well as Wnt receptors, low-density lipoprotein receptor-related protein 5 (*Lrp5*) and Frizzled class receptor (*Frz7* and *Frz2*). These transcriptomics results support the important role of Wnt signaling in the decreased proliferation and increased neurogenesis phenotype of SLOS NPCs.

Hippo and *TGF-β signaling pathways* are the other two significantly affected pathways at E12.5 that are critical for embryonic development. The Hippo signaling pathway controls organ size in embryonic development, which could be related to the commonly observed microcephaly

phenotype in SLOS (Kelley et al., 2000). The signaling cascade consists of MST1 and MST2 kinases and their cofactors. In response to high cell density, activation of the pathway leads to cell apoptosis that prevents organ size overgrowth. At low cell density, when the pathway is inactivated, there are transcriptional factors that promote cell growth and proliferation. The TGF-β signaling pathway is involved in many different cellular functions, including proliferation, apoptosis, differentiation, and migration that are regulated by TGF-β family members. Most of the genes in Hippo and TGF-β signaling pathways are down-regulated, consistent with the decreased proliferation of *Dhcr7*-KO NPCs reported previously (Tomita et al., 2022).

E14.5 is in the middle of cortical neurogenesis as NPCs differentiate into neurons that migrate to the outer layers of the neocortex while a proliferating pool of NPCs is also maintained (Dehay et al., 2007; Molyneaux et al., 2007). Programmed cell death, or apoptosis, plays a critical role in regulating neuronal precursors and pruning inefficient synapses (Chen et al., 2017). Thus, it is not surprising to observe that cell cycle and cellular senescence were among the most significantly affected pathways at this time point.

It is important to note that GABAergic synapse, glutamatergic synapse, and cholinergic synapse pathways are significantly affected at later time points. Although previous work used mouse cortical precursors to demonstrate premature neurogenesis of excitatory neurons (Tomita et al., 2022), the current results indicate that the formation of all types of neurons may be affected similarly by the loss of *Dhcr7* function. Indeed, an impaired response of neurons to glutamate (Wassif et al., 2001) and aberrant development of the serotonergic system (Waage-Baudet et al., 2003) have been reported previously.

The switch in fold-changes of DEGs between E16.5 and PND0 time points, seen in the ribosome, cholinergic synapse, and GABAergic synapse pathways, made for an interesting set of observations. The biological importance of this flip between embryonic and postnatal time points should be further investigated. For example, in the GABAergic synapse pathway, the switch between up-regulated DEGs at E16.5 to down-regulated DEGs at PND0 could be related to the postnatal GABA shift, which is the developmental switch in GABAergic response (from excitatory-to-inhibitory) that occurs before and after birth (Ben-Ari, 2014; Peerboom & Wierenga, 2021).

At E16.5, the *axon guidance pathway* was found to be significantly upregulated. This is consistent with previous work by Jiang et al., which showed increased axon and dendrite formation in *Dhcr7*-KO mouse hippocampal neurons relative to WT (Jiang et al., 2010).

Ribosome pathway was found to be significantly affected at E14.5, E16.5, and PND0, but mostly downregulated at E14.5 and E16.5 and upregulated at PND0. This is a novel pathway that has not been indicated in previous studies. A recent paper showed that reduced cholesterol levels block the proliferation of erythroid precursors by inhibiting ribosome biogenesis (Lu et al., 2022). Although neural precursors are a different cell type than erythroid precursors, a similar mechanism could likely be in play for regulating the proliferation and differentiation of neural precursors. The role of cholesterol in regulating ribosome biogenesis in the brain and the significance of this pathway in neurodevelopment are worthy of further investigation in future studies.

Because SLOS patients are known to display autistic behavior, we examined whether the DEGs observed in *Dhcr7*-KO mouse brains contain known genes involved in autism by comparing them with the SFARI autism gene database. Indeed, we found 69, 39, 75, and 114

autism-related genes at E12.5, E14.5, E16.5, and PND0, respectively (**Figure 4.16**). Among these genes, only *DHCR7* was shared by all time points. Genes shared by three groups include *FAT1*, *CACNA1B*, *KCNQ2*, *KCTD13*, *HERC2*, *STXBP1*, *LDLR*, and *TSPAN7*. Additional genes shared by at least two time points are shown in the table in **Figure 4.16**. Enrichment analysis with DAVID for KEGG pathways (**Table 4.5**) highlighted several interesting pathways, including some of the synapse-related pathways discussed earlier, that could be relevant to the autistic behavior phenotype found in SLOS.

4.4 Experimental Procedure

4.4.1. Chemicals

2-methylbutane was purchased from Thermo Fisher Scientific (Grand Island, New York). RNeasy Lipid Tissue Mini Kit was purchased from Qiagen (Germantown, Maryland).

4.4.2. Animals

Animal studies were performed in accordance with the NIH *Guide for the Care and Use of Laboratory Animals* and approved by the University of Washington Institutional Animal Care and Use Committee. C57BL/6J and transgenic heterozygous mice with a null mutation for *Dhcr7* (Ex8) mice were purchased from Jackson Laboratories (Bar Harbor, Maine; catalog #007453). Mice were housed in an animal care facility with a standard 12-hour light and dark cycle and fed an *ad libitum* commercial rodent chow diet. Heterozygous *Dhcr7* (Ex8) mice were mated overnight, where the day after time-mating was designated embryonic day 0.5 (E0.5). Heterozygous mating produced WT, Het, and KO offspring at roughly the expected Mendelian 1:2:1 ratio. Animals were genotyped using PCR, as described previously (Fitzky et al., 2001). Brains were harvested from mice at E12.5, E14.5, E16.5 (n=3 per genotype), and PND0 (n=4 per genotype) time points. For the embryonic time points, the pregnant dam was anesthetized under

CO_2 and decapitated. For the PND0 time point, neonates were removed from cages after birth, anesthetized on ice, and decapitated. Whole brains were excised under the dissection scope in ice-cold PBS and frozen in pre-cooled 2-methylbutane to be stored at -80ºC until further processing steps.

4.4.3. RNA Isolation

E12.5, E14.5, and E16.5 whole brains and PND0 half brains (cut along the midsagittal plane) were processed for RNA sequencing. RNA was isolated using the Qiagen Lipid RNeasy Kit following the manufacturer's protocol. RNA quality was assessed with a NanoDrop One spectrophotometer (Thermo Scientific), and only samples with appropriate purity (260/280 ratio > 2.0 and 260/230 ratio > 2.0) were used for analysis. Gel electrophoresis was also used to check for DNA contamination and RNA integrity.

4.4.4. RNA Sequencing (Novogene)

Samples were sent to Novogene Co. Ltd (Sacramento, CA) for total RNA sequencing on their Illumina platform. RNA sample quality control was further assessed, and the mRNA library was prepared with additional polyA enrichment, RNA fragmentation, and cDNA transcription steps. Libraries were sequenced by 150 bp paired-end reads on the Illumina NovaSeq 6000 Sequencing System with a minimum sequencing read depth of 6 GB of raw data per sample.

4.4.5. Data Analysis

Data analysis was performed using a combination of Linux, R code, and various open-source online tools. We used an in-house-built Python script that streamlines raw data processing steps, utilizing zipped raw sequence read files to conserve disk memory space. *hisat2* is used to align sequence reads to the reference mouse genome (mm10), where greater than 95% sequence alignment was achieved (Kim et al., 2019). *samtools sort* and *featureCounts* are then used to

count reads to genomic features (annotation file VM25) (H. Li et al., 2009; Liao et al., 2014). The resulting sequence count data are input into DESeq2 (using R/Bioconductor) for differential expression analysis (Love et al., 2014). DESeq2 uses a generalized linear model with negative binomial distribution to estimate dispersion and the Wald significance test. Independent filtering step removes genes with very low counts. For pathway analysis, we utilized iPathwayGuide and Database for Annotation, Visualization, and Interpretation (DAVID) (Dennis et al., 2003; Donato et al., 2013; Draghici et al., 2007; Sherman et al., 2022). For both iPathwayGuide and DAVID, we used a list of all measured genes specific for each time point as the reference background lists.

4.4.6. Data Availability

Raw RNA-seq data has been deposited in NCBI's Gene Expression Omnibus (GEO) and is available with the GEO Accession Number: GSE247566.

4.5 Conclusion

We have performed transcriptomic analysis of whole brains from *Dhcr7*-KO and WT mice at three embryonic time points and one postnatal time point. Comparative analysis of differentially expressed genes and pathway analysis shows the altered regulation of different physiological processes that could be related to the neurological phenotype in SLOS. Early time points suggest downregulation of genes and pathways involved in embryonic development, such as Hippo, Wnt, and TGF-β, and later time points suggest universal defective neuronal synapse pathways. In addition, the ribosome was found to be another novel pathway affected by deficient cholesterol biosynthesis at three time points. Thus, disruption of cholesterol synthesis through genetic mutation of *Dhcr7* has deleterious and concerted effects beyond those expected in simply sterol and lipid homeostasis.

Figures

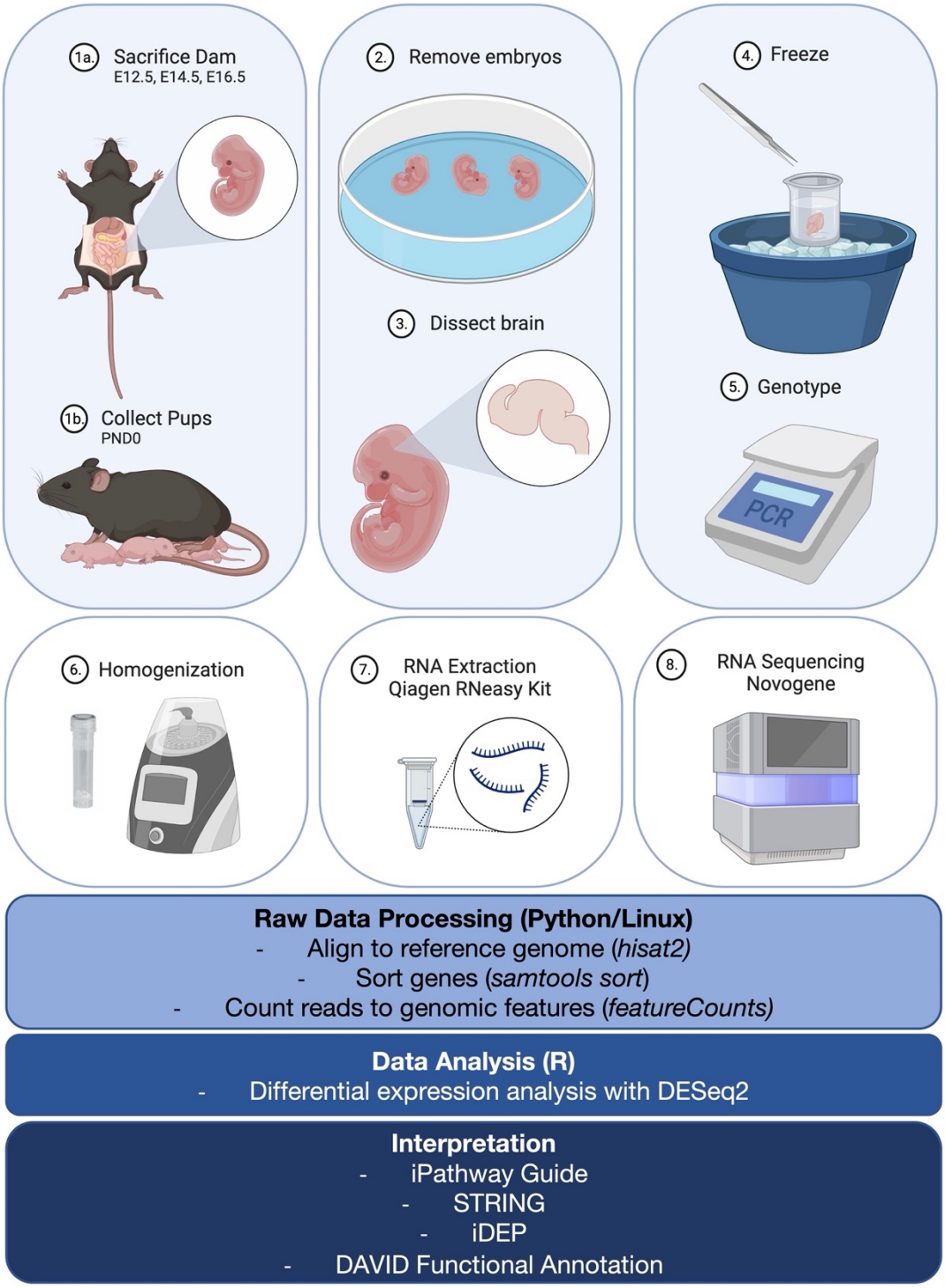

Figure 4.1 Diagram of RNA sequencing workflow. Steps for sample preparation (brain tissue collection from mouse embryos or neonates), RNA extraction, RNA sequencing, and data analysis are outlined. Created with BioRender.com.

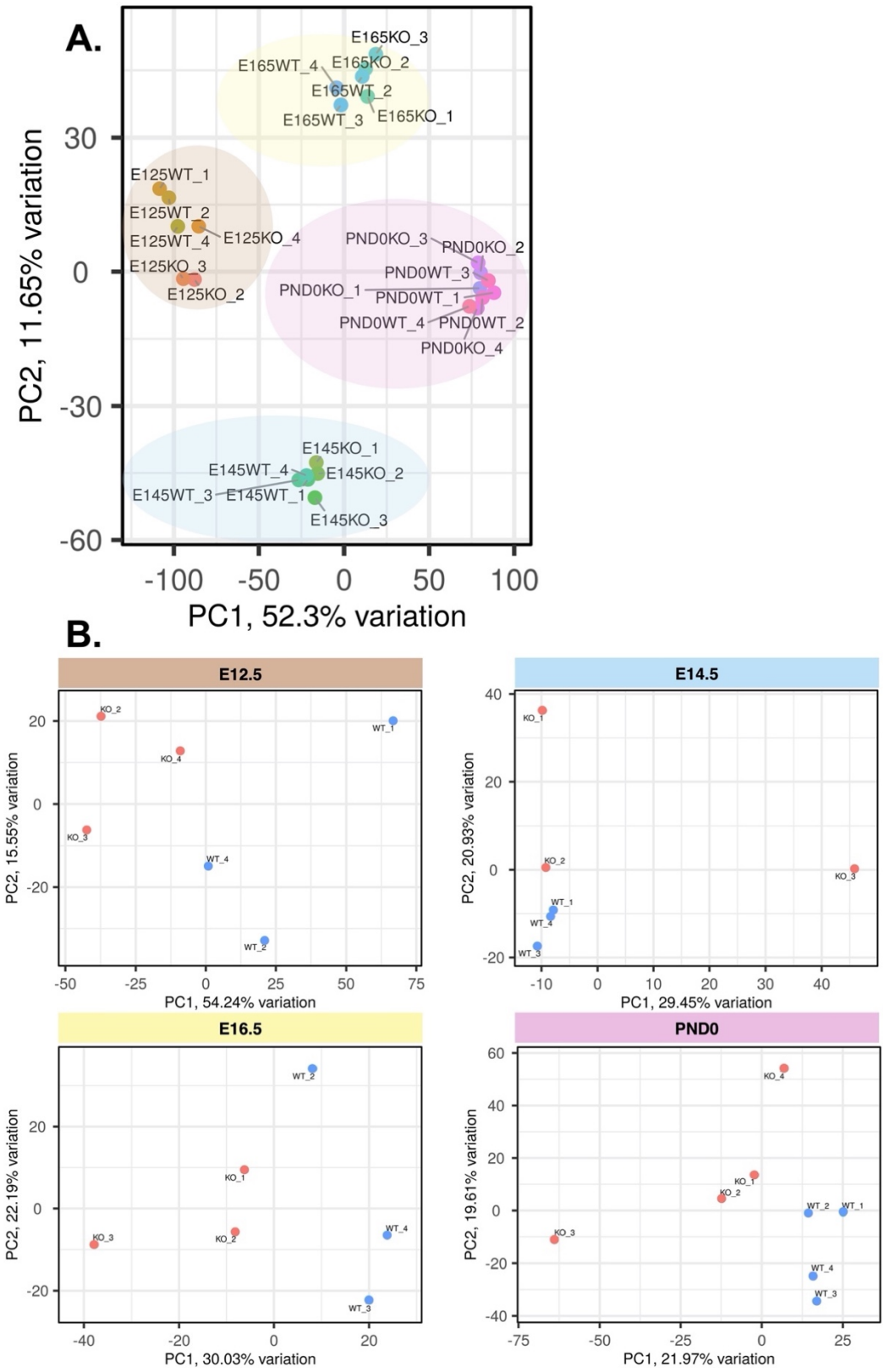

Figure 4.2 PCA bi-plots for **A.** all groups combined and **B.** individual time points. Created by iDEP1.1.

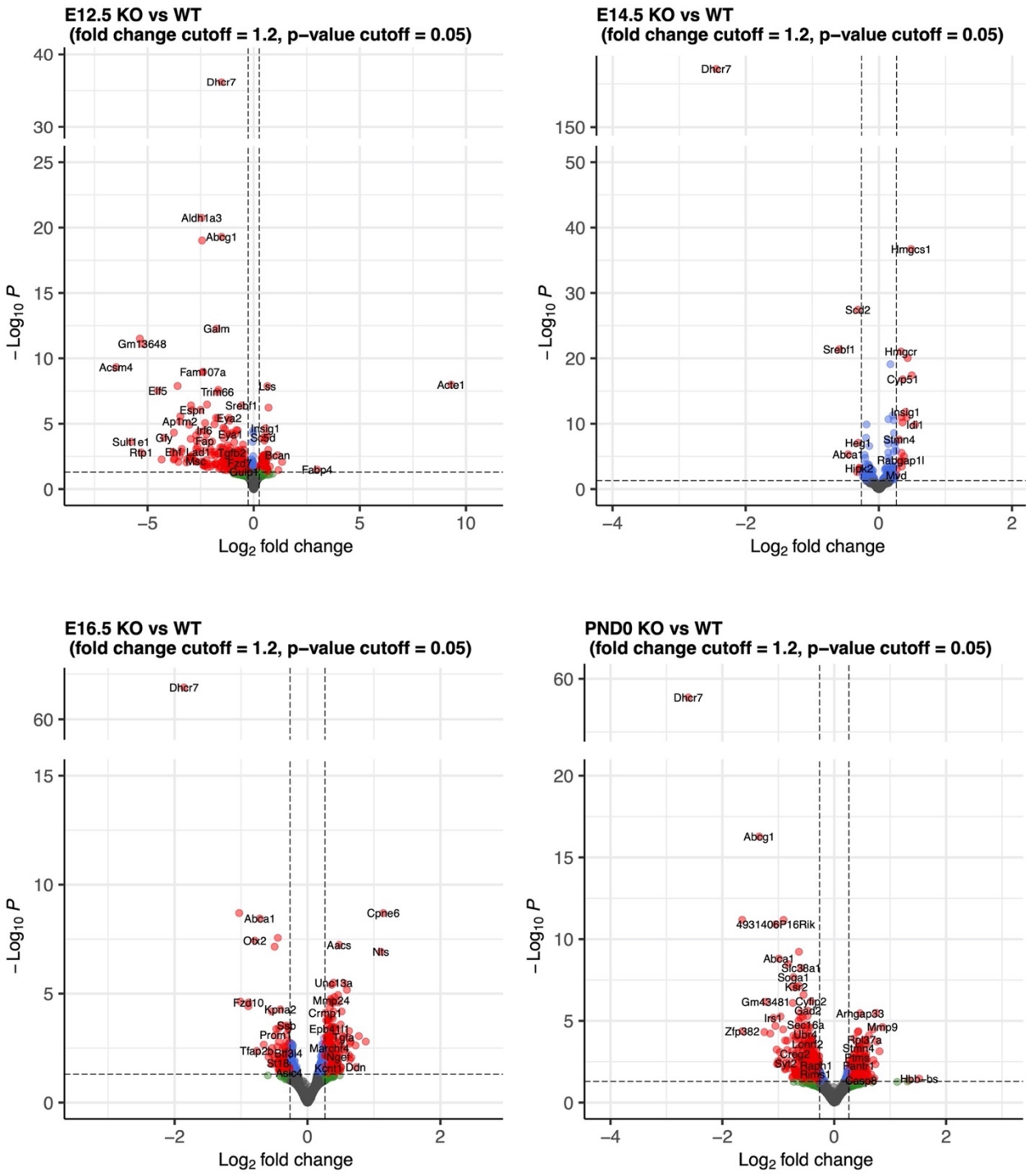

Figure 4.3 Volcano plots highlighting differentially expressed genes (shown in red) filtered by adjusted p-value ≤0.05 (shown in blue) and fold-change ≥1.2 (shown in green). The complete list of DEGs is available in **Table S4.1**. Created with R/*EnhancedVolcano.*

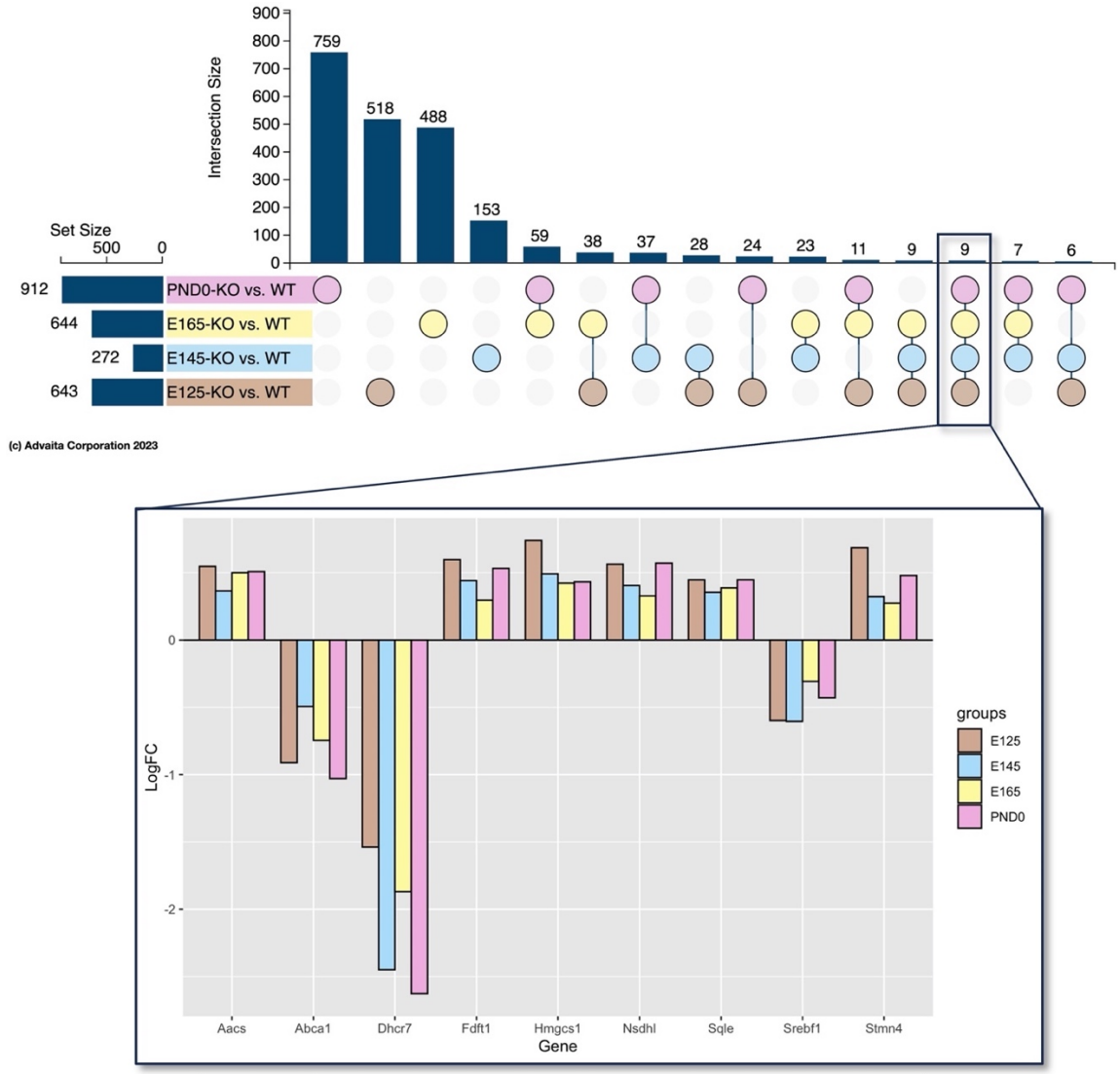

Dhcr7	7-dehydrocholesterol reductase
Nsdhl	NAD(P) dependent steroid dehydrogenase-like
Srebf1	sterol regulatory element binding transcription factor 1
Abca1	ATP-binding cassette, sub-family A (ABC1), member 1
Sqle	squalene epoxidase
Stmn4	stathmin-like 4
Hmgcs1	3-hydroxy-3-methylglutaryl-Coenzyme A synthase 1
Fdft1	farnesyl diphosphate farnesyl transferase 1
Aacs	acetoacetyl-CoA synthetase

Figure 4.4 UpSet plot for meta-analysis of differentially expressed genes from all four time points. Bar plot displaying log fold-change values for the nine shared genes from all four time points and table of gene annotations. Created by iPathwayGuide and R/*ggplot2*.

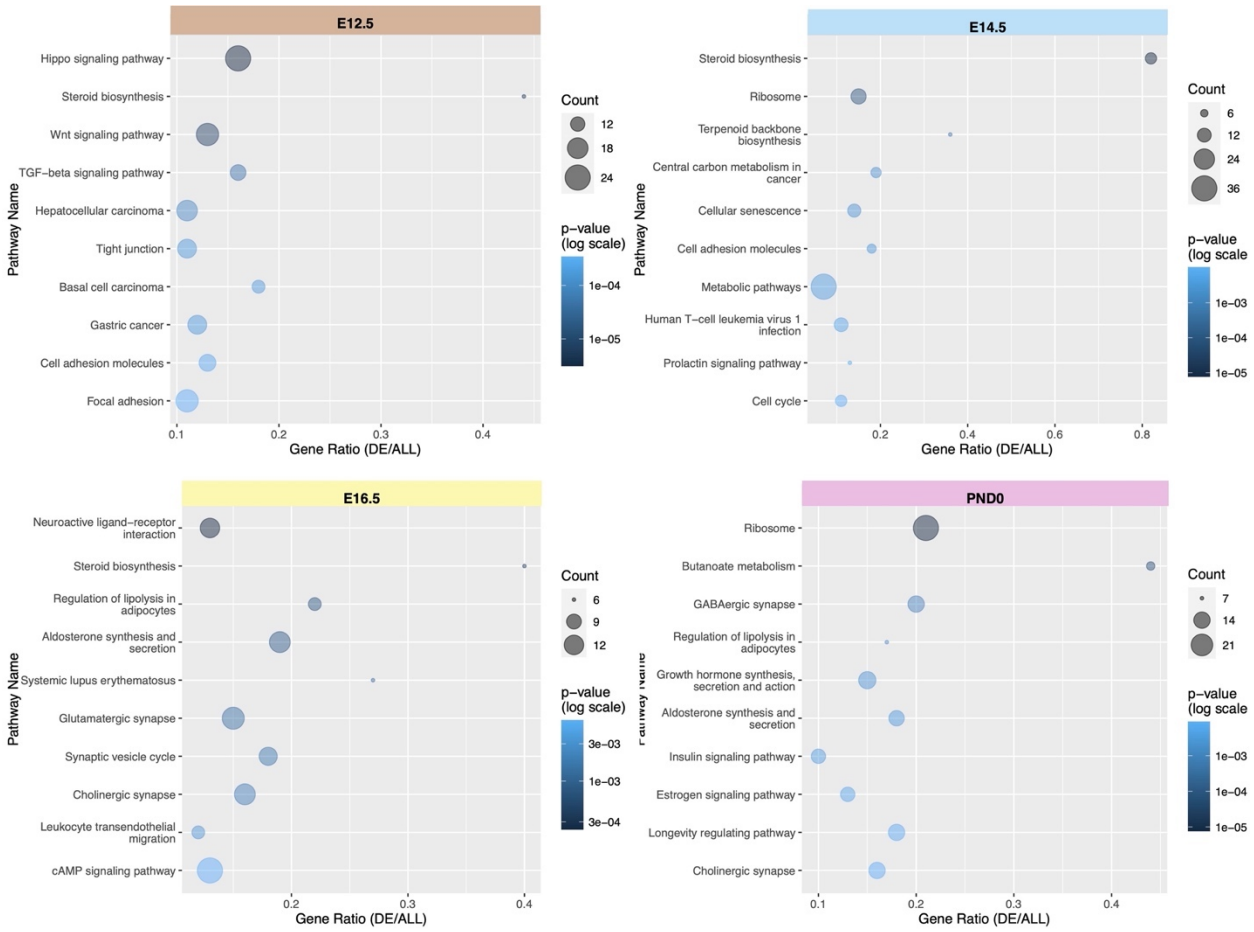

Figure 4.5 Top 10 affected pathways from pathway analysis using iPathwayGuide. Bubble plots are ordered by p-value, and display pathway name and gene ratio, where the size of the bubble designates the number of differentially expressed genes, and the color designates the p-value. * COVID-19 removed from E14.5, E16.5, and PND0 time points. Created by R/*ggplot2*.

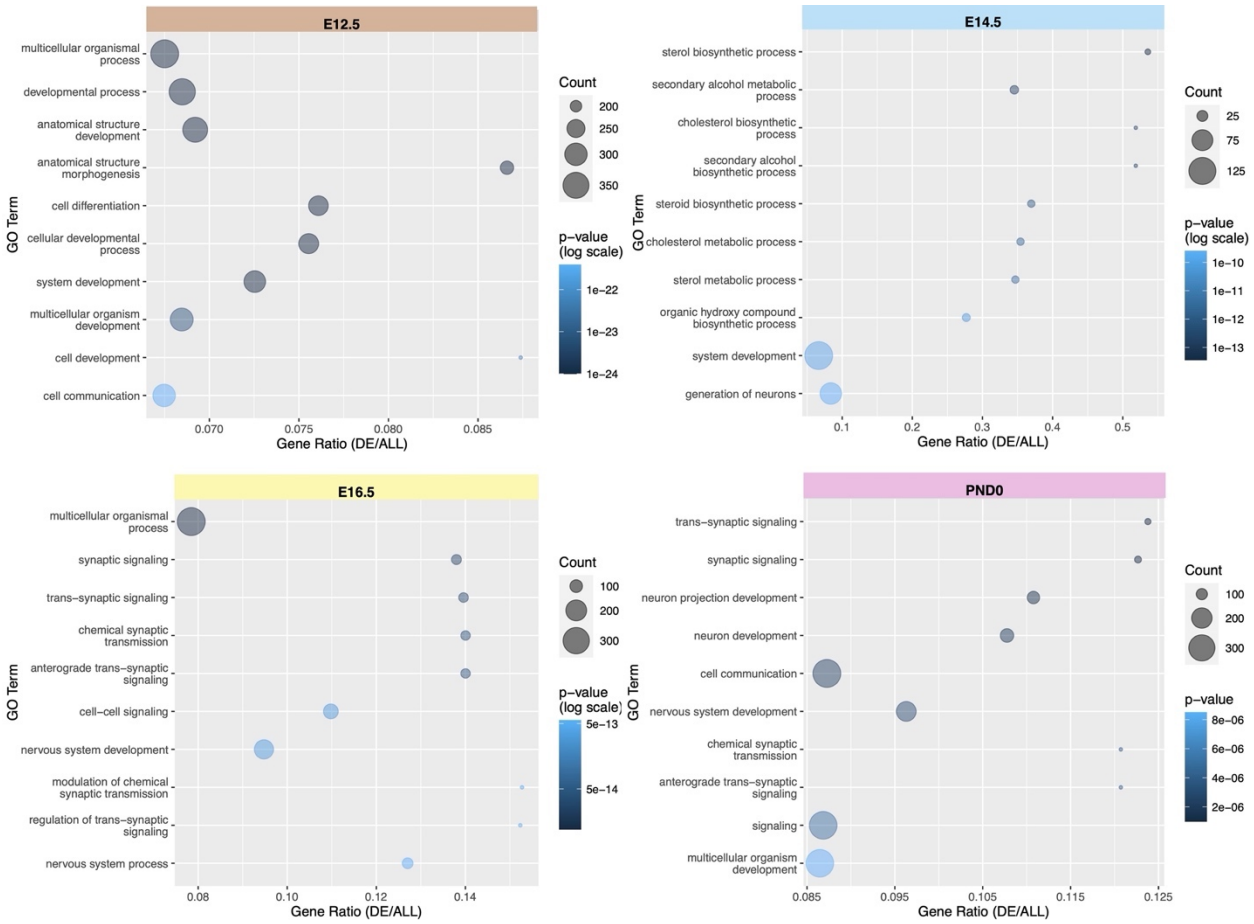

Figure 4.6 Top 10 enriched GO terms using iPathwayGuide. Bubble plots are ordered by p-value and display pathway name and gene ratio, where the size of the bubble designates the number of differentially expressed genes and the color designates p-value.

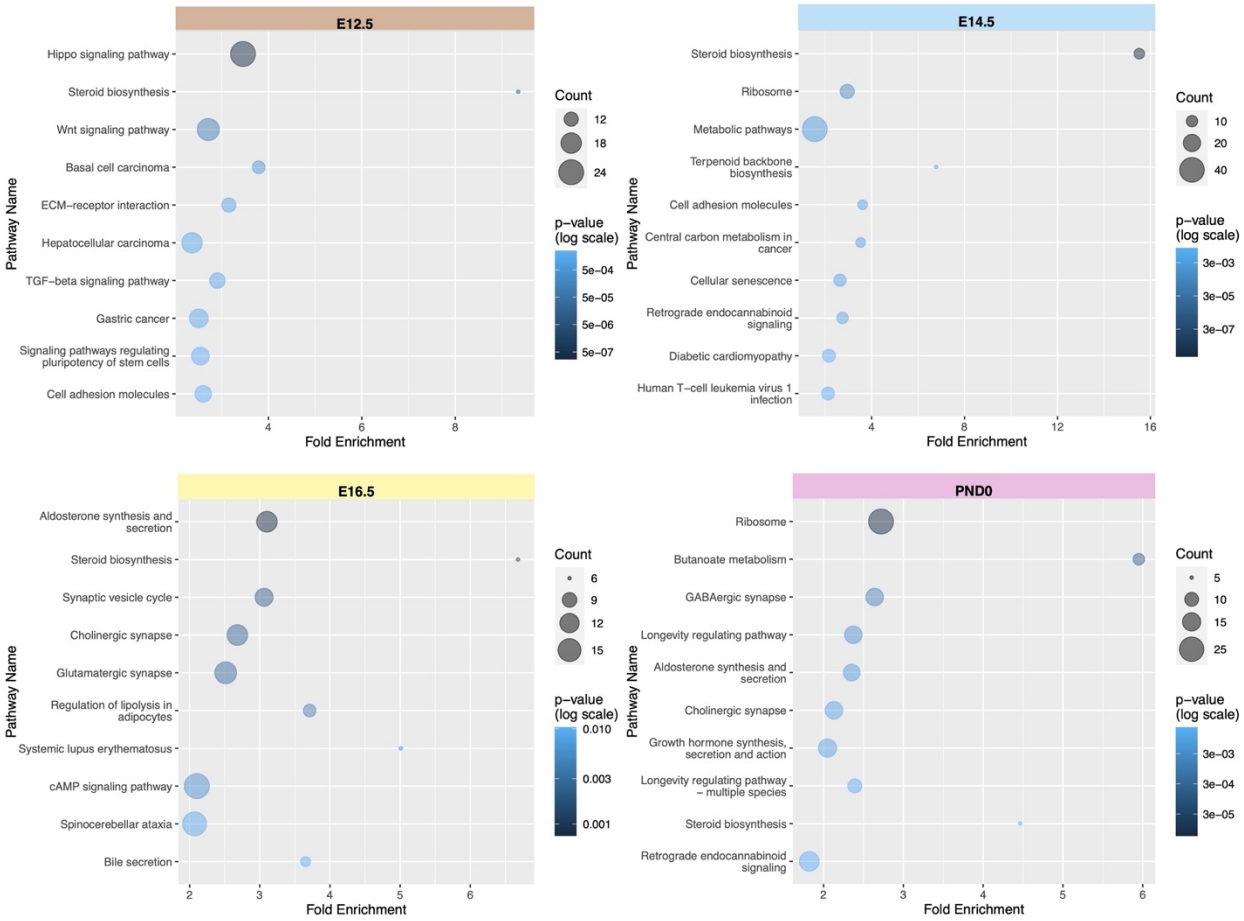

Figure 4.7 Top 10 enriched pathways from pathway analysis using DAVID. Bubble plots are ordered by p-value, and display pathway name and Fold Enrichment, where the size of the bubble designates the number of differentially expressed genes, and the color designates the p-value.

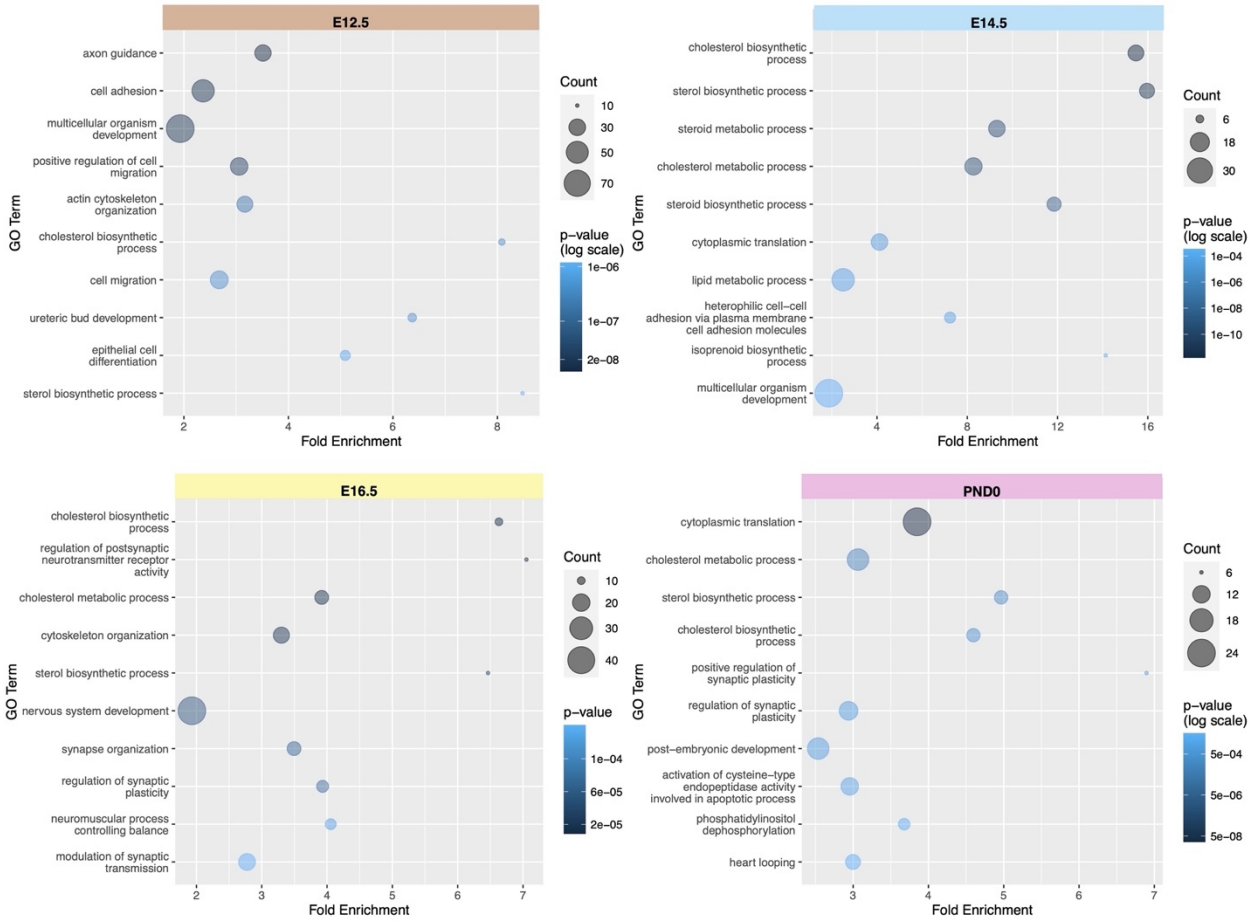

Figure 4.8 Top 10 enriched GO terms using DAVID. Bubble plots are ordered by p-value, and display pathway name and Fold Enrichment, where the size of the bubble designates the number of differentially expressed genes, and the color designates the p-value.

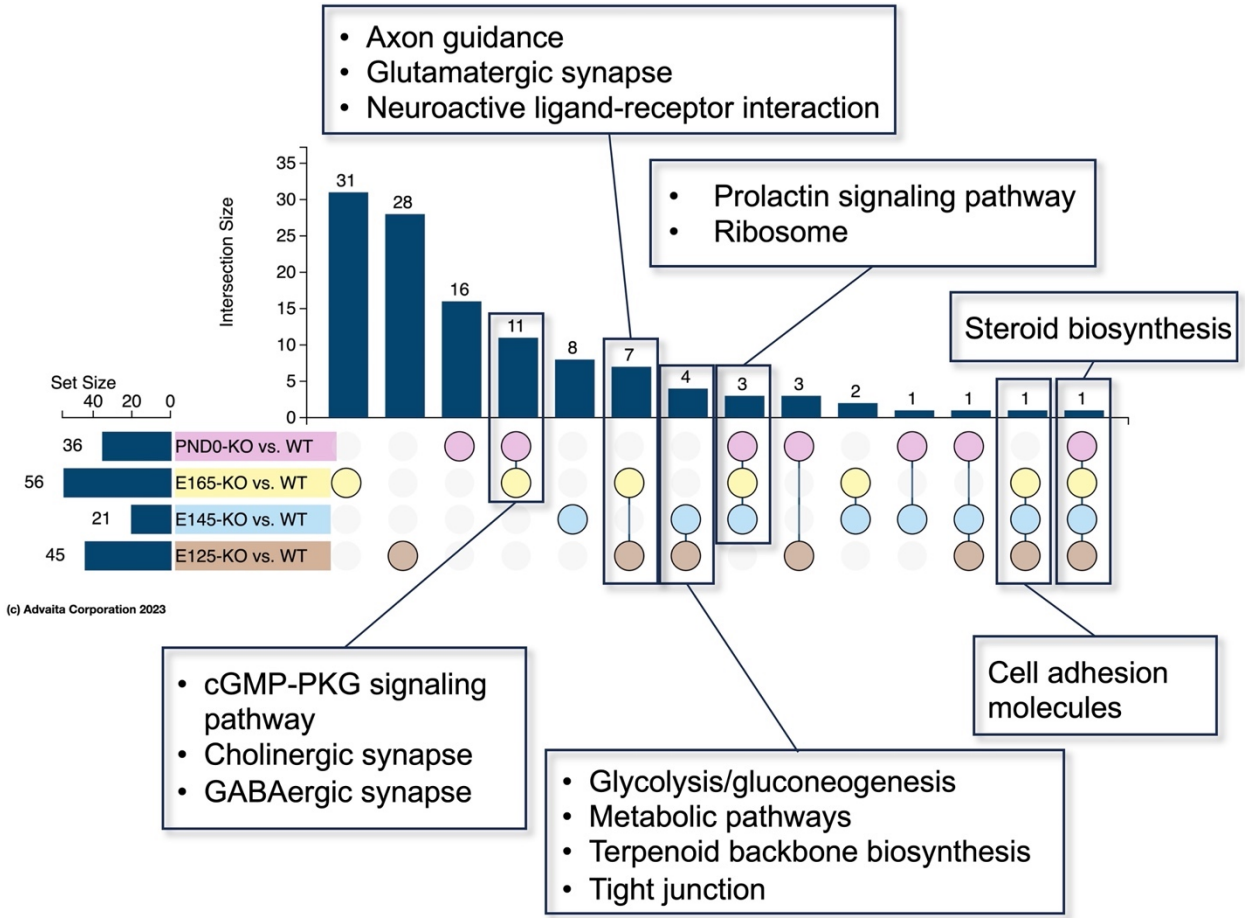

Figure 4.9 UpSet plot for meta-analysis of shared pathway hits from all time points with some specific pathways listed. All pathway results are available in **Table S4.2**.
No p-value correction for multiple hypothesis testing was applied for pathway hits.
Created by iPathwayGuide.

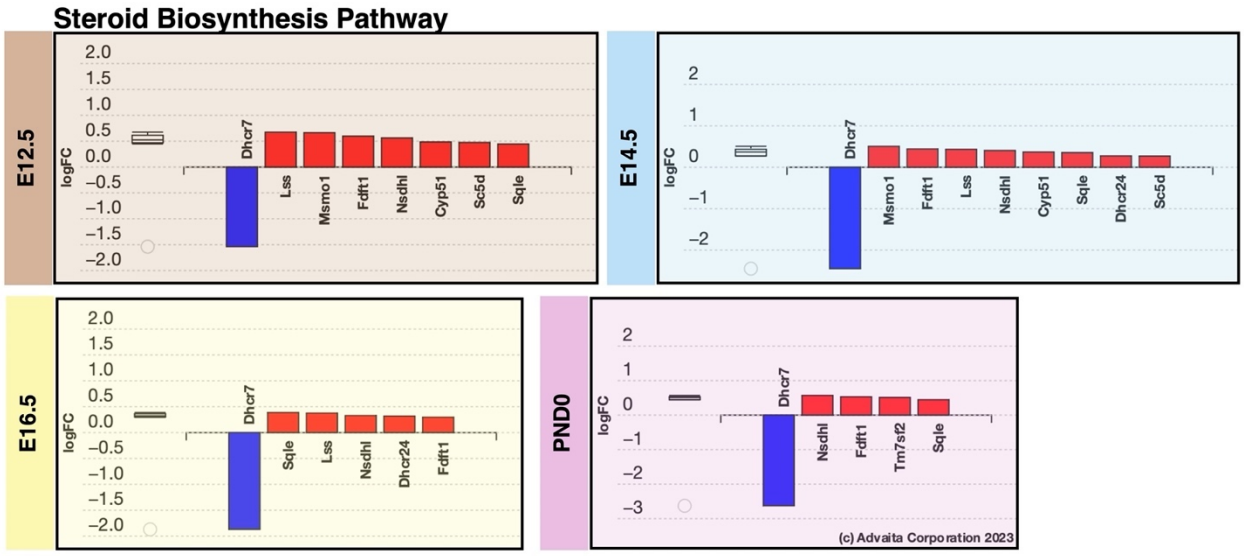

Figure 4.10 Bar plots of log fold-changes for DEGs in the **steroid biosynthesis pathway** (mmu:00100) for time points where this pathway had a p-value ≤ 0.05. DEGs are ordered by absolute LFC.

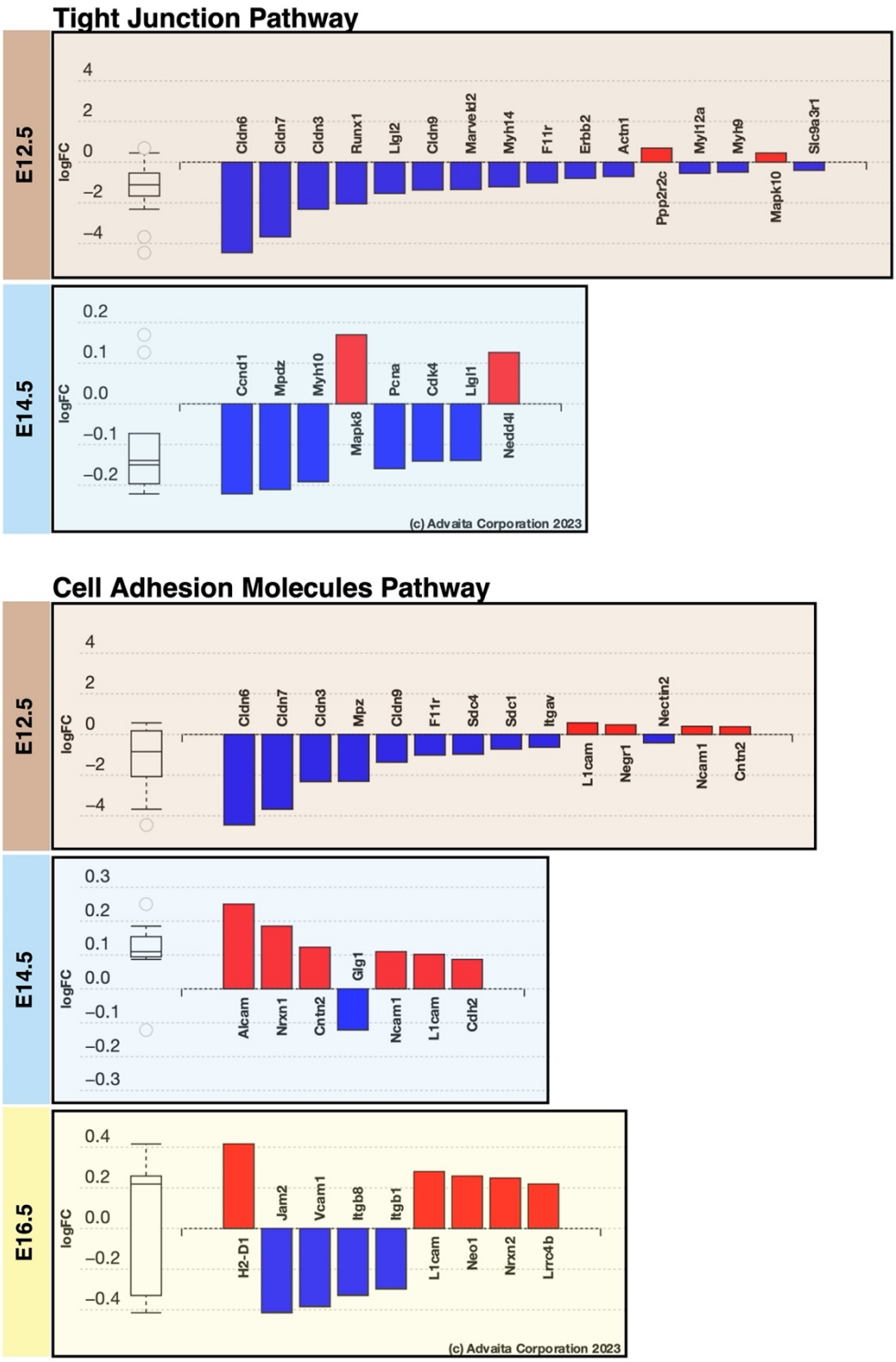

Figure 4.11 Bar plots of log fold-changes for DEGs in the **tight junction** (mmu:04530) and **cell adhesion molecules pathways** (mmu:04515) for time points where these pathways had a p-value ≤ 0.05.

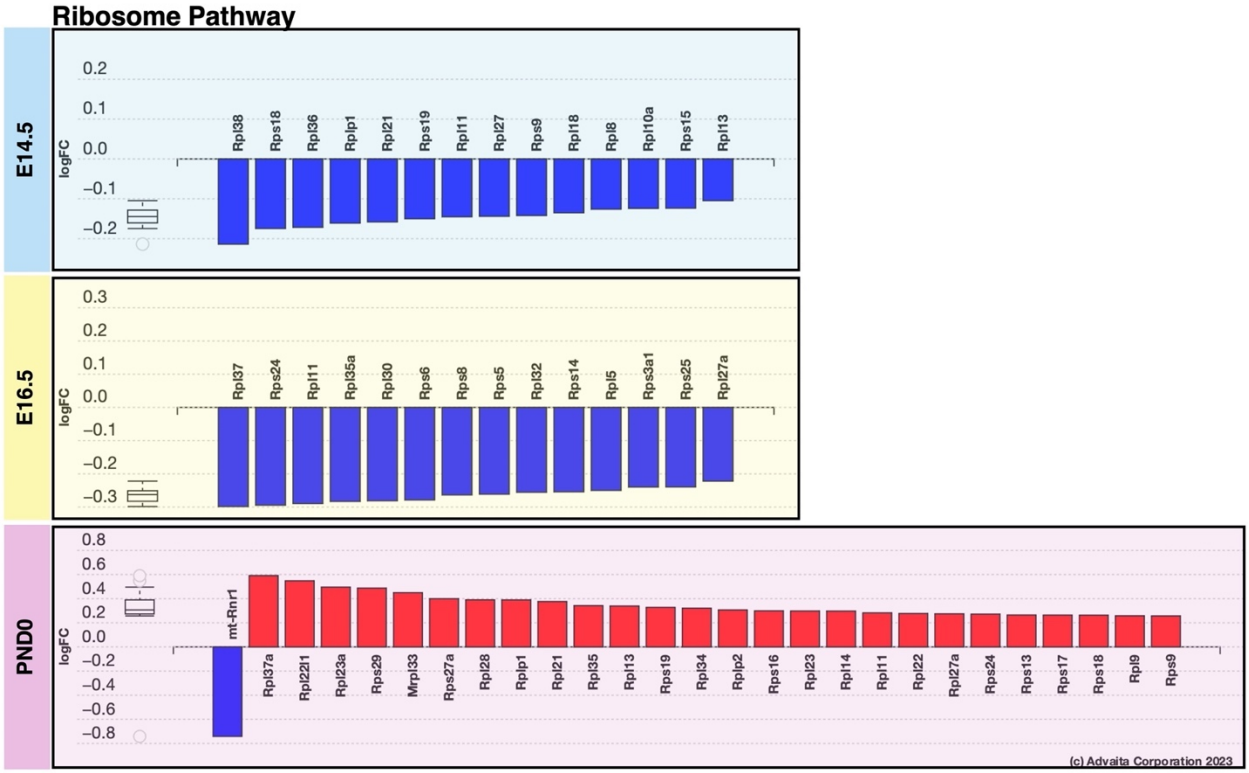

Figure 4.12 Bar plots of log fold-changes for DEGs in the **ribosome pathway** (mmu:03010) for time points where this pathway had a p-value ≤ 0.05.

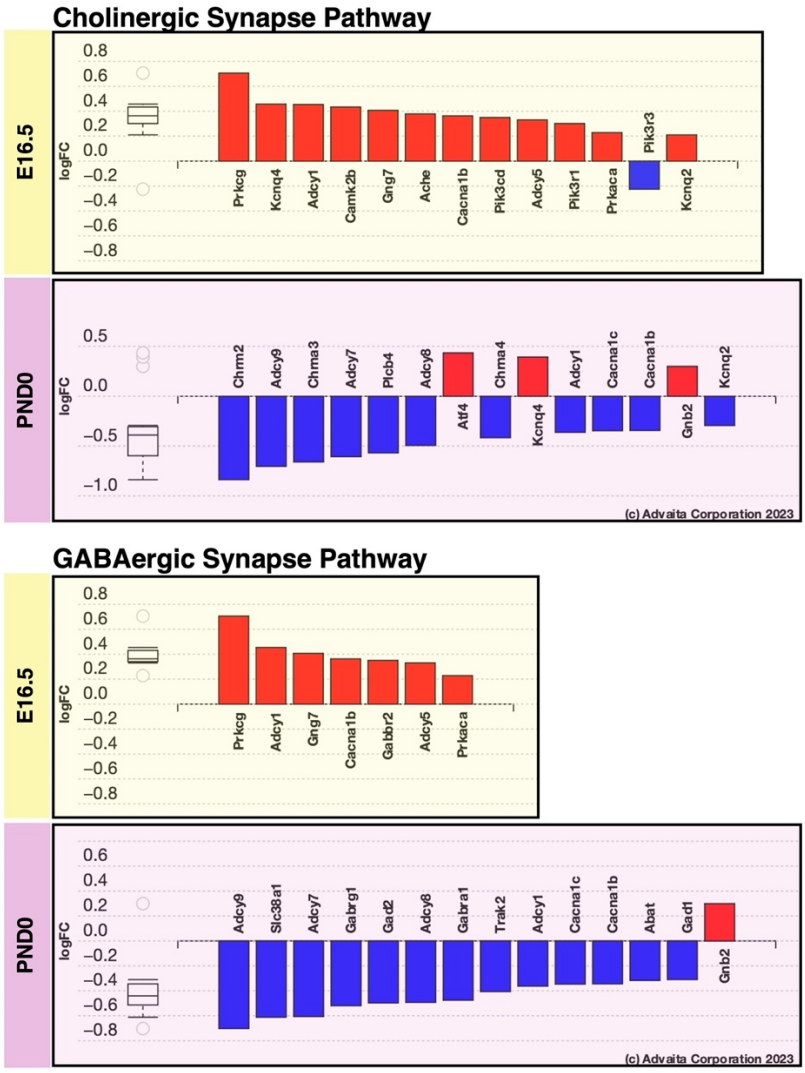

Figure 4.13 Bar plots of log fold-changes for DEGs in the **cholinergic** (mmu:04725) and **GABAergic synapse pathways** (mmu:04727) for time points where these pathways had a p-value ≤ 0.05.

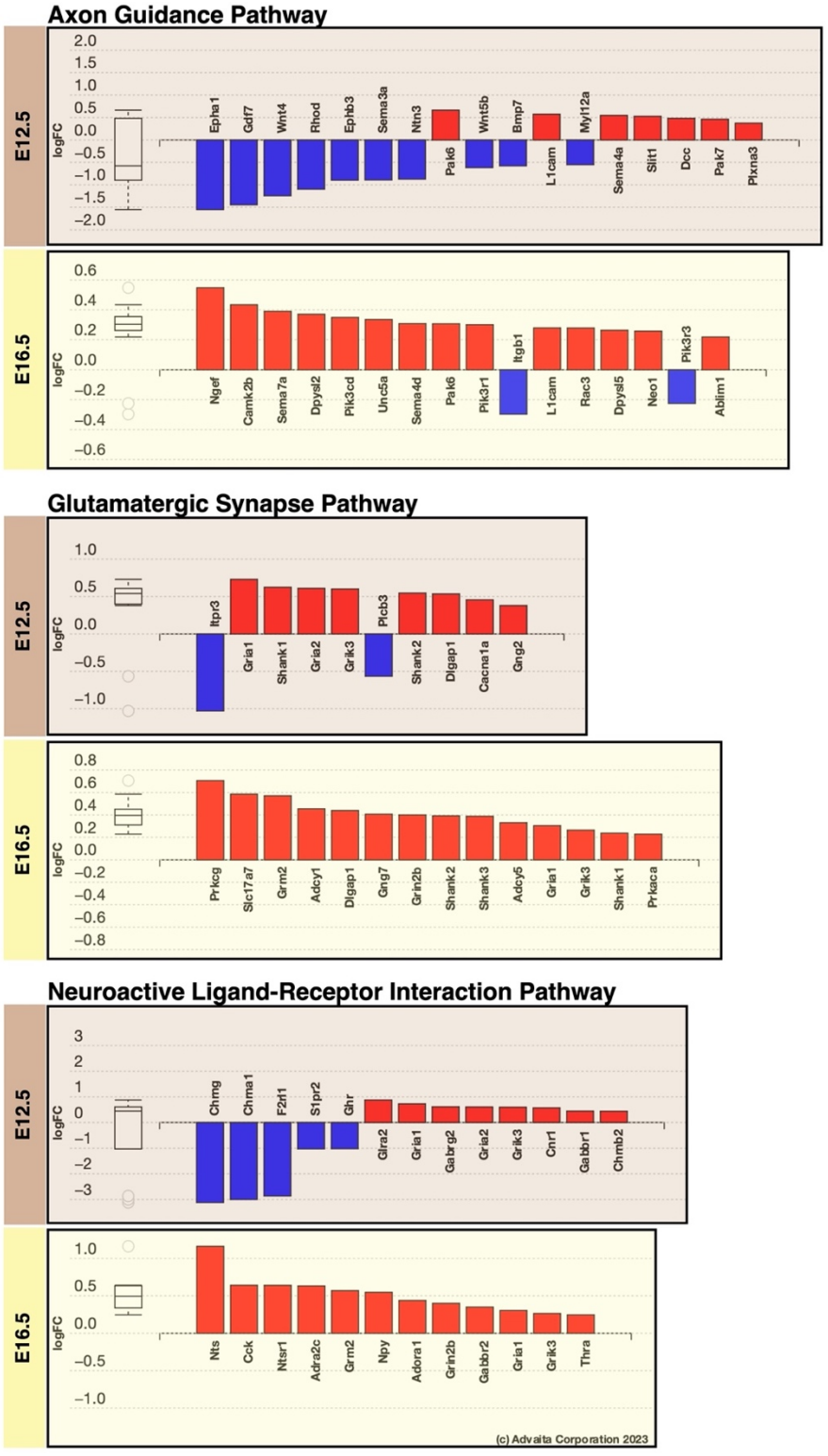

Figure 4.14 Bar plots of log fold-changes for DEGs in the **axon guidance** (mmu:04360), **glutamatergic synapse** (mmu:04724), and **neuroactive ligand-receptor interaction pathways** (mmu:04080) for time points where these pathways had a p-value ≤ 0.05.

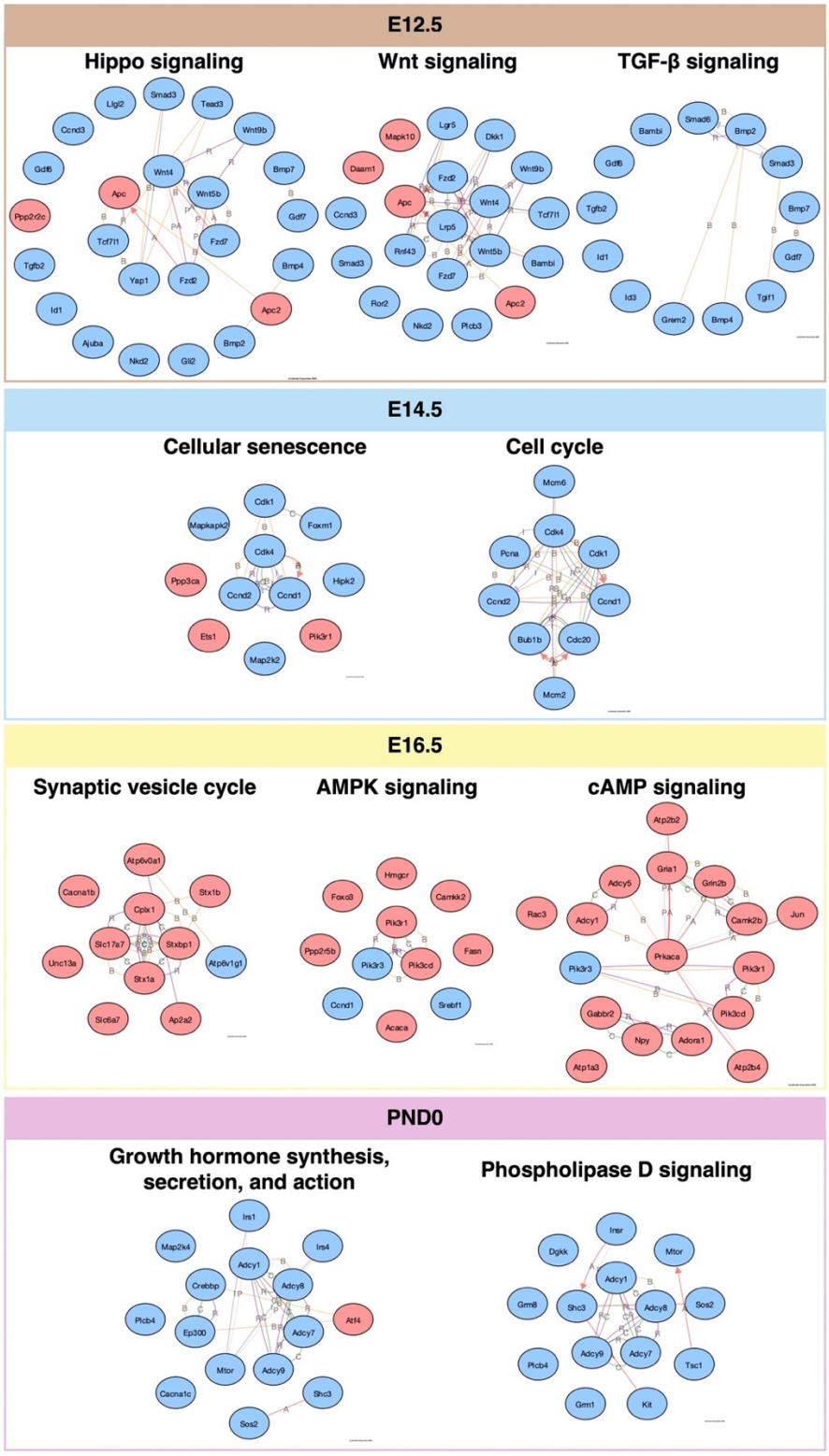

Figure 4.15 Interaction networks of DEGs in unique signaling pathways that are significantly affected at each time point (p-value ≤ 0.05). Up-regulated genes are shown in red, and down-regulated genes are in blue. Created by iPathwayGuide.

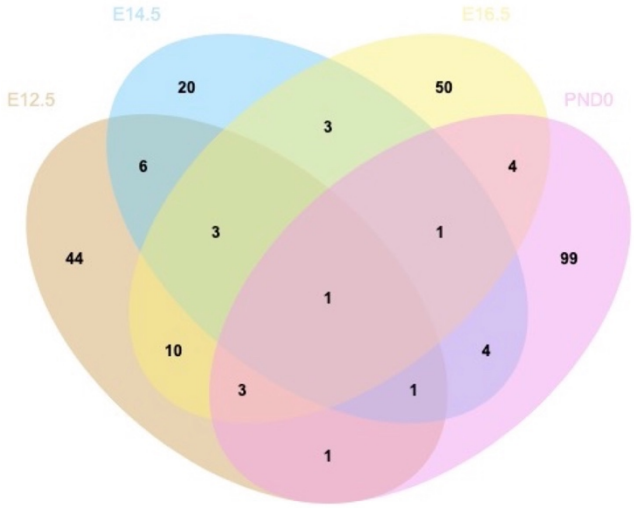

Shared by Two Time Points

E12|E14	E12|E16	E12|PND0	E14|E16	E14|PND0	E16|PND0
GRIA2	*ELAVL2*	*LMTK3*	*TBR1*	*CLASP1*	*DST*
GPR85	*GRIK3*		*UNC13A*	*CHD7*	*MAP1A*
GRB10	*NOVA2*		*DPYSL2*	*AGO1*	*KCNB1*
UNC79	*SHANK1*			*PRPF8*	*THRA*
KCNQ3	*SHANK2*				
ZBTB20	*MYO16*				
	GRIA1				
	MAPT				
	MAP1B				
	DLGAP1				

Shared by Three or All Time Points

E12|E14|E16	E12|E14|PND0	E12|E16|PND0	E14|E16|PND0	All
STXBP1	*FAT1*	*CACNA1B*	*HERC2*	*DHCR7***
LDLR		*KCNQ2*		
TSPAN7		*KCTD13*		

Figure 4.16 Venn diagram of DEGs shared with SFARI autism gene database at each time point.

Tables

Excel spreadsheet tables are accessible as Supporting Info in the preprint:

> Amy Li, Hideaki Tomita, and Libin Xu, Temporal gene expression changes and affected pathways in neurodevelopment of a mouse model of Smith-Lemli-Opitz syndrome, *bioRxiv*, (**2023**). doi:10.1101/2023.11.21.568116.

Table S4.1 List of differentially expressed genes for each time point with an adjusted p-value (FDR) ≤ 0.05.

Table S4.2 List of enriched KEGG pathways for each time point with a p-value ≤ 0.05.

Table S4.3 List of enriched GO Biological Process terms for each time point with an adjusted p-value (FDR) ≤ 0.05.

Table 4.4 Summary of differentially expressed genes, with an adjusted p-value threshold (FDR ≤ 0.05), or an adjusted p-value threshold and a fold-change threshold (|FC| ≥ 1.2), and the total number of genes with measured expression (after DESeq2 filtering of genes with an extreme count outlier and low mean normalized counts).

Time Point	Number of DEGs (FDR ≤ 0.05)	Number of DEGs (FDR ≤ 0.05 and |FC| ≥ 1.2)	Total Number of Measured Genes
E12.5	647 (Up: 213; Down: 434)	644 (Up: 212; Down: 432)	17386
E14.5	279 (Up: 129; Down: 150)	42 (Up: 29; Down: 13)	6559
E16.5	645 (Up: 391; Down: 254)	470 (Up: 297, Down: 173)	11674
PND0	919 (Up: 391; Down: 528)	844 (Up: 369; Down: 515)	13145

Table 4.5 Functional annotation chart from DAVID enrichment analysis of shared DEGs between SLOS and SFARI autism database.

KEGG Pathway	Count	Genes	p-value
Glutamatergic synapse	6	*GRIA1, GRIA2, GRIK3, DLGAP1, SHANK2, SHANK1*	5.6E-6
Nicotine addiction	3	*GRIA1, GRIA2, CACNA1B*	3.9E-3
Synaptic vesicle cycle	3	*UNC13A, STXBP1, CACNA1B*	1.4E-2
Cholinergic synapse	3	*KCNQ2, KCNQ3, CACNA1B*	2.8E-2
Dopaminergic synapse	3	*GRIA1, GRIA2, CACNA1B*	4.0E-2
Retrograde endocannabinoid signaling	3	*GRIA1, GRIA2, CACNA1B*	4.7E-2

Chapter 5 Conclusion and Future Directions

The results from this work highlight that dysregulated lipid metabolism and altered gene expression beyond the loss of *Dhcr7* and defective cholesterol biosynthesis occur in the pathophysiology of SLOS. **Chapter 2** discussed altered lipid metabolic pathways that were determined by an untargeted lipidomics analysis of *Dhcr7*-KO mouse brains across embryonic time points (E12.5, E14.5, and E16.5) to postnatal time point (PND0). We confirmed the accumulation of oxysterol metabolites of 7-DHC and other interesting differentially expressed lipid classes, such as monoacylglyceride species and sphingomyelin. We discussed the implications of altered glycerolipid, glycerophospholipid, and sphingolipid metabolism and their effect on biological processes, such as synaptic signaling, lipid raft formation, myelination, and inflammation in SLOS pathophysiology. In **Chapter 3**, we applied MALDI-IM-MS to determine the regional distribution of features that correspond to cholesterol, 7-DHC/desmosterol, and the precursor of desmosterol, 7-dehydrodesmosterol, in WT and *Dhcr7*-KO mice at PND0. Interestingly, we also observed *m/z* values that match the major oxysterol metabolites of 7-DHC (DHCEO and hydroxy-7-DHC), which displayed similar patterns as 7-DHC. Subsequent statistical analysis of regions-of-interest allowed us to identify differentially expressed lipids between *Dhcr7*-KO and WT brains, which could contribute to defects in myelination, neurogenesis, neuroinflammation, and learning and memory in SLOS. In **Chapter 4**, we discussed a complementary transcriptomics analysis to **Chapter 2**, where we observed the expected downregulation of the *Dhcr7* transcript in the *Dhcr7*-KO mouse model, as well as gene expression changes of several other genes involved in cholesterol biosynthesis throughout all time points. Pathway and GO term enrichment analyses revealed affected signaling pathways and biological processes that were shared amongst time points and unique to individual time

points. Specifically, the pathways important for embryonic development, including Hippo, Wnt, and TGF-β signaling pathways, are the most significantly affected at the earliest time point, E12.5. Additionally, neurogenesis-related GO terms were enriched in earlier time points, consistent with the timing of development. Conversely, pathways related to synaptogenesis, which occurs later in development compared to neurogenesis, are significantly affected at the later time points, E16.5 and PND0, including the cholinergic, glutamatergic, and GABAergic synapses. The impact of these transcriptomic changes and enriched pathways was discussed in the context of known biological phenotypes of SLOS.

Finally, some findings from this dissertation warrant further investigation. For example, gene expression changes determined by RNA sequencing in **Chapter 4** should be confirmed by western blot or immunohistochemistry (IHC) to examine whether the observed gene expression changes lead to protein level changes. Protein targets of interest include those involved in the affected neurotransmission-related signaling pathways, such as the GABA receptor subunit alpha-1 (GABRA1) and adenylate cyclase 1 (ADCY1) in the GABAergic synapse pathway. The myelination defect suggested by lipidomics studies in **Chapters 2** and **3** can also be investigated further by IHC using luxol-fast blue (LFB) (Kluver & Barrera, 1953). Since myelination is mostly a postnatal process, we propose using the conditional-KO mouse model to study postnatal phenotypes in adolescent mice.

Appendix A. Lipidomics by HILIC-Ion Mobility-Mass Spectrometry

Portions of this chapter have been adapted and reproduced with permission from:

> Amy Li, Kelly M. Hines, and Libin Xu, Lipidomics by HILIC-Ion Mobility-Mass Spectrometry, *Methods Mol Biol*, 2084:119-132, (**2020**).

A.1 Introduction

In recent years, the advancement of singular and multi-disciplinary 'omics technologies has quickly taken storm as a systems biology approach is applied to biomedical research. They are highly informative experiments that can reveal molecular changes within some altered state of a system, such as a disease or a treatment condition (Jurowski et al., 2017). The central biological processes of DNA transcription to mRNA, subsequent protein translation, and eventual production of metabolites correspond to the studies of genomics, transcriptomics, proteomics, and metabolomics, respectively. Lipidomics falls under the category of metabolomics as the lipidome represents a major fraction of the human metabolome (Wishart et al., 2009). Specifically, lipidomics aims to systematically identify and quantify individual lipid species within cells, tissues, or an organism and map out the complex interactions between lipids and other macromolecules. There is growing evidence that lipids are closely related to the onset and progression of several diseases, including neurodegenerative, neurodevelopmental, cardiovascular, and metabolic disorders. Thus, lipidomics represents a unique niche to address specific questions about the role of altered lipid metabolism within disease etiologies and advance biomarker identifications to aid diagnosis (Rustam & Reid, 2018).

Lipids cover a diverse range of functions within the cell as structural components of membranes, energy reservoirs, and signaling molecules, which reflects their large chemical diversity. There are eight main lipid classes (FA, fatty acyls; GL, glycerolipids; GP, glycerophospholipids; SP, sphingolipids; ST, sterol lipids; PR, prenol lipids; SL, saccharolipids;

PK, polyketides) and multiple subclasses (Fahy et al., 2005; Fahy et al., 2009). Further variations are possible within each subclass from multiple types of head groups, backbones, fatty acyl chains, linkages (ester, ether, or vinyl ether), and other accessory modifications, like sugar molecules (Fahy et al., 2005; Fahy et al., 2009). This vast combinatorial space is estimated (by the LIPID MAPS database) to contain over 40,000 distinct lipids. This presents a significant analytical challenge for lipidomics because most lipid species occupy a narrow mass range of 600 – 900 *m/z*. Modern mass spectrometry has dramatically advanced the field of lipidomics and increased coverage of the lipidome over the past two decades, but some limitations remain.

Mass spectrometry-based lipidomics can be divided into two categories: shotgun (Han et al., 2005; Schwudke et al., 2007) and liquid chromatography (LC)-based experiments (Ivanova et al., 2007; Merrill et al., 2005; O. Quehenberger, et al., 2010). In shotgun lipidomics, samples are directly infused into the mass spectrometer without any prior chromatographic separation, aiming to maximize the throughput of analysis. However, this approach cannot resolve isomeric and isobaric lipids and limits the detection of lower abundance lipids due to ion suppression. LC-based lipidomics involves LC separation, such as normal phase (NP), reverse phase (RP), or hydrophilic interaction liquid chromatography (HILIC), prior to ionization. RP separation utilizes nonpolar C18 columns with polar solvents, where lipids are separated based on hydrophobicity, resulting in separation by chain length and degree of unsaturation of fatty acyl chains. HILIC separation utilizes columns with polar stationary phase in combination with typical reverse phase solvents, such as acetonitrile and water, where lipids partition at the water/silica interface. HILIC separation is mostly dependent on the polarity of lipid head groups (Baker et al., 2014; Cifkova et al., 2012). Further separation, although to a lesser extent, occurs within each subclass by chain length and degree of unsaturation of fatty acyl chains.

Ion mobility (IM) is another technology that has gained popularity and shown advantages in lipidomics studies as it contributes to both separation and structural elucidation of analytes and can be coupled to LC separation without affecting throughput (K. Hines et al., 2017; K. M. Hines et al., 2017; Hinz et al., 2018; Kliman et al., 2011). Ions are separated based on their size, shape, and charge as they are pushed through a drift tube by an electric field through an opposing flow of inert gas (Fenn & McLean, 2008; Kliman et al., 2011; McLean et al., 2005). Drift times are related to a physicochemical property called collisional cross section (CCS), which can be measured either directly on a drift tube-IM (DTIM) instrument using the Mason-Schamp equation (Mason & McDaniel, 1988; Mason & Schamp Jr, 1958) or on a traveling wave-IM (TWIM) instrument through calibration (Forsythe et al., 2015; Hines et al., 2016; Ruotolo et al., 2008). Previous papers from our group have shown that in TWIM experiments, matched lipid calibrants produce more accurate and precise CCS values of lipid standards compared to calibration by calibrants from other classes of molecules, such as poly-DL-alanine, tetraalkylammonium compounds, and hexakis(fluoroalkoxy)phosphazines (Hines et al., 2016). IM is a gas-phase technique that is orthogonal to LC and enables the separation of lipid ions from other classes of macromolecules due to their distinct IM profiles (Fenn et al., 2009; May et al., 2014). Even within total lipids, individual lipid classes can be separated from each other, although the complete resolution of certain species is still limited by instrumentation (K. M. Hines et al., 2017; Kyle et al., 2016; Paglia et al., 2015; Zhou et al., 2017). Coupled with retention times (RT) and mass-to-charge (*m/z*) ratios, CCS values greatly increase the confidence in lipid identifications. Recently, the Zhu Lab reported the first platform for lipid identification using multidimensional RT-*m/z*-CCS data, LipidIMMS, which can utilize both RP-IM-MS and HILIC-IM-MS data (Zhou et al., 2018).

Herein, we discuss the use of our HILIC-IM-MS protocol (K. Hines et al., 2017; K. M. Hines et al., 2017) for the analysis of lipid species in the lipid extracts of biological samples using brain tissues and cells as examples. The workflow involves (1) sample preparation, including tissue homogenization, lysis, and liquid phase extraction; (2) data acquisition on a Waters SYNAPT HDMS G2-Si Q-TOF ion mobility-mass spectrometer; and (3) data analysis using Progenesis QI and EZ Info software. The data included in **Figure A.4** comes from a paper by members of our research group, investigating the lipidomic changes in a neuroblastoma cell line exposed to an environmental chemical, benzalkonium chlorides (BACs), and related compounds known to disrupt cholesterol and lipid homeostasis (K. Hines et al., 2017). Readers are encouraged to consult the original paper for the biological context.

A.2 Materials

A.2.1 General

Ammonium hydroxide (certified ACS reagent), ammonium acetate (Optima LC/MS grade), and sodium chloride (certified ACS crystalline) were purchased from Fisher Scientific. All mobile phase solvents (acetonitrile and water) and extraction reagents (chloroform, methanol, and methylene chloride) were Fisher Optima LC/MS grade. Lipid standards were purchased from Avanti Polar Lipids (Alabaster, AL) and Nu-Chek Prep (Elysian, MN). Phosphate buffer saline (PBS) was purchased from Gibco.

A.2.2 Sample Preparation

1. 1x phosphate buffer saline.
2. *DC*™ Protein Assay Kit II.

A.2.3 Folch Lipid Extraction

1. Folch solution: 2:1 (v/v) chloroform/methanol.

2. Sodium chloride solution: 0.9% (w/v) NaCl aqueous solution.

A.2.4 HILIC-MS

1. HILIC A mobile phase: 95% ACN, 5% H_2O, 5 mM ammonium acetate.
2. HILIC B mobile phase: 50% ACN, 50% H_2O, 5 mM ammonium acetate.

A.2.5 Lipid Standards

1. Lipid internal standard solution: prepare 1 mM stock solutions of lipid standards in chloroform. Prepare a 5 µM mixture in HILIC A (*see* **Table A.1** for the list of lipid standards).
2. Lipid mixture solution: extracts purchased from Avanti Polar Lipids were prepared at 1 mM concentration in chloroform. Prepare a 10 µM mixture in chloroform. For analysis, make a 1:2 dilution of the mixture in HILIC A (*see* **Table A.2** for the list of lipid extracts).
3. CCS calibrants: phosphatidylcholine (PC) and phosphatidylethanolamine (PE) lipid standards (Avanti Polar Lipids). Prepare 1 mM stock solutions of lipid standards. Prepare a mixture of PC 6:0-24:0 in methanol with 0.1% formic acid for positive mode analysis and PE 6:0-24:0 at 5-10 µM in methanol with 50 µM ammonium hydroxide for negative mode analysis. Prior to calibration, make a 1:4 dilution of the PC mixture and a 1:2 dilution of the PE mixture in their respective solvents (*see* **Table A.3**).

A.2.6 Supplies and Equipment

1. Analytical Column: HILIC Phenomenex Kinetex®, 2.1 x 100 mm, 1.7 µm.
2. Guard Cartridge: Phenomenex SecurityGuard® ULTRA HILIC Cartridge for 2.1mm ID UHPLC columns.

3. Guard Cartridge Holder: Phenomenex SecurityGuard® ULTRA Holder for 2.1-4.6 mm ID UHPLC columns.
4. Instrument: Waters Synapt® G2-Si HDMS equipped with an ESI source (Waters Corporation, Milford, MA, USA).
5. Inlet System: Waters® Acquity I-Class FTN UPLC with Autosampler (Waters Corporation, Milford, MA, USA).

A.3 Methods

Carry out procedures at room temperature.

A.3.1 Sample Preparation – Cultured Cells

1. Pellet a minimum of 10^6 cells in a Pyrex glass centrifuge tube at 104 x g (750 rpm) for 5 minutes at 4°C (Sorvall® Legend® X1R Centrifuge) and keep samples on ice (*see* **Notes 1**).
2. Lyse in 300 µL chilled 1x PBS using cold sonication for 30 minutes.
3. Conduct protein quantitation assay in a 96-well microplate (BioTek® Synergy® HTX Microplate Reader) (*see* **Notes 2**).
4. Store at -80°C or perform lipid extraction immediately.

A.3.2 Sample Preparation - Tissues

1. Measure tissue weight (*see* **Notes 2**).
2. Add 4 mL Folch solution.
3. Disrupt and homogenize tissue for 30 seconds using a tissue homogenizer (Polytron® PT 1200 Kinematica).
4. Add 1 mL NaCl solution.
5. Continue to step 2 of "Folch Lipid Extraction."

A.3.3 Folch Lipid Extraction

1. Add 4 mL Folch solution and 1 mL NaCl solution to cell lysates.
2. If including lipid internal standard, add to sample (*see* **Notes 3**).
3. Vortex for 30 seconds.
4. Centrifuge at 1660 x g (3000 rpm) for 5 minutes at 4°C.
5. Using a 9" glass Pasteur pipet with a mechanical pipet pump, pipette through the upper, aqueous phase and protein layer and transfer approximately 2 mL of the lower organic layer to a 10 mL glass tube.
6. Dry lipid extracts with a speed vacuum concentrator (Thermo Fisher Savant SpeedVac® SC210A).
7. Reconstitute in 300 µL CH_2Cl_2 for cells and tissue samples with weights below 100 mg. Reconstitute heavier tissue samples in 1 mL CH_2Cl_2 and transfer to HPLC vials with screw caps. Store at -80°C until HILIC-MS analysis.

A.3.4 Data Acquisition

1. To prepare samples for analysis, make a 1:4 dilution of lipid extracts in an LC glass autosampler vial. Adjust dilutions according to instrument signal intensity (*see* **Notes 4**).
2. Prepare a pooled QC sample, combining an equal volume from each final sample into a separate LC autosampler vial.
3. Equilibrate LC column and instrument (*see* **Table A.4**, **Table A.5**, and **Table A.6**). The pressure should be around 4000 psi when the 0.5 mL/min flow rate is established.
4. Perform detector setup through the Intellistart interface (*see* **Notes 5**).

5. Mass calibration. Infuse sodium formate at 20 μL/min and perform mass calibration through the Intellistart interface for both positive and negative modes.
6. Switch the instrument to Mobility TOF mode and allow the IM cell to equilibrate for an hour.
7. CCS calibration. Direct infuse PC and PE calibrant mixtures at 15 μL/min and calibrate through the Intellistart interface (*see* **Figure A.3**).
8. LockSpray Source Setup to check calibration curve quality (checks that it gives the right CCS for LeuEnk based on the observed DT).
9. Inject the lipid extract mix (*see* **Figure A.1** and **Figure A.2** for example chromatograms), standard mix, and a blank sample.
10. Randomize the sample list and increment a QC sample every 10 injections.

A.3.5 Data Processing and Analysis (*see* **Figure A.4**)

1. Import .raw files into Progenesis® QI (Nonlinear Dynamics) and process data in the chromatographic region between 0.4 and 8.5 minutes: data alignment to a reference QC sample, automatic peak detection of profile (continuum) data, and normalization to the external standard.
2. Perform multivariate statistical analysis of the data (EZInfo).
3. If internal standard was used, normalize externally to signal intensity of the appropriate internal standard.
4. Determine features that are significantly different between groups.
5. Identify features by matching retention time to the lipid classes, *m/z* to the METLIN, LIPID MAPS, and LipidBlast databases, and CCS values to LipidIMMS and our own lipid CCS database.

A.4 Notes

1. Glass tubes and pipettes are recommended when working with chloroform to prevent leaching of plasticizers, typically eluting between 2-3 minutes, which will interfere with data analysis.
2. Data should be normalized to protein concentrations or tissue weight and internal standard (if used) post-data acquisition.
3. An example internal standard is d17:1/12:0 sphingo PE, N-lauroyl-D-erythro-sphingosyl phosphoethanolamine, catalog no. 860529. Please refer to the original paper (Cifkova et al., 2012) for more information on quantitative analysis using a single internal lipid standard.
4. Signal intensity of TIC should be on the order of 10^7 to ensure detection of lower concentration lipids. Preparing samples at two concentrations may be necessary to get the best results for both high and low abundance lipids.
5. LockSpray should be utilized (leucine-enkephalin; positive mode: *m/z* 566.2771, CCS 226.0; negative mode: *m/z* 564.2615, CCS 224.0) to correct shifts in masses and drift times throughout the run.

Figures

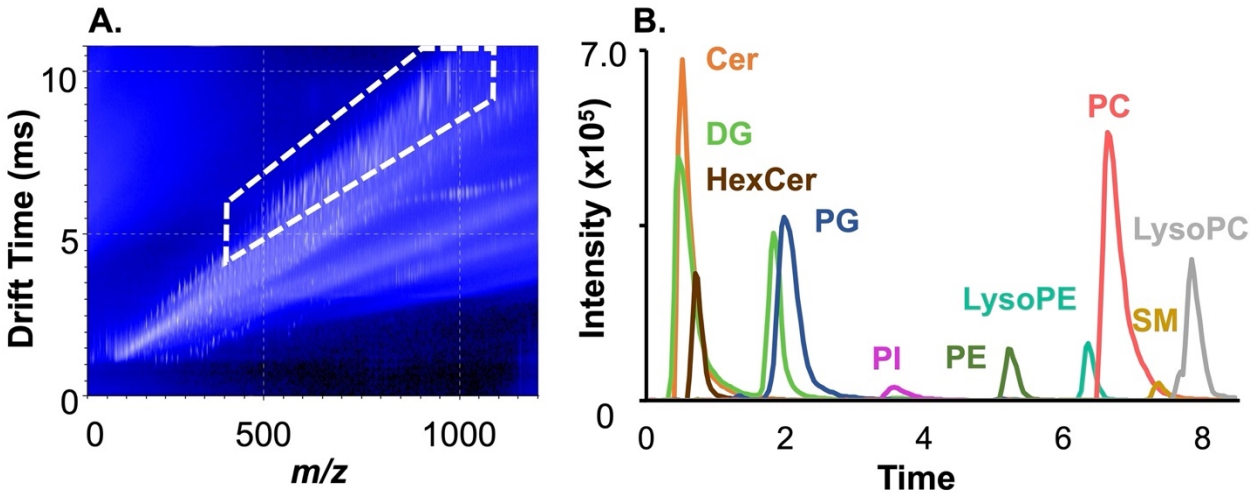

Figure A.1 A. Drift time versus *m/z* spectrum showing IM profile of lipids. **B.** Chromatogram of the most intense lipids from individual lipid subclasses present in the mammalian lipid extract mixture. Ceramide d36:1; Diacylglycerol 36:4; Hexosylceramide d42:2; Phosphatidylglycerol 34:1; Phosphatidylinositol 38:4; Phosphatidylethanolamine 36:1; LysoPE 18:0; Phosphatidylcholine 34:1; Sphingomyelin d36:1; LysoPC 16:0.

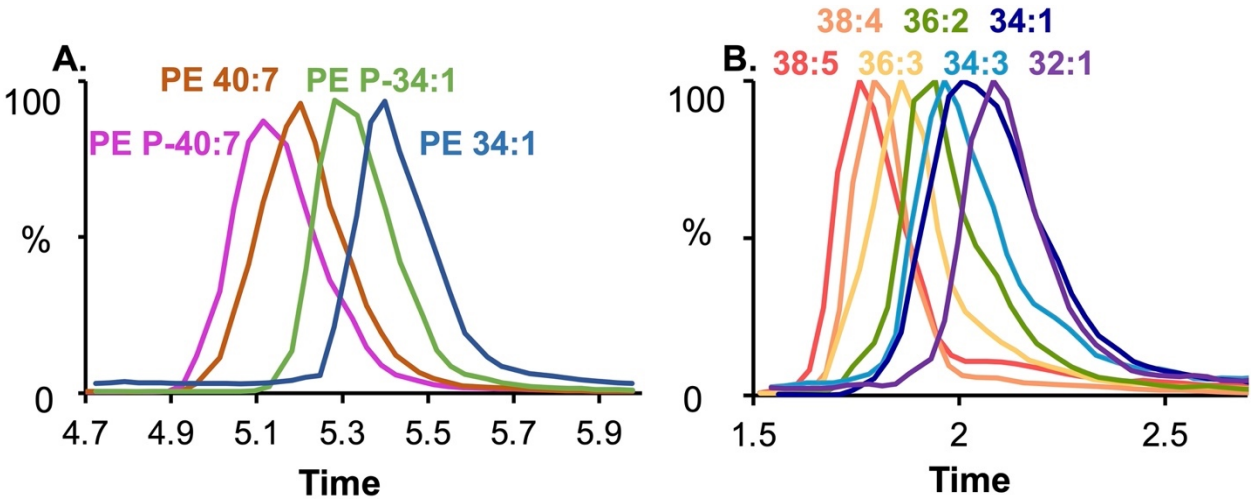

Figure A.2 A. Chromatogram showing separation of phosphatidyl and plasmenyl PEs. M+H adducts shown. **B.** Chromatogram showing separation of PGs by fatty acyl chain composition. From left to right: PG 38:5; PG 38:4; PG 36:3; PG 36:2; PG 34:3; PG 34:1; PG 32:1. M+Na adducts shown.

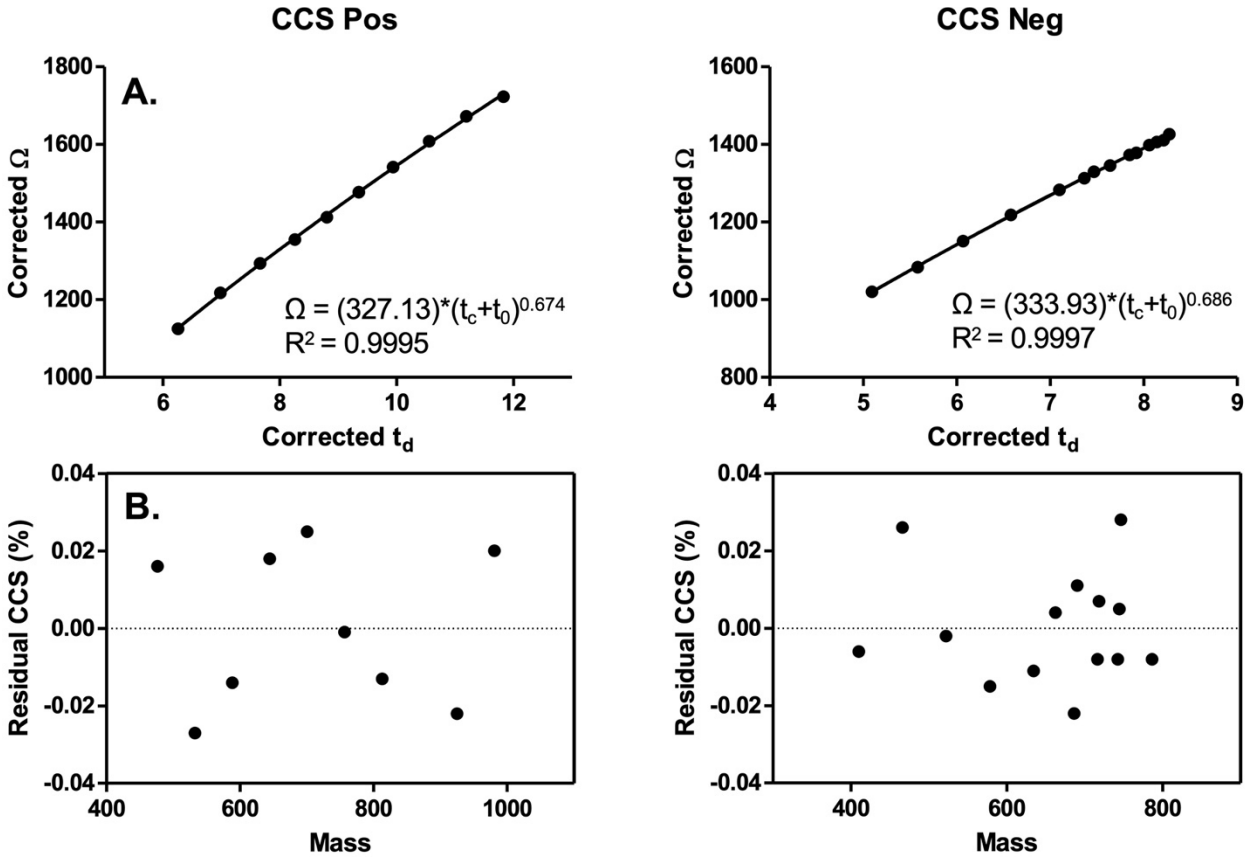

Figure A.3 A. Example calibration plots and **B.** corresponding residual plots for CCS calibration in both positive and negative ionization modes using PC and PE calibrant mixtures, respectively.

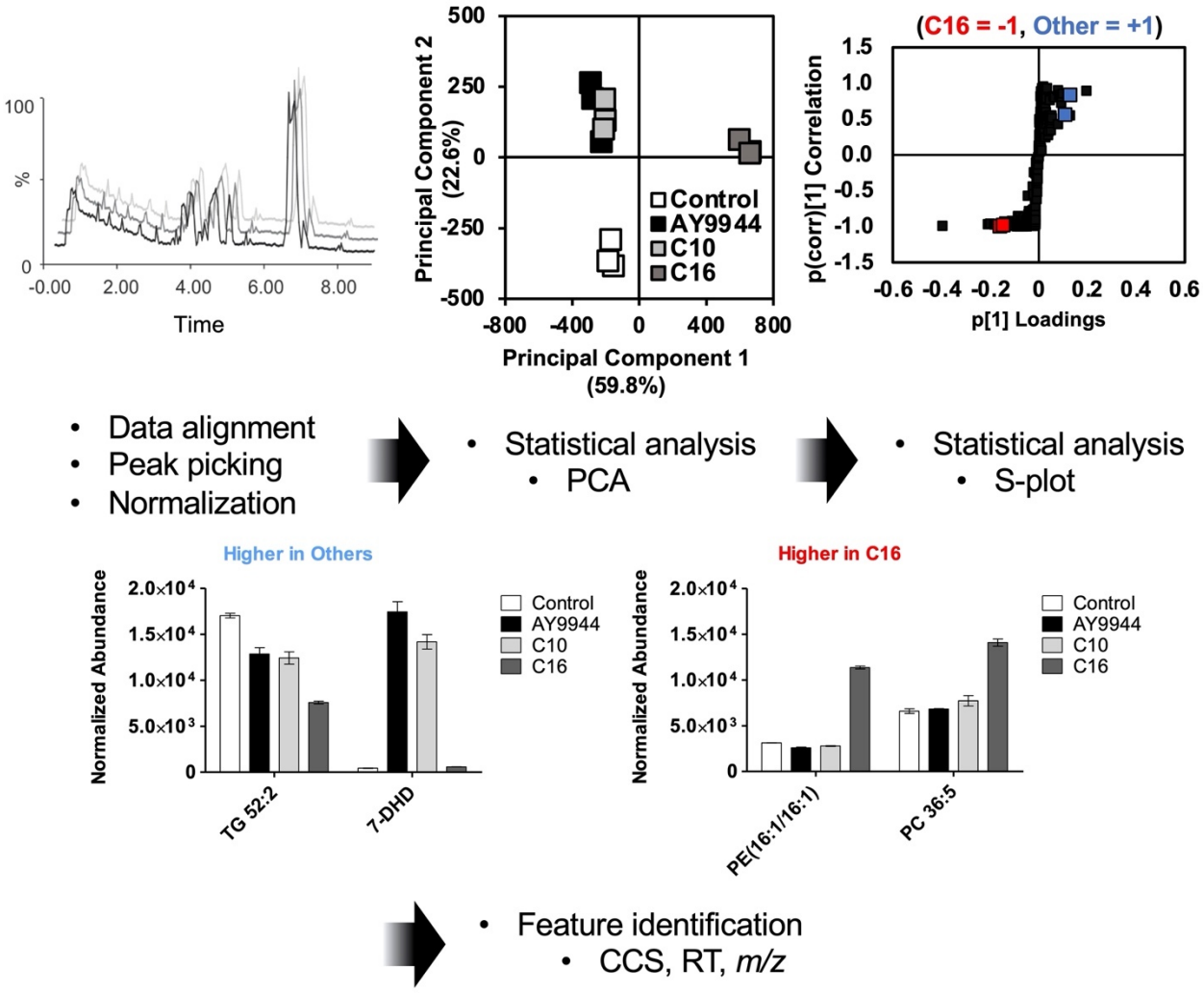

Figure A.4 Schematic of HILIC-IM-MS data analysis workflow from MS data processing to lipid identification.

Tables

Table A.1 Lipid standards included in discrete lipid internal standards mixture

Lipid common name	Systematic name	Catalog no.
DG 13:0/13:0	Ditridecanoin glyceride	D-136 (Nu-Chek)
TG 15:0/15:0/15:0	Tripentadecanoin glyceride	T-145 (Nu-Chek)
Cer d18:1/17:0	N-heptadecanoyl-D-erythro-sphingosine	860517
PG 15:0/15:0	1,2-dipentadecanoyl-sn-glycero-3-phospho-(1'-rac-glycerol)	840446
PE 15:0/15:0	1,2-dipentadecanoyl-sn-glycero-3-phosphoethanolamine	850704
PC 15:0/15:0	1,2-dipentadecanoyl-sn-glycero-3-phosphocholine	850350
PA 12:0/12:0	1,2-dilauroyl-sn-glycero-3-phosphate	840635
PS 12:0/12:0	1,2-dilauroyl-sn-glycero-3-phospho-L-serine	840038
SM d18:1/17:0	N-heptadecanoyl-D-erythro-sphingosylphosphorylcholine	860585
C12 Sphingosyl PE	N-lauroyl-D-erythro-sphingosyl phosphoethanolamine	860529
Lyso PC 15:0/0:0	1-pentadecanoyl-2-hydroxy-sn-glycero-3-phosphocholine	855576
Lyso PE 13:0/0:0	1-tridecanoyl-sn-glycero-3-phosphoethanolamine	856706

Table A.2 Lipid extracts included in the lipid mixture

Lipid class	**Catalog no.**
Ceramide	860052P
Cerebroside	131303P
Sphingomyelin	860062C
L-α-phosphatidic acid	840101C
L-α-phosphatidylcholine	840051C
L-α-lysophosphatidylcholine	830071P
L-α-phosphatidylethanolamine	840022C
L-α-phosphatidylglycerol	841138C
L-α-phosphatidylinositol	840042C
L-α-phosphatidylserine	840032C
Diacylglyceride	Nu-Chek Prep

Table A.3 PE and PC lipid species included in the lipid CCS calibration mixture

Lipid common name	Systematic name	Catalog no.	Conc. (μM)
PE 6:0/6:0	1,2-dihexanoyl-sn-glycero-3-phosphoethanolamine	850697C	5
PE 8:0/8:0	1,2-dioctanoyl-sn-glycero-3-phosphoethanolamine	850699C	5
PE 10:0/10:0	1,2-didecanoyl-sn-glycero-3-phosphoethanolamine	850700C	5
PE 12:0/12:0	1,2-dilauroyl-sn-glycero-3-phosphoethanolamine	850702X	5
PE 14:0/14:0	1,2-dimyristoyl-sn-glycero-3-phosphoethanolamine	850745X	5
PE 15:0/15:0	1,2-dipentadecanoyl-sn-glycero-3-phosphoethanolamine	850704X	10
PE 16:1/16:1	1,2-dipalmitoleoyl-sn-glycero-3-phosphoethanolamine	850706C	10
PE 16:0/16:0	1,2-dipalmitoyl-sn-glycero-3-phosphoethanolamine	850705X	10
PE 16:0/18:1	1-palmitoyl-2-oleoyl-sn-glycero-3-phosphoethanolamine	850757C	10
PE 17:0/17:0	1,2-diheptadecanoyl-sn-glycero-3-phosphoethanolamine	830756X	10
PE 18:1/18:1	1,2-dioleoyl-sn-glycero-3-phosphoethanolamine	850725C	10
PE 18:0/18:1	1-stearoyl-2-oleoyl-sn-glycero-3-phosphoethanolamine	850758C	10
PE 18:0/18:0	1,2-distearoyl-sn-glycero-3-phosphoethanolamine	850715X	10
PE 20:4/20:4	1,2-diarachidonoyl-sn-glycero-3-phosphoethanolamine	850800C	10

Lipid common name	Systematic name	Catalog no.	Conc. (μM)
PC 6:0/6:0	1,2-dihexanoyl-sn-glycero-3-phosphocholine	850305C	5
PC 8:0/8:0	1,2-dioctanoyl-sn-glycero-3-phosphocholine	850315C	5
PC 10:0/10:0	1,2-didecanoyl-sn-glycero-3-phosphocholine	850325C	5
PC 12:0/12:0	1,2-dilauroyl-sn-glycero-3-	850335C	5

	phosphocholine		
PC 14:0/14:0	1,2-dimyristoyl-sn-glycero-3-phosphocholine	850345C	5
PC 16:0/16:0	1,2-dipalmitoyl-sn-glycero-3-phosphocholine	850355C	10
PC 18:0/18:0	1,2-distearoyl-sn-glycero-3-phosphocholine	850365C	10
PC 20:0/20:0	1,2-diarachidoyl-sn-glycero-3-phosphocholine	850368C	10
PC 22:0/22:0	1,2-dibehenoyl-sn-glycero-3-phosphocholine	850371C	10
PC 24:0/24:0	1,2-dilignoceroyl-sn-glycero-3-phosphocholine	850373C	10

Table A.4 HILIC-IM-MS parameters: LC conditions

LC Method	
Injection volume	5 µL for positive mode, 10 µL for negative mode
Flow rate	0.5 mL/min
Column temperature	40°C
Sample temperature	6°C
Mobile phase gradient	0-1 min: Hold at 100% HILIC A 4 min: Hold at 90% HILIC A 7-8 min: Linear gradient to 70% HILIC A 9-12 min: Equilibrate at 100% HILIC A

Table A.5 MS source conditions

Source Conditions	
Mode	Resolution
Mass range	50-1200 *m/z*
Capillary voltage	+2.5 kV for positive, -2.0 kV for negative
Sampling cone	40 V
Source offset	80 V
Source temperature	150°C
Desolvation temperature	500°C
Desolvation gas flow	1000 L/hr
Cone gas flow	100 L/hr
Nebulizer gas flow	5.0 bar

Table A.6 Ion mobility parameters

IM/MS Conditions	
IMS wave velocity	500 m/s
IMS wave height	40.0 V
Trap wave velocity	311 m/z
Trap wave height	4.0 V
Trap collision Energy	4.0 eV
Transfer wave velocity	380 m/s
Transfer wave height	4.0 V
Transfer collision energy, function 1 (MS)	2.0 eV
Transfer collision energy, function 2 (MS^E)	Low, 35 eV High, 45 eV
Trap Gas Flow	2 mL/min
Helium Cell Gas Flow	180 mL/min
IMS Gas Flow	90 mL/min

Appendix B. Curriculum Vitae

AMY LI

Department of Medicinal Chemistry
1705 NE Pacific Street, Box 357610
Seattle, WA 98195-7610
ali94@uw.edu

EDUCATION

University of Washington | Seattle, WA | Degree awarded **December 2023**
Ph.D. in Medicinal Chemistry
Dissertation: "Temporal and Spatial Multi-Omics Characterization of Smith-Lemli-Opitz Syndrome"
Advisor: Dr. Libin Xu

Pepperdine University | Malibu, CA | Degree awarded **April 2016**
Bachelor of Science in Biochemistry with Honors, *summa cum laude*
Thesis: "An improved method for tetrodotoxin determination by high performance liquid chromatography coupled with fluorescence detection applied to TTX levels in the California newt"

GRANTS AND AWARDS

Achievement Rewards for College Scientists (ARCS) Fellow 2016-2019
Seattle Chapter ARCS Foundation

Pharmacological Sciences Training Program (PSTP) Fellow 2018-2020
National Institute of Health (T32 GM007750)

ITHS TL1 Translational Research Training Program Fellow 2020-2021
National Center for Advancing Translational Sciences (TL1 TR002318)

Magnuson Scholarship 2020-2021

Scott Grimm Memorial Scholarship 2020, 2022

Graduate Student Leadership Award 2021

WORK AND RESEARCH EXPERIENCE

University of Washington

Graduate Research Assistant | Medicinal Chemistry — Summer 2017-Winter 2023

Teaching Assistant, Organic Medicinal Agents — Fall 2017

Teaching Assistant, Immunizing and Antimicrobial Agents — Spring 2018

Pepperdine University

Undergraduate Research Student | Analytical Chemistry — Spring 2013-Spring 2015

Undergraduate Research Student | Atmospheric Chemistry — Fall 2015-Spring 2016

Laboratory Teaching Assistant, General Chemistry I and II — Fall 2013-Spring 2016

Private Tutor, General Chemistry I and II — Summer 2013-Spring 2016

Oregon Health and Science University

Summer Internship Research Student | Cell, Developmental, and Cancer Biology — Summer 2015

LEADERSHIP & ACTIVITIES

UW School of Pharmacy Leadership Committee Fall 2021-Spring 2022

- Served as a graduate student representative of my departmental program for an academic year
- Attended quarterly meetings with School of Pharmacy faculty, staff, and student representatives
- Communicated student activities and concerns to the committee, and provided feedback and input for faculty regarding issues related to graduate students

Departmental Graduate Students Mentorship Program Fall 2020-Spring 2022

- Established a graduate student mentorship program for incoming 1st year students
- Mentored two students over the course of two academic years to help with their transition to graduate school

PUBLICATIONS

1. **Li, A.**; Tomita, H.; Xu, L. (2023) Temporal gene expression changes and affected pathways in neurodevelopment of a mouse model of Smith-Lemli-Opitz syndrome, *bioRxiv* (preprint), doi: https://doi.org/10.1101/2023.11.21.568116
2. **Li, A.**; Xu, L. (2023) MALDI-IM-MS Imaging of Brain Sterols and Lipids in a Mouse Model of Smith-Lemli-Opitz Syndrome, *bioRxiv* (preprint), doi: https://doi.org/10.1101/2023.10.02.560415
3. Elias, E. R.; Orth, L. E.; **Li, A.**; Xu, L.; Jones, S. M.; Rizzo, W. B. (2023) Cholic Acid Increases Plasma Cholesterol in Smith-Lemli-Opitz Syndrome: A Pilot Study, *Molecular Genetics and Metabolism Reports*, 38, 101030
4. Zhang, R.; Ashford, N. K.; **Li, A**.; Ross, D. H.; Werth, B. J.; Xu, L. (2023) High-throughput analysis of lipidomic phenotypes of methicillin-resistant Staphylococcus aureus by coupling in situ 96-well cultivation and HILIC-ion mobility-mass spectrometry. *Analytical and Bioanalytical Chemistry,* 415, 6191-6199
5. Tomita, H.; Hines, K.M.; Herron, J.M.; **Li, A.**; Baggett, D.W.; Xu, L. (2022) 7-Dehydrocholesterol-derived oxysterols cause neurogenic defects in Smith-Lemli-Opitz syndrome. *eLife*, 11, e67141
6. Lo, M.; Sharir, A.; Paul, M.; Torosyan, H.; Agnew, C.; **Li, A**.; Neben, C.; Marangoni, P.; Xu, L.; Raleigh, D.; Jura, N.; Klein, O. (2022) CNPY4 inhibits the Hedgehog pathway by modulating membrane sterol lipids. *Nature Communication*, 13, 2407
7. **Li, A.**; Hines, K. M.; Ross, D. H.; MacDonald, J. W.; Xu, L. (2022) Temporal changes in the brain lipidome during neurodevelopment of Smith-Lemli-Opitz syndrome mice. *Analyst,* 147, 1611
8. Daggubati, V.; Hochstetler, J.; Bommireddy, A.; Choudhury, A.; Krup, A.L.; Choksi, P.K.; Tong, P.; **Li, A.**; Xu, L.; Reiter, J.F.; Raleigh, D. R. (2021) Smoothened-activating lipids drive resistance to CDK4/6 inhibition in Hedgehog-associated medulloblastoma cells and preclinical models. *J. Clin. Invest.*, 131, e141171
9. Findakly, S.; Daggubati, V.; Garcia, G.; LaStella, S. A.; Choudhury, A.; Tran, C.; **Li, A.**; Tong, P.; Garcia, J. Q.; Puri, N.; Reiter, J. F.; Xu, L.; Raleigh, D. R., (2021) Sterol and oxysterol synthases near the ciliary base activate the Hedgehog pathway. *J. Cell. Biol.*, 220, e202002026
10. Golla, R. M.; Mishra, B.; Dang, X.; Narayana, J. L.; **Li, A.**; Xu, L.; Wang, G. (2020) Resistome of Staphylococcus aureus in Response to Human Cathelicidin LL-37 and its Engineered Antimicrobial Peptides. *ACS Infectious Diseases,* 6(7), 1866-1881

11. **Li, Amy**; Hines, Kelly M.; Xu, Libin. (2020) Lipidomics by HILIC-Ion Mobility-Mass Spectrometry. *Methods in Molecular Biology,* vol. 2084: 119-132
12. Sytsma, Trevor M.; **Li, Amy**; Ganske, J. A. (2018) Nitric Acid Acts Upon Copper: Gas Phase Product Analysis of a Historic Reaction Using Fourier Transform Infrared Spectroscopy. *The Chemical Educator,* 23, 58-63
13. Bucciarelli, Gary M.; **Li, Amy**; Zimmer, Richard K.; Kats, Lee B.; Green, David B. (2014) Quantifying tetrodotoxin levels in the California newt using a non-destructive sampling method. *Toxicon,* 80, 87-93

PRESENTATIONS

Conference Poster Sessions

1. Li, Amy and Xu, Libin. *Spatial Brain Lipidomics of Adult Age WT and SLOS (T93M) Mice by MALDI-IM-MS Imaging.* 70th ASMS Conference on Mass Spectrometry and Allied Topics, Minneapolis, MN (June 2022)
2. Li, Amy and Xu, Libin. *Spatial Changes in Brain Lipids of WT and SLOS Mice by MALDI-IM-MS Imaging.* 69th ASMS Conference on Mass Spectrometry and Allied Topics, Philadelphia, PA (Nov 2021)
3. Li, Amy; Hines, Kelly M.; Xu, Libin. *Alterations in mouse brain lipidome during neurodevelopment and in a model of Smith-Lemli-Opitz syndrome.* 68th ASMS Conference on Mass Spectrometry and Allied Topics, Virtual (June 2020)
4. Li, Amy; Xu, Libin. *Desorption Electrospray Ionization Mass Spectrometry Imaging of Brain Tissue from a Mouse Model of Smith-Lemli-Opitz Syndrome.* 67th ASMS Conference on Mass Spectrometry and Allied Topics, Atlanta, GA (June 2019)
5. Li, Amy; Arnett, Anne; Pepper, Micah; Bernier, Raphael; Xu, Libin. *Lipidomics analysis of cultured human fibroblasts form individuals with autism spectrum disorders.* 66th ASMS Conference on Mass Spectrometry and Allied Topics, San Diego, CA (June 2018)
6. Li, Amy; Arnett, Anne; Pepper, Micah; Bernier, Raphael; Xu, Libin. *Lipidomics analysis of cultured human fibroblasts form individuals with autism spectrum disorders.* 14th Annual conference of the Metabolomics Society, Seattle, WA (June 2018)
7. Li, Amy; Gribble, Matthew D.; Ganske, Jane A. *Exploiting the action of copper on nitric acid to generate atmospherically relevant nitrogen-containing gases: A physical-atmospheric chemistry laboratory project.* 251st ACS National Meeting & Exposition, San Diego, CA (March 2016)
8. Li, Amy; Jablonski, Lia M.; Green, David B. *Solid-phase extraction using new divalent metal ion-loaded cation exchange resins and application to the isolation of oleandrin from Nerium oleander*. 249th ACS National Meeting & Exposition, Denver, CO (March 2015)
9. McCollum, Alexandria M.; Longo, Angela M.; Goosherst, Kevin J.; Jablonski, Lia M.; Kaak, Marissa L.; Li, Amy; Sacenti, Dylan G.; Green, David B.; Fristch, Joseph M. *Non-Newtonian fluids as a student affiliates chapter event: Chemistry, logistics, outreach.* 249th ACS National Meeting and Exposition, Denver, CO (March 2015)
10. Li, Amy; Bucciarelli, Gary; Kats, Lee B.; Green, David B. *Reduced sample size and improved extraction and recovery of tetrodotoxin from the California newt, T. torosa with quantitation by HPLC-FLD.* 247th ACS National Meeting & Exposition, Dallas, TX (March 2014)

Oral Presentations

1. *Investigating the pathogenesis, diagnosis, and treatment of Smith-Lemli-Opitz syndrome.* Pre-general Examination (November 2018) and General Examination (November 2019)

2. *Disorders of Cholesterol Biosynthesis: their genetic mutations, pathogenic mechanisms, and pharmaceutical inhibitors of involved enzymes*. Literature Seminar (January 2018)

GRADUATE COURSEWORK

Signaling Mechanisms in Excitable Cells
Signal Transduction from the Cell Membrane to the Nucleus
Advanced Physical Organic Chemistry
Advanced Medicinal Chemistry
Drug Metabolism
Laboratory Methods in Protein Therapeutics
Biological Mass Spectrometry
Advanced Bio-Organic Chemistry
Introduction to Structural Biology
Biophysical Enzymology and Biopharmaceuticals
Introduction to Neurobiology
Introduction to Epidemiology
Applied Biostatistics I & II

REFERENCES

Libin Xu, Ph.D.
Associate Professor
Department of Medicinal Chemistry
University of Washington School of Pharmacy
libinxu@uw.edu

REFERENCES

Acevedo, A., Durán, C., Ciucci, S., Gerl, M., & Cannistraci, C. V. (2018). LIPEA: Lipid Pathway Enrichment Analysis. *BioRxiv*, 274969. doi:10.1101/274969

Ashburner, M., Ball, C. A., Blake, J. A., Botstein, D., Butler, H., Cherry, J. M., . . . Sherlock, G. (2000). Gene ontology: tool for the unification of biology. The Gene Ontology Consortium. *Nat Genet, 25*(1), 25-29. doi:10.1038/75556

Aslam, M., & Ladilov, Y. (2022). Emerging Role of cAMP/AMPK Signaling. *Cells, 11*(2). doi:10.3390/cells11020308

Baker, P. R., Armando, A. M., Campbell, J. L., Quehenberger, O., & Dennis, E. A. (2014). Three-dimensional enhanced lipidomics analysis combining UPLC, differential ion mobility spectrometry, and mass spectrometric separation strategies. *J Lipid Res*, Epub ahead of print. doi: 10.1194/jlr.D051581. doi:10.1194/jlr.D051581

Battaile, K. P., Battaile, B. C., Merkens, L. S., Maslen, C. L., & Steiner, R. D. (2001). Carrier frequency of the common mutation IVS8-1G>C in DHCR7 and estimate of the expected incidence of Smith-Lemli-Opitz syndrome. *Mol Genet Metab, 72*(1), 67-71. doi:10.1006/mgme.2000.3103

Ben-Ari, Y. (2014). The GABA excitatory/inhibitory developmental sequence: a personal journey. *Neuroscience, 279*, 187-219. doi:10.1016/j.neuroscience.2014.08.001

Benjamini, Y., & Hochberg, Y. (1995). Controlling the False Discovery Rate: A Practical and Powerful Approach to Multiple Testing. *Journal of the Royal Statistical Society: Series B (Methodological), 57*(1), 289-300. doi:https://doi.org/10.1111/j.2517-6161.1995.tb02031.x

Bjorkhem, I., Cedazo-Minguez, A., Leoni, V., & Meaney, S. (2009). Oxysterols and neurodegenerative diseases. *Mol Aspects Med, 30*(3), 171-179. doi:S0098-2997(09)00008-9 [pii] 10.1016/j.mam.2009.02.001

Boland, M. R., & Tatonetti, N. P. (2016). Investigation of 7-dehydrocholesterol reductase pathway to elucidate off-target prenatal effects of pharmaceuticals: a systematic review. *Pharmacogenomics J, 16*(5), 411-429. doi:10.1038/tpj.2016.48

Brantley, S. E., & Di Talia, S. (2021). Cell cycle control during early embryogenesis. *Development, 148*(13). doi:10.1242/dev.193128

Brown, A. J., & Jessup, W. (1999). Oxysterols and atherosclerosis. *Atherosclerosis, 142*(1), 1-28. doi:10.1016/s0021-9150(98)00196-8

Bukelis, I., Porter, F. D., Zimmerman, A. W., & Tierney, E. (2007). Smith-Lemli-Opitz syndrome and autism spectrum disorder. *Am J Psychiatry, 164*(11), 1655-1661. doi:10.1176/appi.ajp.2007.07020315

Burla, B., Arita, M., Arita, M., Bendt, A. K., Cazenave-Gassiot, A., Dennis, E. A., . . . Wenk, M. R. (2018). MS-based lipidomics of human blood plasma: a community-initiated position paper to develop accepted guidelines. *J Lipid Res, 59*(10), 2001-2017. doi:10.1194/jlr.S087163

Bush, M. F., Campuzano, I. D., & Robinson, C. V. (2012). Ion mobility mass spectrometry of peptide ions: effects of drift gas and calibration strategies. *Anal Chem, 84*(16), 7124-7130. doi:10.1021/ac3014498

Castillo, P. E., Younts, T. J., Chavez, A. E., & Hashimotodani, Y. (2012). Endocannabinoid signaling and synaptic function. *Neuron, 76*(1), 70-81. doi:10.1016/j.neuron.2012.09.020

Caughlin, S., Park, D. H., Yeung, K. K.-C., Cechetto, D. F., & Whitehead, S. N. (2017). Sublimation of DAN Matrix for the Detection and Visualization of Gangliosides in Rat Brain Tissue for MALDI Imaging Mass Spectrometry. *J Vis Exp*(121). doi:10.3791/55254

Chan, Y. M., Merkens, L. S., Connor, W. E., Roullet, J. B., Penfield, J. A., Jordan, J. M., . . . Jones, P. J. (2009). Effects of dietary cholesterol and simvastatin on cholesterol synthesis in Smith-Lemli-Opitz syndrome. *Pediatr Res, 65*(6), 681-685. doi:10.1203/PDR.0b013e31819ea4eb

Chen, V. S., Morrison, J. P., Southwell, M. F., Foley, J. F., Bolon, B., & Elmore, S. A. (2017). Histology Atlas of the Developing Prenatal and Postnatal Mouse Central Nervous System, with Emphasis on Prenatal Days E7.5 to E18.5. *Toxicol Pathol, 45*(6), 705-744. doi:10.1177/0192623317728134

Ciara, E., Popowska, E., Piekutowska-Abramczuk, D., Jurkiewicz, D., Borucka-Mankiewicz, M., Kowalski, P., . . . Krajewska-Walasek, M. (2006). SLOS carrier frequency in Poland as determined by screening for Trp151X and Val326Leu DHCR7 mutations. *Eur J Med Genet, 49*(6), 499-504. doi:10.1016/j.ejmg.2006.01.006

Cifkova, E., Holcapek, M., Lisa, M., Ovcacikova, M., Lycka, A., Lynen, F., & Sandra, P. (2012). Nontargeted quantitation of lipid classes using hydrophilic interaction liquid chromatography-electrospray ionization mass spectrometry with single internal standard and response factor approach. *Anal Chem, 84*(22), 10064-10070. doi:10.1021/ac3024476

Cooper, M. K., Wassif, C. A., Krakowiak, P. A., Taipale, J., Gong, R., Kelley, R. I., . . . Beachy, P. A. (2003). A defective response to Hedgehog signaling in disorders of cholesterol biosynthesis. *Nat Genet, 33*(4), 508-513. doi:10.1038/ng1134

Correa-Cerro, L. S., Wassif, C. A., Kratz, L., Miller, G. F., Munasinghe, J. P., Grinberg, A., . . . Porter, F. D. (2006). Development and characterization of a hypomorphic Smith-Lemli-Opitz syndrome mouse model and efficacy of simvastatin therapy. *Hum Mol Genet, 15*(6), 839-851. doi:10.1093/hmg/ddl003

Dang Do, A. N., Baker, E. H., Warren, K. E., Bianconi, S. E., & Porter, F. D. (2018). Spontaneously regressing brain lesions in Smith-Lemli-Opitz syndrome. *Am J Med Genet A, 176*(2), 386-390. doi:10.1002/ajmg.a.38563

Dehay, C., & Kennedy, H. (2007). Cell-cycle control and cortical development. *Nat Rev Neurosci, 8*(6), 438-450. doi:10.1038/nrn2097

Dennis, G., Sherman, B. T., Hosack, D. A., Yang, J., Gao, W., Lane, H. C., & Lempicki, R. A. (2003). DAVID: Database for Annotation, Visualization, and Integrated Discovery. *Genome Biology, 4*(5). doi:10.1186/gb-2003-4-5-p3

Dietschy, J. M., & Turley, S. D. (2004). Cholesterol metabolism in the central nervous system during early development and in the mature animal. *J Lipid Res, 45*(8), 1375-1397. doi:10.1194/jlr.R400004-JLR200

Donato, M., Xu, Z., Tomoiaga, A., Granneman, J. G., Mackenzie, R. G., Bao, R., . . . Draghici, S. (2013). Analysis and correction of crosstalk effects in pathway analysis. *Genome Res, 23*(11), 1885-1893. doi:10.1101/gr.153551.112

Draghici, S., Khatri, P., Tarca, A. L., Amin, K., Done, A., Voichita, C., . . . Romero, R. (2007). A systems biology approach for pathway level analysis. *Genome Res, 17*(10), 1537-1545. doi:10.1101/gr.6202607

Edison, R., & Muenke, M. (2003). The interplay of genetic and environmental factors in craniofacial morphogenesis: holoprosencephaly and the role of cholesterol. *Congenit Anom (Kyoto), 43*(1), 1-21. doi:10.1111/j.1741-4520.2003.tb01022.x

Elias, E. R., Irons, M. B., Hurley, A. D., Tint, G. S., & Salen, G. (1997). Clinical effects of cholesterol supplementation in six patients with the Smith-Lemli-Opitz syndrome (SLOS). *American Journal of Medical Genetics, 68*(3), 305-310. doi:10.1002/(sici)1096-8628(19970131)68:3<305::aid-ajmg11>3.0.co;2-x

Fahy, E., Subramaniam, S., Brown, H. A., Glass, C. K., Merrill, A. H., Jr., Murphy, R. C., . . . Dennis, E. A. (2005). A comprehensive classification system for lipids. *J Lipid Res, 46*(5), 839-861. doi:10.1194/jlr.E400004-JLR200

Fahy, E., Subramaniam, S., Murphy, R. C., Nishijima, M., Raetz, C. R., Shimizu, T., . . . Dennis, E. A. (2009). Update of the LIPID MAPS comprehensive classification system for lipids. *J Lipid Res, 50 Suppl*, S9-14. doi:10.1194/jlr.R800095-JLR200

Fenn, L. S., Kliman, M., Mahsut, A., Zhao, S. R., & McLean, J. A. (2009). Characterizing ion mobility-mass spectrometry conformation space for the analysis of complex biological samples. *Anal Bioanal Chem, 394*(1), 235-244. doi:10.1007/s00216-009-2666-3

Fenn, L. S., & McLean, J. A. (2008). Biomolecular structural separations by ion mobility-mass spectrometry. *Anal Bioanal Chem, 391*(3), 905-909. doi:10.1007/s00216-008-1951-x

Finlay, B. L., & Darlington, R. B. (1995). Linked regularities in the development and evolution of mammalian brains. *Science, 268*(5217), 1578-1584. doi:10.1126/science.7777856

Fitzky, B. U., Moebius, F. F., Asaoka, H., Waage-Baudet, H., Xu, L., Xu, G., . . . Tint, G. S. (2001). 7-Dehydrocholesterol–dependent proteolysis of HMG-CoA reductase suppresses sterol biosynthesis in a mouse model of Smith-Lemli-Opitz/RSH syndrome. *Journal of Clinical Investigation, 108*(6), 905-915. doi:10.1172/jci200112103

Fitzky, B. U., Witsch-Baumgartner, M., Erdel, M., Lee, J. N., Paik, Y. K., Glossmann, H., . . . Moebius, F. F. (1998). Mutations in the Delta7-sterol reductase gene in patients with the Smith-Lemli-Opitz syndrome. *Proc Natl Acad Sci U S A, 95*(14), 8181-8186. doi:10.1073/pnas.95.14.8181

Fliesler, S. J. (2013). Antioxidants: The Missing Key to Improved Therapeutic Intervention in Smith-Lemli-Opitz Syndrome? *Hereditary Genet, 2*(2), 119. doi:10.4172/2161-1041.1000119

Fliesler, S. J., Peachey, N. S., Herron, J., Hines, K. M., Weinstock, N. I., Ramachandra Rao, S., & Xu, L. (2018). Prevention of Retinal Degeneration in a Rat Model of Smith-Lemli-Opitz Syndrome. *Sci Rep, 8*(1), 1286. doi:10.1038/s41598-018-19592-8

Foran, D. R., & Peterson, A. C. (1992). Myelin acquisition in the central nervous system of the mouse revealed by an MBP-Lac Z transgene. *J Neurosci, 12*(12), 4890-4897. doi:10.1523/JNEUROSCI.12-12-04890.1992

Forsythe, J. G., Petrov, A. S., Walker, C. A., Allen, S. J., Pellissier, J. S., Bush, M. F., . . . Fernandez, F. M. (2015). Collision cross section calibrants for negative ion mode traveling wave ion mobility-mass spectrometry. *Analyst, 140*(20), 6853-6861. doi:10.1039/c5an00946d

Francis, K. R., Ton, A. N., Xin, Y., O'Halloran, P. E., Wassif, C. A., Malik, N., . . . Porter, F. D. (2016). Modeling Smith-Lemli-Opitz syndrome with induced pluripotent stem cells reveals a causal role for Wnt/beta-catenin defects in neuronal cholesterol synthesis phenotypes. *Nat Med, 22*(4), 388-396. doi:10.1038/nm.4067

Funfschilling, U., Jockusch, W. J., Sivakumar, N., Mobius, W., Corthals, K., Li, S., . . . Saher, G. (2012). Critical Time Window of Neuronal Cholesterol Synthesis during Neurite Outgrowth. *J Neurosci, 32*(22), 7632-7645. doi:10.1523/JNEUROSCI.1352-11.2012

Gene Ontology, C., Aleksander, S. A., Balhoff, J., Carbon, S., Cherry, J. M., Drabkin, H. J., . . . Westerfield, M. (2023). The Gene Ontology knowledgebase in 2023. *Genetics, 224*(1). doi:10.1093/genetics/iyad031

Griffiths, W. J., & Wang, Y. (2018). An update on oxysterol biochemistry: New discoveries in lipidomics. *Biochem Biophys Res Commun, 504*(3), 617-622. doi:10.1016/j.bbrc.2018.02.019

Haas, D., Niklowitz, P., Hoffmann, G. F., Andler, W., & Menke, T. (2008). Plasma and thrombocyte levels of coenzyme Q10 in children with Smith-Lemli-Opitz syndrome (SLOS) and the influence of HMG-CoA reductase inhibitors. *Biofactors, 32*(1-4), 191-197. doi:10.1002/biof.5520320123

Han, X., & Gross, R. W. (2005). Shotgun lipidomics: electrospray ionization mass spectrometric analysis and quantitation of cellular lipidomes directly from crude extracts of biological samples. *Mass Spectrom Rev, 24*(3), 367-412. doi:10.1002/mas.20023

Han, X., & Gross, R. W. (2022). The foundations and development of lipidomics. *J Lipid Res, 63*(2), 100164. doi:10.1016/j.jlr.2021.100164

Herman, G. E. (2003). Disorders of cholesterol biosynthesis: prototypic metabolic malformation syndromes. *Hum Mol Genet, 12 Spec No 1*, R75-88. doi:10.1093/hmg/ddg072

Hines, K., Herron, J., & Xu, L. (2017). Assessment of Altered Lipid Homeostasis by HILIC-Ion Mobility-Mass Spectrometry-Based Lipidomics. *J Lipid Res, 58*(4), 809-819. doi:10.1194/jlr.D074724

Hines, K. M., May, J. C., McLean, J. A., & Xu, L. (2016). Evaluation of Collision Cross Section Calibrants for Structural Analysis of Lipids by Traveling Wave Ion Mobility-Mass Spectrometry. *Anal Chem, 88*(14), 7329-7336. doi:10.1021/acs.analchem.6b01728

Hines, K. M., Waalkes, A., Penewit, K., Holmes, E. A., Salipante, S. J., Werth, B. J., & Xu, L. (2017). Characterization of the Mechanisms of Daptomycin Resistance among Gram-Positive Bacterial Pathogens by Multidimensional Lipidomics. *mSphere, 2*(6), e00492-00417. doi:10.1128/mSphere.00492-17

Hines, K. M., & Xu, L. (2019). Lipidomic consequences of phospholipid synthesis defects in Escherichia coli revealed by HILIC-ion mobility-mass spectrometry. *Chem Phys Lipids, 219*, 15-22. doi:10.1016/j.chemphyslip.2019.01.007

Hinz, C., Liggi, S., & Griffin, J. L. (2018). The potential of Ion Mobility Mass Spectrometry for high-throughput and high-resolution lipidomics. *Curr Opin Chem Biol, 42*, 42-50. doi:10.1016/j.cbpa.2017.10.018

Horton, J. D., Goldstein, J. L., & Brown, M. S. (2002). SREBPs: activators of the complete program of cholesterol and fatty acid synthesis in the liver. *J Clin Invest, 109*(9), 1125-1131. doi:10.1172/JCI15593

Ikonen, E. (2008). Cellular cholesterol trafficking and compartmentalization. *Nat Rev Mol Cell Biol, 9*(2), 125-138. doi:10.1038/nrm2336

Irons, M., Elias, E. R., Abuelo, D., Bull, M. J., Greene, C. L., Johnson, V. P., . . . Salen, G. (1997). Treatment of Smith-Lemli-Opitz syndrome: results of a multicenter trial. *Am J Med Genet, 68*(3), 311-314.

Irons, M., Elias, E. R., Salen, G., Tint, G. S., & Batta, A. K. (1993). Defective cholesterol biosynthesis in Smith-Lemli-Opitz syndrome. *Lancet, 341*(8857), 1414. doi:10.1016/0140-6736(93)90983-n

Ivanova, P. T., Milne, S. B., Byrne, M. O., Xiang, Y., & Brown, H. A. (2007). Glycerophospholipid identification and quantitation by electrospray ionization mass spectrometry. *Methods Enzymol, 432*, 21-57. doi:10.1016/S0076-6879(07)32002-8

Jiang, X. S., Wassif, C. A., Backlund, P. S., Song, L., Holtzclaw, L. A., Li, Z., . . . Porter, F. D. (2010). Activation of Rho GTPases in Smith-Lemli-Opitz syndrome: pathophysiological and clinical implications. *Hum Mol Genet, 19*(7), 1347-1357. doi:10.1093/hmg/ddq011

Jira, P. E., Waterham, H. R., Wanders, R. J., Smeitink, J. A., Sengers, R. C., & Wevers, R. A. (2003). Smith-Lemli-Opitz syndrome and the DHCR7 gene. *Ann Hum Genet, 67*(Pt 3), 269-280. doi:10.1046/j.1469-1809.2003.00034.x.

Jira, P. E., Wevers, R. A., de Jong, J., Rubio-Gozalbo, E., Janssen-Zijlstra, F. S. M., van Heyst, A. F. J., . . . Smeitink, J. A. M. (2000). Simvastatin: a new therapeutic approach for Smith-Lemli-Opitz syndrome. *Journal of Lipid Research, 41*(8), 1339-1346. doi:10.1016/S0022-2275(20)33442-8

Joensuu, M., Wallis, T. P., Saber, S. H., & Meunier, F. A. (2020). Phospholipases in neuronal function: A role in learning and memory? *J Neurochem, 153*(3), 300-333. doi:10.1111/jnc.14918

Jurowski, K., Kochan, K., Walczak, J., Baranska, M., Piekoszewski, W., & Buszewski, B. (2017). Analytical Techniques in Lipidomics: State of the Art. *Crit Rev Anal Chem, 47*(5), 418-437. doi:10.1080/10408347.2017.1310613

Kanehisa, M., & Goto, S. (2000). KEGG: kyoto encyclopedia of genes and genomes. *Nucleic Acids Res, 28*(1), 27-30. doi:10.1093/nar/28.1.27

Kanuri, B., Fong, V., Ponny, S. R., Tallman, K. A., Rao, S. R., Porter, N., . . . Patel, S. B. (2021). Generation and validation of a conditional knockout mouse model for the study of the Smith-Lemli-Opitz syndrome. *J Lipid Res, 62*, 100002. doi:10.1194/jlr.RA120001101

Keller, R. K., Arnold, T. P., & Fliesler, S. J. (2004). Formation of 7-dehydrocholesterol-containing membrane rafts in vitro and in vivo, with relevance to the Smith-Lemli-Opitz syndrome. *Journal of Lipid Research, 45*(2), 347-355.

Kelley, R. I., & Hennekam, R. C. (2000). The Smith-Lemli-Opitz syndrome. *J Med Genet, 37*(5), 321-335. doi:10.1136/jmg.37.5.321

Kim, D., Paggi, J. M., Park, C., Bennett, C., & Salzberg, S. L. (2019). Graph-based genome alignment and genotyping with HISAT2 and HISAT-genotype. *Nat Biotechnol, 37*(8), 907-915. doi:10.1038/s41587-019-0201-4

Kliman, M., May, J. C., & McLean, J. A. (2011). Lipid analysis and lipidomics by structurally selective ion mobility-mass spectrometry. *Biochim. Biophys. Acta, Mol. Cell Biol. Lipids, 1811*(11), 935-945. doi:10.1016/j.bbalip.2011.05.016

Kluver, H., & Barrera, E. (1953). A method for the combined staining of cells and fibers in the nervous system. *J Neuropathol Exp Neurol, 12*(4), 400-403. doi:10.1097/00005072-195312040-00008

Korade, Z., Xu, L., Mirnics, K., & Porter, N. A. (2013). Lipid biomarkers of oxidative stress in a genetic mouse model of Smith-Lemli-Opitz syndrome. *J Inherit Metab Dis, 36*(1), 113-122. doi:10.1007/s10545-012-9504-z

Korade, Z., Xu, L., Shelton, R., & Porter, N. A. (2010). Biological activities of 7-dehydrocholesterol-derived oxysterols: implications for Smith-Lemli-Opitz syndrome. *J. Lipid Res., 51*(11), 3259-3269. doi:10.1194/jlr.M009365

Koudinov, A. R., & Koudinova, N. V. (2001). Essential role for cholesterol in synaptic plasticity and neuronal degeneration. *FASEB J, 15*(10), 1858-1860. doi:10.1096/fj.00-0815fje

Kukurba, K. R., & Montgomery, S. B. (2015). RNA Sequencing and Analysis. *Cold Spring Harb Protoc, 2015*(11), 951-969. doi:10.1101/pdb.top084970

Kyle, J. E., Zhang, X., Weitz, K. K., Monroe, M. E., Ibrahim, Y. M., Moore, R. J., . . . Baker, E. S. (2016). Uncovering biologically significant lipid isomers with liquid chromatography, ion mobility spectrometry and mass spectrometry. *Analyst, 141*(5), 1649-1659. doi:10.1039/c5an02062j

Lazarin, G. A., Haque, I. S., Evans, E. A., & Goldberg, J. D. (2017). Smith-Lemli-Opitz syndrome carrier frequency and estimates of in utero mortality rates. *Prenat Diagn, 37*(4), 350-355. doi:10.1002/pd.5018

Le Belle, J. E., Orozco, N. M., Paucar, A. A., Saxe, J. P., Mottahedeh, J., Pyle, A. D., . . . Kornblum, H. I. (2011). Proliferative neural stem cells have high endogenous ROS levels that regulate self-renewal and neurogenesis in a PI3K/Akt-dependant manner. *Cell Stem Cell, 8*(1), 59-71. doi:10.1016/j.stem.2010.11.028

Leaptrot, K. L., May, J. C., Dodds, J. N., & McLean, J. A. (2019). Ion mobility conformational lipid atlas for high confidence lipidomics. *Nat Commun, 10*(1), 985. doi:10.1038/s41467-019-08897-5

Lee, R. W., Conley, S. K., Gropman, A., Porter, F. D., & Baker, E. H. (2013). Brain magnetic resonance imaging findings in Smith-Lemli-Opitz syndrome. *Am J Med Genet A, 161A*(10), 2407-2419. doi:10.1002/ajmg.a.36096

Lee, R. W., Yoshida, S., Jung, E. S., Mori, S., Baker, E. H., & Porter, F. D. (2013). Corpus Callosum Measurements Correlate with Developmental Delay in Smith-Lemli-Opitz Syndrome. *Pediatr Neurol, 49*(2), 107-112. doi:10.1016/j.pediatrneurol.2013.03.015

Li, A., Hines, K. M., Ross, D. H., MacDonald, J. W., & Xu, L. (2022). Temporal changes in the brain lipidome during neurodevelopment of Smith-Lemli-Opitz syndrome mice. *Analyst, 147*(8), 1611-1621. doi:10.1039/d2an00137c

Li, A., Hines, K. M., & Xu, L. (2020). Lipidomics by HILIC-Ion Mobility-Mass Spectrometry. *Methods Mol Biol, 2084*, 119-132. doi:10.1007/978-1-0716-0030-6_7

Li, H., Handsaker, B., Wysoker, A., Fennell, T., Ruan, J., Homer, N., . . . Genome Project Data Processing, S. (2009). The Sequence Alignment/Map format and SAMtools. *Bioinformatics, 25*(16), 2078-2079. doi:10.1093/bioinformatics/btp352

Li, T., & Chiang, J. Y. (2009). Regulation of bile acid and cholesterol metabolism by PPARs. *PPAR Res, 2009*, 501739. doi:10.1155/2009/501739

Liao, Y., Smyth, G. K., & Shi, W. (2014). featureCounts: an efficient general purpose program for assigning sequence reads to genomic features. *Bioinformatics, 30*(7), 923-930. doi:10.1093/bioinformatics/btt656

Liebisch, G., Vizcaino, J. A., Kofeler, H., Trotzmuller, M., Griffiths, W. J., Schmitz, G., . . . Wakelam, M. J. (2013). Shorthand notation for lipid structures derived from mass spectrometry. *J Lipid Res, 54*(6), 1523-1530. doi:10.1194/jlr.M033506

Love, M. I., Huber, W., & Anders, S. (2014). Moderated estimation of fold change and dispersion for RNA-seq data with DESeq2. *Genome Biol, 15*(12), 550. doi:10.1186/s13059-014-0550-8

Lu, Z., Huang, L., Li, Y., Xu, Y., Zhang, R., Zhou, Q., . . . Zhao, B. (2022). Fine-Tuning of Cholesterol Homeostasis Controls Erythroid Differentiation. *Adv Sci (Weinh), 9*(2), e2102669. doi:10.1002/advs.202102669

Marion, R. W., Alvarez, L. A., Marans, Z. S., Lantos, G., & Chitayat, D. (1987). Computed tomography of the brain in the Smith-Lemli-Opitz syndrome. *J Child Neurol, 2*(3), 198-200. doi:10.1177/088307388700200305

Mason, E. A., & McDaniel, E. W. (1988). *Transport properties of ions in gases*. New York: Wiley.

Mason, E. A., & Schamp Jr, H. W. (1958). Mobility of gaseous lons in weak electric fields. *Annals of Physics, 4*(3), 233-270. doi:10.1016/0003-4916(58)90049-6

Mauch, D. H., Nagler, K., Schumacher, S., Goritz, C., Muller, E. C., Otto, A., & Pfrieger, F. W. (2001). CNS synaptogenesis promoted by glia-derived cholesterol. *Science, 294*(5545), 1354-1357. doi:10.1126/science.294.5545.1354

May, J. C., Goodwin, C. R., Lareau, N. M., Leaptrot, K. L., Morris, C. B., Kurulugama, R. T., . . . McLean, J. A. (2014). Conformational ordering of biomolecules in the gas phase: nitrogen collision cross sections measured on a prototype high resolution drift tube ion mobility-mass spectrometer. *Anal Chem, 86*(4), 2107-2116. doi:10.1021/ac4038448

McLean, J. A., Ruotolo, B. T., Gillig, K. J., & Russell, D. H. (2005). Ion mobility-mass spectrometry: a new paradigm for proteomics. *International Journal of Mass Spectrometry, 240*(3), 301-315. doi:10.1016/j.ijms.2004.10.003

Merrill, A. H., Jr., Sullards, M. C., Allegood, J. C., Kelly, S., & Wang, E. (2005). Sphingolipidomics: high-throughput, structure-specific, and quantitative analysis of sphingolipids by liquid chromatography tandem mass spectrometry. *Methods, 36*(2), 207-224. doi:10.1016/j.ymeth.2005.01.009

Metsalu, T., & Vilo, J. (2015). ClustVis: a web tool for visualizing clustering of multivariate data using Principal Component Analysis and heatmap. *Nucleic Acids Res, 43*(W1), W566-570. doi:10.1093/nar/gkv468

Moebius, F. F., Fitzky, B. U., Lee, J. N., Paik, Y.-K., & Glossmann, H. (1998). Molecular cloning and expression of the human !7-sterol reductase. *Proc Natl Acad Sci U S A, 95*, 1899-1902.

Molyneaux, B. J., Arlotta, P., Menezes, J. R., & Macklis, J. D. (2007). Neuronal subtype specification in the cerebral cortex. *Nat Rev Neurosci, 8*(6), 427-437. doi:10.1038/nrn2151

Nishina, A., Kimura, H., Sekiguchi, A., Fukumoto, R.-h., Nakajima, S., & Furukawa, S. (2006). Lysophosphatidylethanolamine in Grifola frondosa as a neurotrophic activator via activation of MAPK. *Journal of Lipid Research, 47*(7), 1434-1443. doi:https://doi.org/10.1194/jlr.M600045-JLR200

Nowaczyk, M. J., Nakamura, L. M., Eng, B., Porter, F. D., & Waye, J. S. (2001). Frequency and ethnic distribution of the common DHCR7 mutation in Smith-Lemli-Opitz syndrome. *Am J Med Genet, 102*(4), 383-386. doi:10.1002/ajmg.1441

Nwokoro, N. A., & Mulvihill, J. J. (1997). Cholesterol and bile acid replacement therapy in children and adults with Smith-Lemli-Opitz (SLO/RSH) syndrome. *American Journal of Medical Genetics, 68*(3), 315-321. doi:10.1002/(sici)1096-8628(19970131)68:3<315::aid-ajmg13>3.0.co;2-w

O'Brien, J. S., & Sampson, E. L. (1965). Lipid composition of the normal human brain: gray matter, white matter, and myelin. *J Lipid Res, 6*(4), 537-544.

Olkku, A., & Mahonen, A. (2009). Calreticulin mediated glucocorticoid receptor export is involved in beta-catenin translocation and Wnt signalling inhibition in human osteoblastic cells. *Bone, 44*(4), 555-565. doi:10.1016/j.bone.2008.11.013

Olsen, A. S. B., & Faergeman, N. J. (2017). Sphingolipids: membrane microdomains in brain development, function and neurological diseases. *Open Biol, 7*(5). doi:10.1098/rsob.170069

Paglia, G., Angel, P., Williams, J. P., Richardson, K., Olivos, H. J., Thompson, J. W., . . . Astarita, G. (2015). Ion mobility-derived collision cross section as an additional measure for lipid fingerprinting and identification. *Anal Chem, 87*(2), 1137-1144. doi:10.1021/ac503715v

Pang, Z., Chong, J., Zhou, G., de Lima Morais, D. A., Chang, L., Barrette, M., . . . Xia, J. (2021). MetaboAnalyst 5.0: narrowing the gap between raw spectra and functional insights. *Nucleic Acids Research, 49*(W1), W388-W396. doi:10.1093/nar/gkab382

Peerboom, C., & Wierenga, C. J. (2021). The postnatal GABA shift: A developmental perspective. *Neurosci Biobehav Rev, 124*, 179-192. doi:10.1016/j.neubiorev.2021.01.024

Phipson, B., Lee, S., Majewski, I. J., Alexander, W. S., & Smyth, G. K. (2016). Robust Hyperparameter Estimation Protects against Hypervariable Genes and Improves Power to Detect Differential Expression. *Ann Appl Stat, 10*(2), 946-963. doi:10.1214/16-AOAS920

Picache, J. A., Rose, B. S., Balinski, A., Leaptrot, K. L., Sherrod, S. D., May, J. C., & McLean, J. A. (2019). Collision cross section compendium to annotate and predict multi-omic compound identities. *Chem Sci, 10*(4), 983-993. doi:10.1039/c8sc04396e

Porter, F. D. (2002). Malformation syndromes due to inborn errors of cholesterol synthesis. *Journal of Clinical Investigation, 110*(6), 715-724. doi:10.1172/JCI200216386

Porter, F. D., & Herman, G. E. (2011). Malformation syndromes caused by disorders of cholesterol synthesis. *J Lipid Res, 52*(1), 6-34. doi:10.1194/jlr.R009548

Porter, J. A., Young, K. E., & Beachy, P. A. (1996). Cholesterol modification of hedgehog signaling proteins in animal development. *Science, 274*(5285), 255-259. doi:10.1126/science.274.5285.255

Poursharifi, P., Madiraju, S. R. M., & Prentki, M. (2017). Monoacylglycerol signalling and ABHD6 in health and disease. *Diabetes Obes Metab, 19 Suppl 1*, 76-89. doi:10.1111/dom.13008

Quehenberger, O., & Dennis, E. A. (2011). The human plasma lipidome. *N Engl J Med, 365*(19), 1812-1823. doi:10.1056/NEJMra1104901

Quehenberger, O., et al. (2010). Lipidomics reveals a remarkable diversity of lipids in human plasma. *J Lipid Res, 51*(11), 3299-3305. doi:jlr.M009449 [pii] 10.1194/jlr.M009449

Raleigh, D. R., Sever, N., Choksi, P. K., Sigg, M. A., Hines, K. M., Thompson, B. M., . . . Reiter, J. F. (2018). Cilia-Associated Oxysterols Activate Smoothened. *Mol Cell, 72*(2), 316-327 e315. doi:10.1016/j.molcel.2018.08.034

Repa, J. J., Liang, G., Ou, J., Bashmakov, Y., Lobaccaro, J. M., Shimomura, I., . . . Mangelsdorf, D. J. (2000). Regulation of mouse sterol regulatory element-binding protein-1c gene (SREBP-1c) by oxysterol receptors, LXRalpha and LXRbeta. *Genes Dev, 14*(22), 2819-2830.

Ritchie, M. E., Phipson, B., Wu, D., Hu, Y., Law, C. W., Shi, W., & Smyth, G. K. (2015). limma powers differential expression analyses for RNA-sequencing and microarray studies. *Nucleic Acids Res, 43*(7), e47. doi:10.1093/nar/gkv007

Ross, D. H., Cho, J. H., & Xu, L. (2020). Breaking Down Structural Diversity for Comprehensive Prediction of Ion-Neutral Collision Cross Sections. *Anal Chem, 92*(6), 4548-4557. doi:10.1021/acs.analchem.9b05772

Ross, D. H., Cho, J. H., Zhang, R., Hines, K. M., & Xu, L. (2020). LiPydomics: A Python Package for Comprehensive Prediction of Li- pid Collision Cross Sections and Retention Times and Analysis of Ion Mobility-Mass Spectrometry-Based Lipidomics Data. *Anal Chem, 92*, 14967–14975.

Ross, D. H., Seguin, R. P., & Xu, L. (2019). Characterization of the Impact of Drug Metabolism on the Gas-Phase Structures of Drugs Using Ion Mobility-Mass Spectrometry. *Anal Chem, 91*(22), 14498-14507. doi:10.1021/acs.analchem.9b03292.

Roux, C., Wolf, C., Mulliez, N., Gaoua, W., Cormier, V., Chevy, F., & Citadelle, D. (2000). Role of cholesterol in embryonic development. *Am J Clin Nutr, 71*(5 Suppl), 1270S-1279S. doi:10.1093/ajcn/71.5.1270s

Ruotolo, B. T., Benesch, J. L., Sandercock, A. M., Hyung, S. J., & Robinson, C. V. (2008). Ion mobility-mass spectrometry analysis of large protein complexes. *Nat Protoc, 3*(7), 1139-1152. doi:10.1038/nprot.2008.78

Rustam, Y. H., & Reid, G. E. (2018). Analytical Challenges and Recent Advances in Mass Spectrometry Based Lipidomics. *Anal Chem, 90*(1), 374-397. doi:10.1021/acs.analchem.7b04836

Ryan, E., & Reid, G. E. (2016). Chemical Derivatization and Ultrahigh Resolution and Accurate Mass Spectrometry Strategies for "Shotgun" Lipidome Analysis. *Acc Chem Res, 49*(9), 1596-1604. doi:10.1021/acs.accounts.6b00030

Sacchetti, P., Sousa, K. M., Hall, A. C., Liste, I., Steffensen, K. R., Theofilopoulos, S., . . . Arenas, E. (2009). Liver X receptors and oxysterols promote ventral midbrain neurogenesis in vivo and in human embryonic stem cells. *Cell Stem Cell, 5*(4), 409-419. doi:10.1016/j.stem.2009.08.019

Saher, G., Brugger, B., Lappe-Siefke, C., Mobius, W., Tozawa, R., Wehr, M. C., . . . Nave, K. A. (2005). High cholesterol level is essential for myelin membrane growth. *Nat Neurosci, 8*(4), 468-475. doi:10.1038/nn1426

Schoner, K., Witsch-Baumgartner, M., Behunova, J., Petrovic, R., Bald, R., Kircher, S. G., . . . Rehder, H. (2020). Smith-Lemli-Opitz syndrome - Fetal phenotypes with special reference to the syndrome-specific internal malformation pattern. *Birth Defects Res, 112*(2), 175-185. doi:10.1002/bdr2.1620

Schwudke, D., Liebisch, G., Herzog, R., Schmitz, G., & Shevchenko, A. (2007). Shotgun lipidomics by tandem mass spectrometry under data-dependent acquisition control. *Methods Enzymol, 433*, 175-191. doi:10.1016/S0076-6879(07)33010-3

Sherman, B. T., Hao, M., Qiu, J., Jiao, X., Baseler, M. W., Lane, H. C., . . . Chang, W. (2022). DAVID: a web server for functional enrichment analysis and functional annotation of gene lists (2021 update). *Nucleic Acids Res, 50*(W1), W216-W221. doi:10.1093/nar/gkac194

Sikora, D. M., Pettit-Kekel, K., Penfield, J., Merkens, L. S., & Steiner, R. D. (2006). The near universal presence of autism spectrum disorders in children with Smith-Lemli-Opitz syndrome. *Am J Med Genet A, 140*(14), 1511-1518. doi:10.1002/ajmg.a.31294

Sikora, D. M., Ruggiero, M., Petit-Kekel, K., Merkens, L. S., Connor, W. E., & Steiner, R. D. (2004). Cholesterol supplementation does not improve developmental progress in Smith-Lemli-Opitz syndrome. *J Pediatr, 144*(6), 783-791. doi:10.1016/j.jpeds.2004.02.036

Sisecioglu, M., Budak, H., Geffers, L., Cankaya, M., Ciftci, M., Thaller, C., . . . Ozdemir, H. (2015). A compendium of expression patterns of cholesterol biosynthetic enzymes in the mouse embryo. *J Lipid Res, 56*(8), 1551-1559. doi:10.1194/jlr.M059634

Smith, D. W., Lemli, L., & Opitz, J. M. (1964). A newly recognized syndrome of multiple congenital anomalies. *J Pediatr, 64*(2), 210-217.

Solomonov, Y., Hadad, N., & Levy, R. (2016). Reduction of cytosolic phospholipase A2α upregulation delays the onset of symptoms in SOD1G93A mouse model of amyotrophic lateral sclerosis. *Journal of Neuroinflammation, 13*(1), 134. doi:10.1186/s12974-016-0602-y

Tan, S. T., Ramesh, T., Toh, X. R., & Nguyen, L. N. (2020). Emerging roles of lysophospholipids in health and disease. *Prog Lipid Res, 80*, 101068. doi:10.1016/j.plipres.2020.101068

Teo, J. L., & Kahn, M. (2010). The Wnt signaling pathway in cellular proliferation and differentiation: A tale of two coactivators. *Adv Drug Deliv Rev, 62*(12), 1149-1155. doi:10.1016/j.addr.2010.09.012

Thurm, A., Tierney, E., Farmer, C., Albert, P., Joseph, L., Swedo, S., . . . Porter, F. D. (2016). Development, behavior, and biomarker characterization of Smith-Lemli-Opitz syndrome: an update. *J Neurodev Disord, 8*, 12. doi:10.1186/s11689-016-9145-x

Tierney, E., Conley, S. K., Goodwin, H., & Porter, F. D. (2010). Analysis of short-term behavioral effects of dietary cholesterol supplementation in Smith-Lemli-Opitz syndrome. *Am J Med Genet A, 152A*(1), 91-95. doi:10.1002/ajmg.a.33148

Tierney, E., Nwokoro, N. A., Porter, F. D., Freund, L. S., Ghuman, J. K., & Kelley, R. I. (2001). Behavior phenotype in the RSH/Smith-Lemli-Opitz syndrome. *Am J Med Genet, 98*(2), 191-200. doi:10.1002/1096-8628(20010115)98:2<191::aid-ajmg1030>3.0.co;2-m

Tint, G. S., Irons, M., Elias, E. R., Batta, A. K., Frieden, R., Chen, T. S., & Salen, G. (1994). Defective cholesterol biosynthesis associated with the Smith-Lemli-Opitz syndrome. *N Engl J Med, 330*(2), 107-113. doi:10.1056/NEJM199401133300205

Tint, G. S., Seller, M., Hughes-Benzie, R., Batta, A. K., Shefer, S., Genest, D., . . . Salen, G. (1995). Markedly increased tissue concentrations of 7-dehydrocholesterol combined with low levels of cholesterol are characteristic of the Smith-Lemli-Opitz syndrome. *J Lipid Res, 36*(1), 89-95.

Tint, G. S., Yu, H., Shang, Q., Xu, G., & Patel, S. B. (2006). The use of the Dhcr7 knockout mouse to accurately determine the origin of fetal sterols. *J Lipid Res, 47*(7), 1535-1541. doi:10.1194/jlr.M600141-JLR200

Tomita, H., Hines, K. M., Herron, J. M., Li, A., Baggett, D. W., & Xu, L. (2022). 7-Dehydrocholesterol-derived oxysterols cause neurogenic defects in Smith-Lemli-Opitz syndrome. *eLife, 11*. doi:10.7554/eLife.67141

Tsugawa, H., Ikeda, K., Takahashi, M., Satoh, A., Mori, Y., Uchino, H., . . . Arita, M. (2020). A lipidome atlas in MS-DIAL 4. *Nat Biotechnol, 38*, 1159–1163. doi:10.1038/s41587-020-0531-2

Tu, J., Yin, Y., Xu, M., Wang, R., & Zhu, Z. J. (2017). Absolute quantitative lipidomics reveals lipidome-wide alterations in aging brain. *Metabolomics, 14*(1), 5. doi:10.1007/s11306-017-1304-x

Ulmer, C. Z., Koelmel, J. P., Ragland, J. M., Garrett, T. J., & Bowden, J. A. (2017). LipidPioneer : A Comprehensive User-Generated Exact Mass Template for Lipidomics. *J Am Soc Mass Spectrom, 28*(3), 562-565. doi:10.1007/s13361-016-1579-6

Vandergrift, G. W., Lukowski, J. K., Taylor, M. J., Zemaitis, K. J., Alexandrov, T., Eder, J. G., . . . Anderton, C. (2023). Are Phosphatidic Acids Ubiquitous in Mammalian Tissues or Overemphasized in Mass Spectrometry Imaging Applications? *Analysis & Sensing*. doi:10.1002/anse.202200112

Waage-Baudet, H., Dunty, W. C., Jr., Dehart, D. B., Hiller, S., & Sulik, K. K. (2005). Immunohistochemical and microarray analyses of a mouse model for the smith-lemli-opitz syndrome. *Dev Neurosci, 27*(6), 378-396. doi:10.1159/000088453

Waage-Baudet, H., Lauder, J. M., Dehart, D. B., Kluckman, K., Hiller, S., Tint, G. S., & Sulik, K. K. (2003). Abnormal serotonergic development in a mouse model for the Smith-Lemli-Opitz syndrome: implications for autism. *Int J Dev Neurosci, 21*(8), 451-459. doi:10.1016/j.ijdevneu.2003.09.002

Walch, A., Rauser, S., Deininger, S. O., & Hofler, H. (2008). MALDI imaging mass spectrometry for direct tissue analysis: a new frontier for molecular histology. *Histochem Cell Biol, 130*(3), 421-434. doi:10.1007/s00418-008-0469-9

Wang, Z., Gerstein, M., & Snyder, M. (2009). RNA-Seq: a revolutionary tool for transcriptomics. *Nat Rev Genet, 10*(1), 57-63. doi:10.1038/nrg2484

Wassif, C. A., Kratz, L., Sparks, S. E., Wheeler, C., Bianconi, S., Gropman, A., . . . Porter, F. D. (2017). A placebo-controlled trial of simvastatin therapy in Smith-Lemli-Opitz syndrome. *Genet Med, 19*(3), 297-305. doi:10.1038/gim.2016.102

Wassif, C. A., Maslen, C., Kachilele-Linjewile, S., Lin, D., Linck, L. M., Connor, W. E., . . . Porter, F. D. (1998). Mutations in the human sterol delta7-reductase gene at 11q12-13 cause Smith-Lemli-Opitz syndrome. *Am J Hum Genet, 63*(1), 55-62. doi:10.1086/301936

Wassif, C. A., Zhu, P., Kratz, L., Krakowiak, P. A., Battaile, K. P., Weight, F. F., . . . Porter, F. D. (2001). Biochemical, phenotypic and neurophysiological characterization of a genetic mouse model of RSH/Smith--Lemli--Opitz syndrome. *Hum Mol Genet, 10*(6), 555-564. doi:10.1093/hmg/10.6.555

Waterham, H. R., & Hennekam, R. C. (2012). Mutational spectrum of Smith-Lemli-Opitz syndrome. *Am J Med Genet C Semin Med Genet, 160C*(4), 263-284. doi:10.1002/ajmg.c.31346

Waterham, H. R., Wijburg, F. A., Hennekam, R. C., Vreken, P., Poll-The, B. T., Dorland, L., . . . Wanders, R. J. (1998). Smith-Lemli-Opitz syndrome is caused by mutations in the 7-dehydrocholesterol reductase gene. *Am J Hum Genet, 63*(2), 329-338. doi:10.1086/301982

Wen, Z., Song, H., & Ming, G. L. (2016). Patient iPSCs: a new discovery tool for Smith-Lemli-Opitz syndrome. *Nat Med, 22*(4), 343-344. doi:10.1038/nm.4081

Wenk, M. R. (2010). Lipidomics: new tools and applications. *Cell, 143*(6), 888-895. doi:10.1016/j.cell.2010.11.033

Wishart, D. S., Knox, C., Guo, A. C., Eisner, R., Young, N., Gautam, B., . . . Forsythe, I. (2009). HMDB: a knowledgebase for the human metabolome. *Nucleic Acids Res, 37*(Database issue), D603-610. doi:10.1093/nar/gkn810

Witsch-Baumgartner, M., Fitzky, B. U., Ogorelkova, M., Kraft, H. G., Moebius, F. F., Glossmann, H., . . . Utermann, G. (2000). Mutational spectrum in the Delta7-sterol reductase gene and genotype-phenotype correlation in 84 patients with Smith-Lemli-Opitz syndrome. *Am J Hum Genet, 66*(2), 402-412. doi:10.1086/302760

Xu, L., Davis, T. A., & Porter, N. A. (2009). Rate Constants for Peroxidation of Polyunsaturated Fatty Acids and Sterols in Solution and in Liposomes. *J. Am. Chem. Soc., 131*(36), 13037-13044.

Xu, L., Korade, Z., & Porter, N. A. (2010). Oxysterols from free radical chain oxidation of 7-dehydrocholesterol: product and mechanistic studies. *J. Am. Chem. Soc., 132*(7), 2222-2232. doi:10.1021/ja9080265

Xu, L., Korade, Z., Rosado, D. A., Jr., Mirnics, K., & Porter, N. A. (2013). Metabolism of oxysterols derived from nonenzymatic oxidation of 7-dehydrocholesterol in cells. *J Lipid Res, 54*(4), 1135-1143. doi:10.1194/jlr.M035733

Xu, L., Korade, Z., Rosado, D. A., Liu, W., Lamberson, C. R., & Porter, N. A. (2011). An oxysterol biomarker for 7-dehydrocholesterol oxidation in cell/mouse models for Smith-Lemli-Opitz syndrome. *J. Lipid Res., 52*(6), 1222-1233. doi:10.1194/jlr.M014498

Xu, L., Liu, W., Sheflin, L. G., Fliesler, S. J., & Porter, N. A. (2011). Novel oxysterols observed in tissues and fluids of AY9944-treated rats - a model for Smith-Lemli-Opitz Syndrome. *J Lipid Res, 52*(10), 1810-1820. doi:10.1194/jlr.M018366

Xu, L., Mirnics, K., Bowman, A. B., Liu, W., Da, J., Porter, N. A., & Korade, Z. (2012). DHCEO accumulation is a critical mediator of pathophysiology in a Smith-Lemli-Opitz syndrome model. *Neurobiol Dis, 45*(3), 923-929. doi:10.1016/j.nbd.2011.12.011

Yu, H., Lee, M., Starck, L., Elias, E. R., Irons, M., Salen, G., . . . Tint, G. S. (2000). Spectrum of Δ7-dehydrocholesterol reductase mutations in patients with the Smith–Lemli–Opitz (RSH) syndrome. *Hum Mol Genet, 9*(9), 1385-1391.

Yu, H., & Patel, S. B. (2005). Recent insights into the Smith-Lemli-Opitz syndrome. *Clin Genet, 68*(5), 383-391. doi:10.1111/j.1399-0004.2005.00515.x

Zhou, H., Mehta, S., Srivastava, S. P., Grabinska, K., Zhang, X., Wong, C., . . . Goodwin, J. E. (2020). Endothelial cell-glucocorticoid receptor interactions and regulation of Wnt signaling. *JCI Insight, 5*(3). doi:10.1172/jci.insight.131384

Zhou, Z., Luo, M., Chen, X., Yin, Y., Xiong, X., Wang, R., & Zhu, Z. J. (2020). Ion mobility collision cross-section atlas for known and unknown metabolite annotation in untargeted metabolomics. *Nat Commun, 11*(1), 4334. doi:10.1038/s41467-020-18171-8

Zhou, Z., Shen, X., Chen, X., Tu, J., Xiong, X., & Zhu, Z. J. (2018). LipidIMMS Analyzer: Integrating multi-dimensional information to support lipid identification in ion mobility - mass spectrometry based lipidomics. *Bioinformatics*, In Press. doi: 10.1093/bioinformatics/bty1661. doi:10.1093/bioinformatics/bty661

Zhou, Z., Tu, J., Xiong, X., Shen, X., & Zhu, Z. J. (2017). LipidCCS: Prediction of Collision Cross-Section Values for Lipids with High Precision To Support Ion Mobility-Mass Spectrometry-Based Lipidomics. *Anal Chem, 89*(17), 9559-9566. doi:10.1021/acs.analchem.7b02625